การย่อยสลายโดยใช้แสงของเมธิลีนบลูด้วยตัวเร่งปฏิกิริยาแพลทินัมซิงค์ออกไซด์และทอง
ซิงค์ออกไซด์ที่สังเคราะห์โดยวิธีเฟลมสเปรย์ไพโรไลซิส
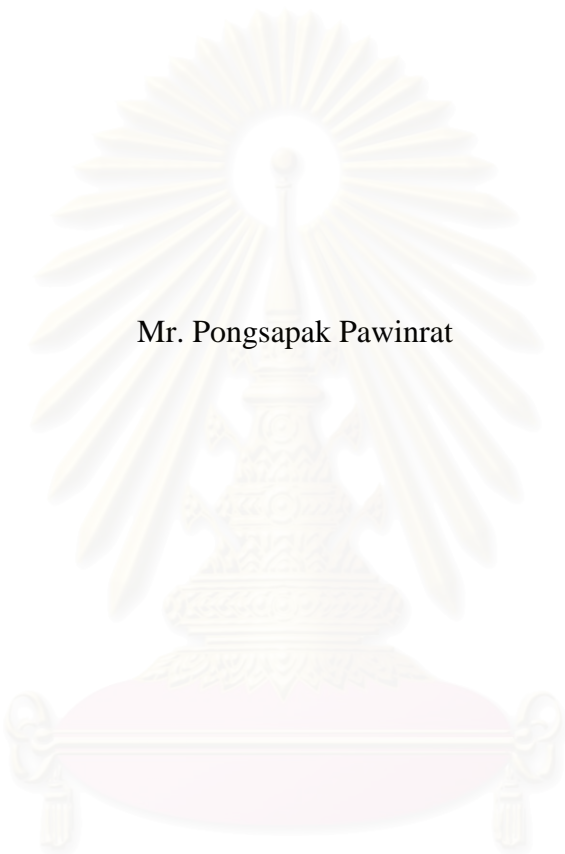
นาย พงศภัค ภวิลรัตน์

วิทยานิพนธ์นี้เป็นส่วนหนึ่งของการศึกษาตามหลักสูตรปริญญาวิศวกรรมศาสตรมหาบัณฑิต

สาขาวิชาวิศวกรรมเคมี ภาควิชาวิศวกรรมเคมี

คณะวิศวกรรมศาสตร์ จุฬาลงกรณ์มหาวิทยาลัย

ปีการศึกษา 2550

PHOTOCATALYTIC DEGRADATION OF METHYLENE BLUE BY Pt/ZnO AND
Au/ZnO CATALYSTS PREPARED BY FLAME SPRAY PYROLYSIS METHOD

Mr. Pongsapak Pawinrat

A Thesis Submitted in Partial Fulfillment of the Requirements

for the Degree of Master of Engineering Program in Chemical Engineering

Department of Chemical Engineering

Faculty of Engineering

Chulalongkorn University

Academic Year 2007

Thesis Title   PHOTOCATALYTIC DEGRADATION OF METHYLENE BLUE BY Pt/ZnO AND Au/ZnO CATALYSTS PREPARED BY FLAME SPRAY PYROLYSIS METHOD

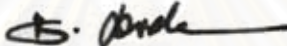By   Mr. Pongsapak Pawinrat

Field of study   Chemical Engineering

Thesis Advisor   Assistant Professor Joongjai Panpranot, Ph.D
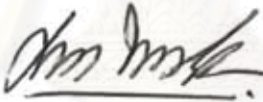
Thesis Co-Advisor   Assistant Professor Okorn Mekasuwandumrong, Ph.D.

Accepted by the Faculty of Engineering, Chulalongkorn University in Partial Fulfillment of the Requirements for the Master's Degree

.... Dean of the Faculty of Engineering

(Associate Professor Boonsom Lerdhirunwong, Dr.Ing.)

THESIS COMMITTEE

.... Chairman

(Associate Professor Supakanok Thongyai, Ph.D.)

.... Thesis Advisor

(Assistant Professor Joongjai Panpranot, Ph.D.)

.... Thesis Co-Advisor

(Assistant Professor Okorn Mekasuwandumrong, Ph.D.)

.... Member

(Akawat Sirisuk, Ph.D)

.... External Member

(Assistant Professor Worapon Kiatkittipong, Ph.D.)

พงศภัค ภวิลรัตน์ : การย่อยสลายโดยใช้แสงของเมธิลีนบลูด้วยตัวเร่งปฏิกิริยาแพลทินัม
ซิงค์ออกไซด์และทองซิงค์ออกไซด์ที่สังเคราะห์โดยวิธีเฟลมสเปรย์ไพโรไลซิส
(PHOTOCATALYTIC DEGRADATION OF METHYLENE BLUE BY
Pt/ZnO AND Au/ZnO CATALYSTS PREPARED BY FLAME SPRAY
PYROLYSIS METHOD) อ.ที่ปรึกษา: ผศ.ดร.จูงใจ ปั้นประณต, อ.ปรึกษาร่วม: ผศ.ดร.
โอกร เมฆาสุวรรณดำรง, 94 หน้า

ผงตัวเร่งปฏิกิริยาซิงค์ออกไซด์ขนาดนาโนเมตรที่มีขนาดผลึกต่างๆกัน(8.8 – 47.0 นาโน
เมตร) ตัวเร่งปฏิกิริยาทองซิงค์ออกไซด์และตัวเร่งปฏิกิริยาแพลทินัมซิงค์ออกไซด์ที่มีขนาดผลึก
ระดับนาโนเมตรถูกสังเคราะห์ขึ้นด้วยวิธีเฟลมสเปรย์ไพโรไลซิสและนำไปวิเคราะห์ด้วยเทคนิค
ต่างๆ เช่น เครื่องกระเจิงรังสีเอ็กซ์ (XRD), การดูดซับทางกายภาพด้วยไนโตรเจน (BET), อัลตร้า
ไวโอเลตและวิสิเบิลสเปกโทรสโกปี (UV-vis), อิเล็คตรอนสปินเรโซแนนซ์ (ESR), โฟโต้ลูมิเนส
เซนซ์ (PL), อะตอมมิกแอบซอร์พชันสเปกโทรสโกปี (AAS) และ กล้องจุลทรรศน์อิเล็กตรอน
แบบส่องผ่าน(TEM) โดยใช้การย่อยสลายเมธิลีนบลูด้วยแสงเป็นตัวประเมินประสิทธิภาพของ
ตัวเร่งปฏิกิริยาเทียบกับตัวเร่งปฏิกิริยาที่ใช้ทางการค้าเช่น ไทเทเนียมไดออกไซด์ P25 และ JRC
พบว่าตัวเร่งปฏิกิริยาซิงค์ออกไซด์ที่มีขนาดผลึก 47 นาโนเมตรให้ความว่องไวสูงที่สุดและการเพิ่ม
ขนาดของตัวเร่งปฏิกิริยาซิงค์ออกไซด์โดยการนำไปเผาที่อุณหภูมิสูงทำให้ประสิทธิภาพของตัวเร่ง
ปฏิกิริยาลดลง ผลที่ได้แสดงว่ามีผลของคุณภาพของผลึก พื้นที่ผิว ออกซิเจนวาเคนซีที่พื้นผิวและ
ความบกพร่องของพื้นผิวตัวเร่งปฏิกิริยาต่อประสิทธิภาพของตัวเร่งปฏิกิริยา อย่างไรก็ตามเมื่อขนาด
ผลึกของตัวเร่งปฏิกิริยาซิงค์ออกไซด์มีขนาดใหญ่กว่า 30 นาโนเมตรจะให้ประสิทธิภาพในการย่อย
สลายเมธิลีนบลูได้ดีกว่าทั้ง P25 และ JRC ในส่วนกรณีของทองและแพลทินัมซิงค์ออกไซด์ที่
เตรียมด้วยวิธีเฟลมสเปรย์ไพโรไลซิส ตัวเร่งปฏิกิริยาทองซิงค์ออกไซด์ที่มีทองอยู่ 3 เปอร์เซ็นต์โดย
น้ำหนักจะให้ประสิทธิภาพในการย่อยสลายเมธิลีนบลูได้ดีที่สุด ในทางตรงกันข้ามตัวเร่งปฏิกิริยา
แพลทินัมซิงค์ออกไซด์ไม่สามารถช่วยปรับปรุงประสิทธิภาพในการย่อยสลายเมธิลีนบลูให้ดีขึ้น
จากเดิมเนื่องจากชนิดของความสมดุลระดับเฟอร์มิของโลหะทั้งสองชนิดแตกต่างกันและความ
แตกต่างของขนาด/ความหนาแน่นของกลุ่มโลหะที่ตกสะสมอยู่บนตัวเร่งปฏิกิริยาซิงค์ออกไซด์

ภาควิชา...........วิศวกรรมเคมี...................... ลายมือชื่อนิสิต.........พงศภัค ภวิลรัตน์........
สาขาวิชา...........วิศวกรรมเคมี...................... ลายมือชื่ออาจารย์ที่ปรึกษา...........................
ปีการศึกษา...........2550...................... ลายมือชื่ออาจารย์ที่ปรึกษาร่วม....................

4970447321: MAJOR   CHEMICAL ENGINEERING

KEY WORD: ZINC OXIDE / FLAME SPRAY PYRORYSIS / GOLD / PLATINUM / PHOTOCATALYTIC OXIDATION

PONGSAPAK PAWINRAT: PHOTOCATALYTIC DEGRADATION OF METHYLENE BLUE BY Pt/ZnO AND Au/ZnO CATALYSTS PREPARED BY FLAME SPRAY PYROLYSIS METHOD THESIS ADVISOR: ASST. PROF. JOONGJAI PANPRANOT, Ph.D., THESIS CO-ADVISOR: ASST. PROF. OKORN MEKASUWANDUMRONG, Ph.D. 94 pp.

ZnO nanopowders with various crystallite sizes (8.8-47.0 nm) and nanocrystalline Au-ZnO and Pt-ZnO catalysts have been prepared by flame spray pyrolysis (FSP) method and characterized by X-ray diffraction (XRD), nitrogen adsorption, UV–vis spectroscopy, photoluminescence (PL), and transmission electron microscopy (TEM). Photodegradation of methylene blue (MB) was used to evaluate the photocatalytic performance of these powders. Commercial photocatalysts P25 and JRC were used for comparison purposes. The FSP-ZnO 47 nm exhibited the highest photocatalytic activity. Further increase of the ZnO crystallite size by annealing at high temperature, however, gradually decreased the photocatalytic activity of ZnO. The results suggest that there were competing effects of crystal quality, surface area, surface oxygen vacancies and surface defects on the photocatalytic activity of ZnO. However, ZnO with crystallite size $\geq$ 30 nm showed better performance than the commercial P25 and JRC TiO_2 photocatalysts. In the case of Pt/ZnO and Au/ZnO prepared by FSP, the experimental results suggest for an optimum content of 3 wt.% Au/ZnO that gave the best photocatalytic performance for MB degradation. Pt/ZnO, on the other hand, showed poor photocatalytic activity compared to the undoped ZnO due to the different type of Fermi level equilibration with diameter and the different metal cluster sizes/density deposited on ZnO.

Department...Chemical Engineering..... Student's signature...Pongsapak Pawinrat....

Field of study...Chemical Engineering...Advisor's signature........................

Academic year............2007...............Co-advisor's signature......................

ACKNOWLEDGEMENTS

The author would like to express his sincere gratitude and appreciation to his advisor, Assistant Professor Joongjai Panpranot, Ph.D., and his co-advisor Assistant Professor Okorn Mekasuwandumrong, Ph.D. from Faculty of Engineering and Industial Technology, Silpakorn University for invaluable suggestions, encouragement during his study, useful discussions throughout this research and especially, giving him the opportunity to present his research at 17th Thailand Chemical Engineering and Applied Chemistry Conference. In addition, the author would also be grateful to Associate Professor Supakanok Tongyai, as the chairman, Akawat Sirisuk and Assistant Professor Worapon Kiatkittipong as the members of the thesis committee.

He is indebted for financial supports of the Thailand Research Fund (TRF), TJTTP-JBIC, and the Graduate School of Chulalongkorn University are gratefully acknowledged.

Most of all, the author would like to express his highest gratitude to his parents who always pay attention to him all the times for suggestions and listen his complain. The most success of graduation is devoted to his parents.

The author would like to acknowledge with appreciation to Professor Piyasan Prasethdam for their kind suggestions on his research without hesitation

Finally, the author wishes to thank the members of the Center of Excellence on Catalysis and Catalytic Reaction Engineering, Department of Chemical Engineering, Faculty of Engineering, Chulalongkorn University for friendship and their assistance. To the many others, not specifically named, who have provided his with support and encouragement, please be assured that he thinks of you.
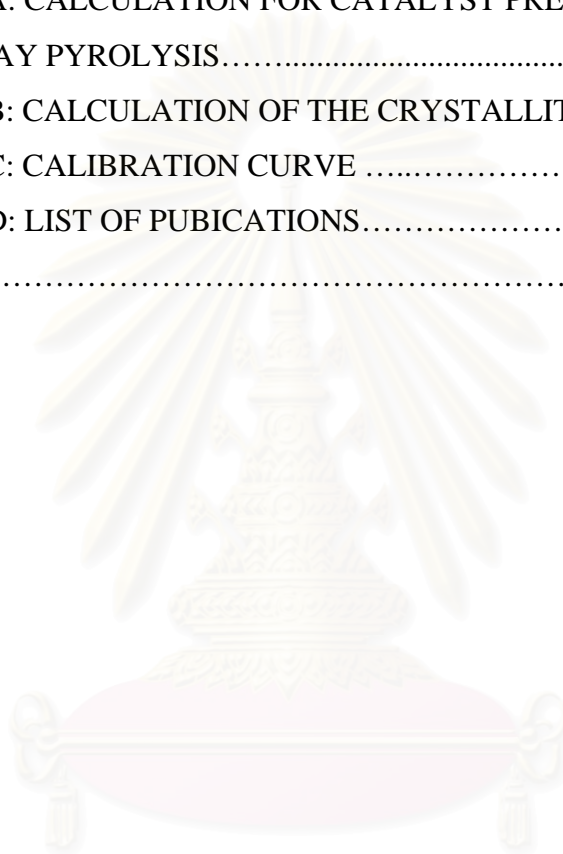
CONTENTS

Page

LIST OF TABLES

LIST OF FIGURES

CHAPTER I

INTRODUCTION

Wastewaters contaminated with residual dyes from textile, paper, and other industries are a cause of environmental problems. Conventional treatment of such wastewater generally involves coagulation/flocculation (Allegre *et al*.,2004 and Golob *et al*.,2005), electrocoagulation (Alinsafi *et al*.,2004) coagulation/carbon adsorption process (Papic *et al*.,2004) and so on. These methods, however, merely transfer dyes from the liquid- to the solid-phase, requiring further treatment and causing secondary pollution (Chakrabarti *et al*.,2004). In recent years, Oxidation is an alternative treatment strategy that can be applied to dyes and many other organics in wastewater and industrial effluents. In particular, semiconductor mediated photocatalytic oxidation can be conveniently applied towards the degradation of dye pollutants.

Photocatalytic degradation of organic pollutants in water and air using semiconductive particles, such as TiO_2 and ZnO, has attracted extensive attention in the past two decades (Hoffmann *et al*.,1995). In particular, ZnO has attracted much attention with respect to the degradation of various pollutants due to its high photosensitivity, non-toxic nature, stability, and wide band gap. While TiO_2 is widely employed as a photocatalyst, ZnO is a suitable alternative to TiO_2 as it has a similar band gap energy (3.2 eV) (Sakthivel *et al*.,2003), adsorbs over a larger fraction of UV spectrum and the corresponding threshold of ZnO is 425 nm (Behnajady *et al*.,2006), and higher photocatalytic efficiencies have been reported (Tanaka *et al*.,2000, Sharma *et al*.,1995, Khodja *et al*.,2001, Akyol *et al*.,2004, and Kavitha *et al*.,2007). It has also suggested that ZnO is a low cost alternative photocatalyst to TiO_2 for degradation of organics in aqueous solutions (Daneshvar *et al*.,2004)

When a semiconductor absorbs a photon of energy greater than or equal to the band gap energy, an electron may be promoted from the valence band to the conduction band leaving behind an electron vacancy or ''hole'' in the valence band. If charge separation is maintained, the electron and hole may migrate to the catalyst surface where they participate in redox reactions with adsorbed species. Hole vacancies may react with surface-bound H_2O or O^- to produce the hydroxyl radical

(OH). Free electrons may be picked up by oxygen to generate superoxide radical anions (O_2^-), which are the active species for oxidation. A limiting factor of the photocatalytic reaction is, therefore, recombination of the electron and hole prior to the superoxide activation step (Gerischer *et al*.,1991).

For semiconductor photocatalysts, particle size is an important parameter for controlling surface area and electronic structure. Under photo-excitation semiconductors undergo charge separation and initiate oxidation of the organic compounds at the interface. Nanostructured semiconductors are a potential candidate to photodegradation of organic compounds because of when the catalyst particle size is reduced down to a few nanometers, an elevate density of active sites for substrate adsorption and/or catalysis can be guaranteed, as small particles possess a significantly higher surface-to-volume ratio as compared to the bulk material. These characteristics thus offer the potential for gaining elevate performances photocatalysts. Furthermore, when the nanocrystal size is comparable or smaller than the bulk exciton diameter, the band-gap becomes size-dependent due to quantization effects (Alivisatos *et al*., 1996 and Henglein *et al*., 1995). This opens the opportunity of designing selective photochemical reactions by means of size modulating the electron–hole redox potentials, provided that a narrow size distribution is available. Moreover, an efficient photocatalytic process requires highly crystalline semiconductors to minimize electron–hole pairs loss owing to the trapping of either charge carriers at defect states (Hoffmann *et al*.,1995 and Beydoun *et al*.,1999).

Another approach to improve the efficiency of charge separation involves the combination of semiconductor substrate (ZnO) and metal cluster such as Ag, Au, Pd and Pt. It has been reported to give improved photocatalytic activity by trapping the photoinduced charge carriers, thereby improving the charge transfer processes (Subramanian *et al*.,2003, Jing *et al*.,2006, Wu *et al*.,2006, and Height *et al*.,2006). The noble metals of gold and platinum were used for the metal-ZnO formation because of high electron affinity behaviour (Sakthivel *et al*.,2004) and produce the highest Schotty barrier among the metals (Li *et al*.,2002). For ZnO n-type semiconductor (with a work function (ϕ_s) of ~ 4.3 eV) in contact with noble metals with a work function ϕ_m (Au: 5.1 eV and Pt: 5.65 eV) (Michaelson *et al*.,1977) $> \phi_s$, a Schottky barrier will form at the junction, facilitating electron capture.

There are various established routes for producing photocatalyst particles such as flame synthesis, chemical vapour deposition, precipitation, and alkoxide sol–gel methods (Teoh *et al.*,2005). The first method is particularly attractive as it is a relatively new method for the one-step production of nano-metal oxides. Flame synthesis in general and especially flame spray pyrolysis (FSP) is a fast simple process for the production of a wide variety of different nanoparticles with high production yield at low-cost (Pratsinis *et al.*,1998) and for the commercial photocatalyts TiO_2, e.g., Degussa P25. This method provides good control of particle size, particle crystal structure, and also can produce highly pure particles continuously without further subsequent processes such as drying, calcinations, and milling. The sizes of flame-made particles range from a few to several hundreds nanometers in diameter depending on process conditions (Jang *et al.*,2006).

1.2 Objective

The objective of this research is to investigate the characteristics and catalytic properties of zinc oxide (ZnO) with various crystallite sizes, zinc oxide supported platinum (Pt/ZnO), and zinc oxide supported gold (Au/ZnO) prepared by flame spray pyrolysis in photodegradation of methylene blue (MB).

1.3 Research Scopes

1. Preparation of ZnO various crystallite sizes by flame spray pyrolysis method (FSP) at different liquid/oxygen ratios (precursor flow rates; 3 and 8 mL/min and dispersion gas flow rates; 5, and 3 L/min) and Zn concentration precursor solution ranged from 0.3 to 1 mol/l.

2. Preparation of annealed-FSP ZnO from FSP ZnO (Zn concentration precursor solution 1 mol/l and precursor flow rates/dispersion gas flow rates ratio = 8/3) at temperature 750, 800, 835, 850, 900 ^{o}C and maintained for 1 h.

3. Preparation of 1 and 3 wt.% Pt/ZnO (Zn concentration precursor solution 0.8 mol/l and precursor flow rates/dispersion gas flow rates ratio = 8/3) by FSP method.

4. Preparation of 1, 3, and 5 wt.% Au/ZnO (Zn concentration precursor solution 0.8 mol/l and precursor flow rates/dispersion gas flow rates ratio = 8/3) by FSP method.

5. Characterization of the ZnO, Pt/ZnO, and Au-ZnO powders using several techniques such as X-ray Diffraction (XRD), Transmission Electron Microscopy (TEM) with Energy Dispersive X-ray analysis (EDX), UV–vis Spectrophotometer, N_2 Adsorption, Atomic Absorption Spectroscopy (AAS), Electron Spin Resonance Spectrometry (ESR).

6. Reaction study of ZnO, Pt-ZnO, and Au-ZnO in photocatalytic degradation of methylene blue and compare their performances to the reference commercial titania photocatalysts (P25 and JRC).

1.4 Research Methodology

Literature reviews

Synthesis of ZnO catalysts with various crystallite sizes by FSP method at different liquid/oxygen ratios and metal concentrations

Synthesis of 1 and 3 wt.% Pt/ZnO catalysts by FSP method

Synthesis of 1, 3, and 5 wt.% Au/ZnO catalysts by FSP method

Anneal FSP ZnO powders at 750, 800, 835, 850, 900°C

Catalyst characterization using XRD, PL N$_2$ Adsorption, TEM with EDX, AAS, and UV-Vis

Catalyst characterization using XRD, TEM, N$_2$ Adsorption, PL, and ESR

Commercial catalyst (TiO$_2$-P25 and TiO$_2$-JRC)

Reaction study in photocatalytic degradation of methylene blue

Data analysis

CHAPTER II

THEORY

2.1 Properties of Zinc Oxide

Zinc oxide is a II-VI compound semiconductor of which the ionicity resides at the borderline between covalent and ionic semiconductor. The crystal structures shared by zinc oxide are wurtzite, zinc blende, and rocksalt, as schematically shown in Figure 2.1. At ambient conditions, the thermodynamically stable phase is wurtzite. The zinc-blende structure can be formed only by the growth of ZnO on cubic substrate. The rocksalt structure may be obtained at relatively high pressure.

(a)   (b)   (c)
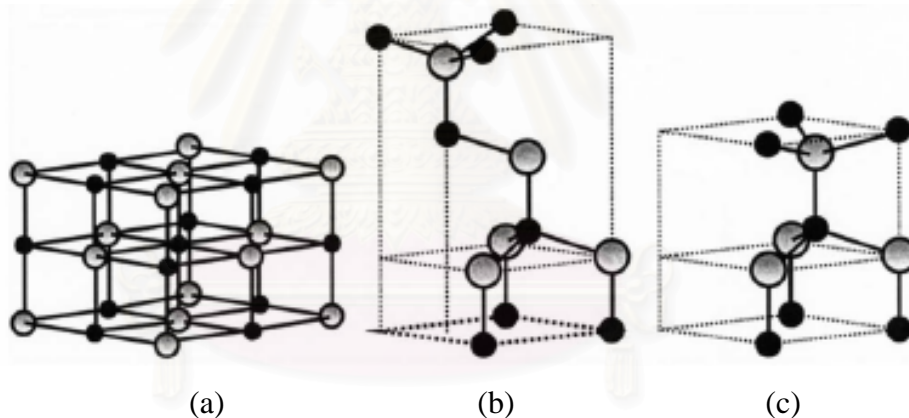
Figure 2.1   Stick and ball representation of zinc oxide crystal structures:
(a) cubic rocksalt, (b) cubic zinc blende, and (c) hexagonal wurtzite. The shaded gray and black spheres denote Zn and O atoms, respectively.

Zinc oxide is an n-type semiconductor with a band gap of 3.20 eV and the free exciton energy of 60 meV, which makes it very high potential for room temperature light emission. This also gives zinc oxide strong resistance to high temperature electronic degradation during operation. Therefore, it is attractive for many opto-electronic applications in the range of blue and violet light as well as UV devices for

wide range of technological applications**.** Zinc oxide also exhibits dual semiconducting and piezoelectric properties. The other properties are given in Table 2.1.

Table 2.1 Properties of wurtzite zinc oxide.

Property	Value
Lattice parameters at 300 K	
a	0.32495 nm
c	0.52069 nm
a/c	1.602 (ideal hexagonal structure is 1.633)
Density	5.606 g/cm^3
Melting point	1975 ^{o}C
Thermal conductivity	130 W/m.K
Linear expansion coefficient (/^{o}C)	a: 6.5 x 10^{-6}
	c: 3.0 x 10^{-6}
Static dielectric constant	8.656
Energy gap	3.2 eV, direct
Exciton binding energy	60 meV

Zinc oxide occurs in nature as mineral. Zinc oxide is prepared in industrial scale by vaporizing zinc metal and oxidizing the generated zinc vapor with preheated air. Zinc oxide has numerous industrial applications. It is a common white pigment in paints. It is used to make enamel, white printing ink, white glue, opaque glasses, and floor tiles. It is also used in cosmetics, pharmaceutical applications such as antiseptic and astringent, dental cements, batteries, electrical equipments, and piezoelectric devices. Other applications are the use as flame retardant, and UV absorber in plastics. Nevertheless, the current major application of zinc oxide is in the preparation of most zinc salts.

2.2 Flame Spray Pyrolysis (FSP) (R. Strobel *et al*., 2004 and H. D. Jang *et al*., 2006)

Flame synthesis is a relatively new method for the one-step production of supported noble metal catalysts and catalysts in general. Flame aerosol synthesis is a cost-effective and versatile process for the controlled production of nanoparticles. In flame reactors, the energy of a flame is used to drive chemical reactions of precursor compounds that result in the formation of clusters which further grow by coagulation and sintering in the hot flame environment to nanometer-sized product particles.

There are two primary types of the flame aerosol process for the synthesis of those nanoparticles. One is a flame assisted vapor-to-particle conversion process that is called as flame vapor synthesis (FVS). The other is a flame assisted liquid droplet-to-particle conversion process called as flame spray pyrolysis (FSP). The FVS process is the best choice for the synthesis of solid nanoparticles of single-component and binary systems such as metals, semiconductors, simple oxide, nitrides, etc. However, the FVS process requires the use of volatile precursors. High production rate is possible when highly volatile precursors are available, and because the vapor phase precursors can be purified more easily than solid or liquid precursors, the FVS process allows the generation of materials with ultrahigh purities. Unfortunately, a disadvantage of the FVS process is that the synthesis of high-purity volatile precursors is complicated and expensive.

In general, the FVS is more complex to design and operate than the FSP because the FVS requires a gas-handling subsystem for the controlled introduction of vapor phase reactants. In contrast, the FSP systems require only an atomizer. The FSP has the major advantages that can handle materials containing a large number of elements and that aqueous solution of precursors can be used to produce multi-components oxide nanoparticles.

In conventional spray pyrolysis, the solution is atomized into a hot wall reactor where the aerosol droplets undergo evaporation and solute concentration within the droplet, drying, thermolysis of the precipitate particle at higher temperature to form a microporous particle, and, eventually a dense one by sintering. The advantages of FSP include the ability to dissolve the precursor directly in the fuel,

simplicity of introduction of the precursor into the hot reaction zone (e.g. a flame), and flexibility in using the high-velocity spray jet for rapid quenching of aerosol formation.

When producing nano-catalyst using a high temperature flame, the particle collection technique has to be chosen. One solution is to collect the material directly on the substrate either inside the flame or very close to it. The variety of operational details includes several physical parameters such as e.g. particle size of the material. When nanosized particles are deposited on the substrate, it is assumed that coarsening of the material may take place, including partial sintering, neck formation and even full coalescence of the particles, especially if the temperature is sufficiently high.
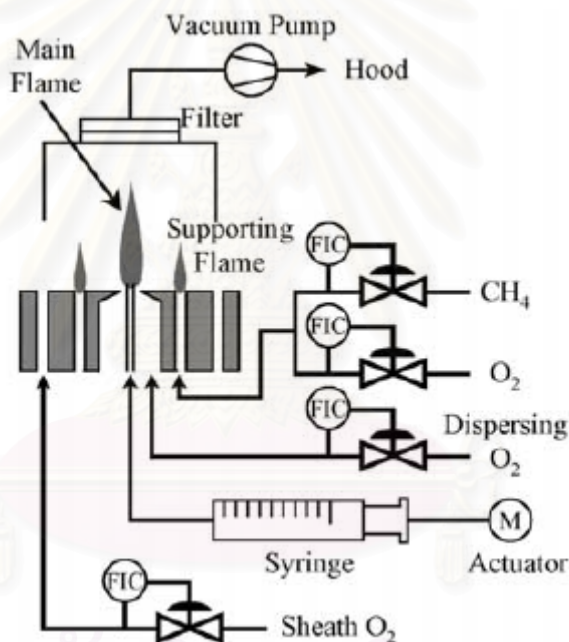
Figure 2.2 Schematic of the FSP process for ZnO particle synthesis.

2.3 Photocatalytic process (A. mills *et al*., 2002, D. Robert *et al*., 2001, E. Bizani *et al*., 2006, and S. Senthilkumaar *et al*., 2005)

The primary photocatalytic process occurs upon irradiation of a semiconductor catalyst. A semiconductor is characterized by an electric band structure in which the highest occupied energy band, called valence band, and the lowest band, called conduction band, are separated by band gap. The magnitude of the fixed energy gap

between the electrochemically populated valence band and the largely vacant condition band govern the extent of thermal population of the conduction band in its intrinsic state. The band gap also defines the wavelength sensitivity of the semiconductor to irradiation. When a photon of the energy higher or equal to the band gap energy is absorbed by a semiconductor particle, an electron from the valence band is promoted to the conduction band with simultaneous generation of an electronic vacancy or "hole" (h^+) in the valence band.

In most materials that are electrically conductive, i.e., metal, two types of carriers, electron (e^-) and holes (h^+), immediately recombine on the surface or the bulk of particle in a few nanosecond and the energy is dissipated as heat (equation 3.1). On semiconductor such as titanium dioxide, however , they survive for period of time to allow these carriers be trapped in surface state where there can react with donor (D) such as surface-bound H_2O or OH^- or acceptor (A) species A adsorbed such as oxygen or hydrogen peroxide or close to the surface of the particle (equation 3.2, 3.3 and 3.4).

Recombination $\quad\quad e^-_{CB} + h^+_{VB} \rightarrow heat$ $\quad\quad\quad\quad\quad$ (3.1)

Photo excitation $\quad\quad semiconductor + hv \rightarrow e^-_{CB} + h^+_{VB}$ $\quad\quad$ (3.2)

$\quad\quad\quad\quad\quad\quad\quad h^+_{VB} + D \rightarrow D^+$ $\quad\quad\quad\quad\quad\quad\quad\quad$ (3.3)

$\quad\quad\quad\quad\quad\quad\quad e^-_{CB} + A \rightarrow A^-$ $\quad\quad\quad\quad\quad\quad\quad\quad$ (3.4)
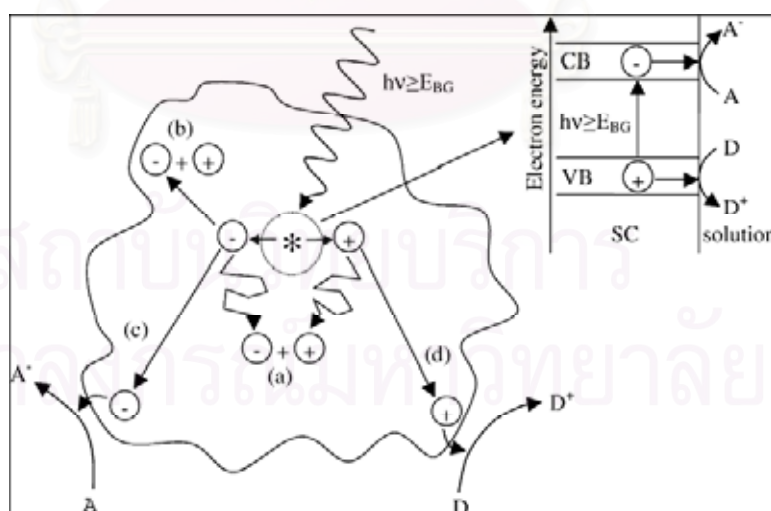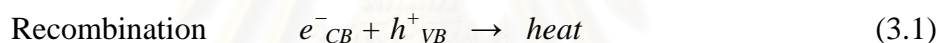
Figure 2.3 Schematic illustration of the major processes that occur on a semiconductor particle upon absorption of a photon of ultra-band gap light, i.e. $hv > E_{BG}$.

This is followed by formation of extremely reactive radicals (like $OH^\bullet$) at the semi-conductor surface and/or a direct oxidation of the polluting species (R).

$$H_2O + h^+{}_{VB} \rightarrow H^+ + OH^\bullet \tag{3.5}$$

$$OH^-{}_{ads} + h^+{}_{VB} \rightarrow OH^\bullet \tag{3.6}$$

$$R + h^+{}_{VB} \rightarrow R^{+\bullet} \rightarrow degradation\ products \tag{3.7}$$
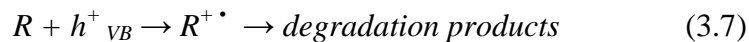
The ejected electrons react with electron acceptors such as oxygen adsorbed or dissolved in water (equation 3.8).

$$(O_2)_{ads} + e^-{}_{CB} \rightarrow O^-{}_2{}^\bullet \tag{3.8}$$

The addition of H_2O_2 (equation 3.9) and (equation 3.10) increases the concentration of $OH^\bullet$ radical since it inhibit the e^-, h^+ recombination.

$$O^-{}_2{}^\bullet + H^+ \rightarrow HO_2{}^\bullet \tag{3.9}$$

$$2HO_2{}^{\bullet\bullet} \rightarrow H_2O_2 + O_2 \tag{3.10}$$

H_2O_2 is considered to have two functions in the photocatalytic degradation. It accepts a photogenerated conduction band electron thus promotes the charge separation (equation 3.11) and it also forms $OH^\bullet$ (equation 3.12).

$$H_2O_2 + e^-{}_{CB} \rightarrow OH^- + OH^\bullet \tag{3.11}$$

$$H_2O_2 + O^-{}_2{}^\bullet \rightarrow OH^- + OH^\bullet + O_2 \tag{3.12}$$

Oxidation of the organic reactant via successive attacks by $OH^\bullet$ radicals (equation 3.13).

$$R + OH^\bullet \rightarrow R'^{\bullet\bullet} + H_2O \tag{3.13}$$
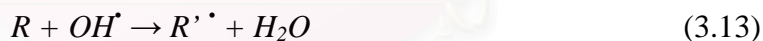
However, photodegradation of dyes over semiconductor may also occur by photosensitization. In this process the colored compound absorb radiation in the visible range to yield an excited state of the dye, dye*. The dye transfers an electron to the semiconductor particle to produce a conduction band radical and a dye radical cation, which, in turn, reduces molecular oxygen to form a superoxide anion. Eventually, the dye cation radical reacts with molecular oxygen or with an oxygenated radical species to yield a mineralized product.

$$dye + h\nu \longrightarrow dye^* \tag{3.16}$$

$$dye^* + semiconductor \longrightarrow dye^+ + semiconductor(e^-{}_{CB}) \tag{3.17}$$

$$O^-{}_2{}^\bullet + e^-{}_{CB} + 2H^+ \longrightarrow H_2O_2 \tag{3.18}$$

$$dye^+ + O_2 \ (and \ / \ or \ O_2^- \ and \ / \ or \ OH^\bullet \ ) \longrightarrow \ mineralized \ products \quad (3.19)$$
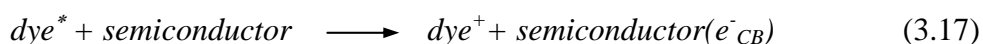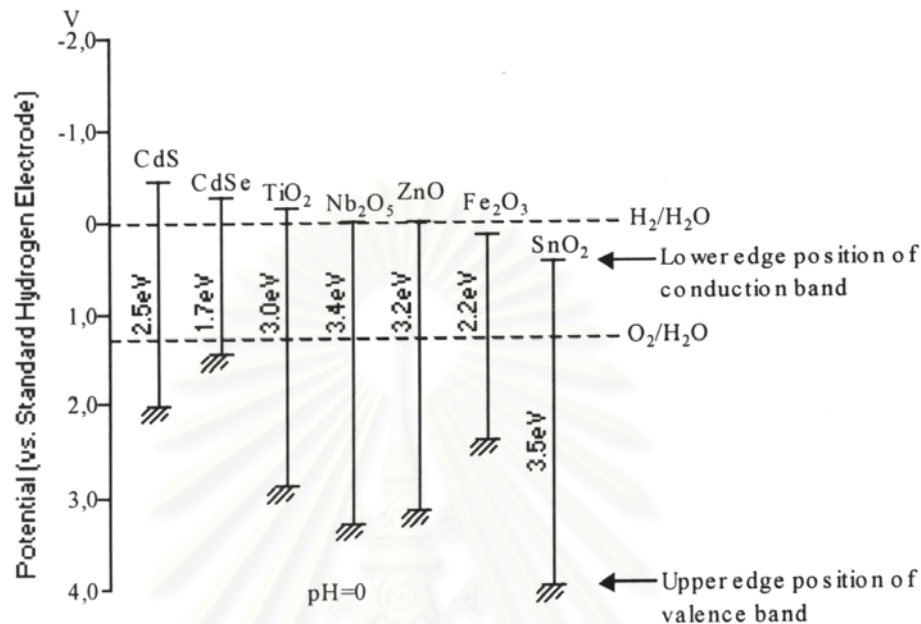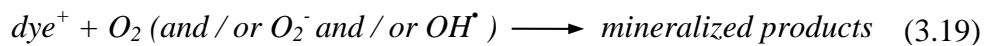
Figure 2.4 Band-edge energies of typical semiconductors (Benedix et al., 2000).

2.4 Defect structure of crystal material

Defect can be broadly divided into two groups: stoichiometric defects in which the crystal composition is unchanged on introducing the defects and non-stoichiometric defects, which are a consequence of a change in crytal composition. It is well-known that the surface reactivity is not the same when the surface is regular (stoichiometric) or reduced (substoichiometric) (Calatayud *et al*., 2004). These defects affect the chemical properties of solids in very significant ways, and play a key role in controlling the rate at which soids react. As a general rule, the most favorable adsorption modes on a perfect surface preserve the electronic gap of the oxide and can be understood in terms of acid-base reaction mechanism; on the contrary, the adsorption on a reduced surface implies a redox mechanism in order to restore the gap that is decreased or has disappeared by effect of them reduction. Two such defects particular importance is the Frenkel and schottky defects. Only point defect that

concerns our work thus large-scale imperfections will not mentioned in details. The details of point defects are following.

2.4.1 Vacancies: Schottky defects

Consider the simplest crystal defect, namely that of an atomic site becoming vacant, with the missing atom migrating to the crystal surface. This process will be energetically unfavorable, costing the system a change in energy. The defects arising from balanced populations of cation and anion vacancies are now known as schottky defects.

Schottky defects are frequently represented in Figure 2.5. This represents a Schottky defect in a crystal structure of the sodium chloride type, the projection shown in this diagram representing a (100) plane. In this case, Schottky defect will consist of the appropriate numbers of the cation and anion vacancies to form an electrically neutral total.
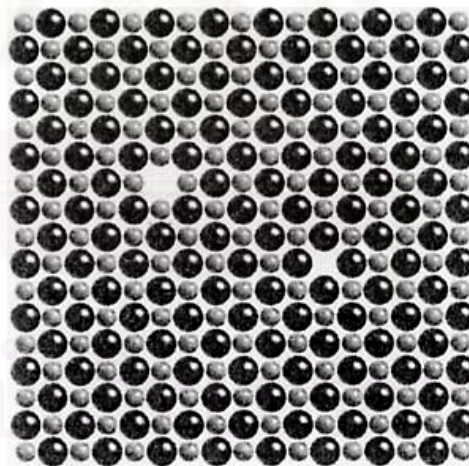
Figure 2.5 Cation and anion charge-balanced shottky defects in NaCl. The metal atoms are smaller than the non-metal atoms. The defect consists of vacancies on both metal and non metal sites.

2.4.2 Interstitial defects: Frenkel defects

In crystals that not pack with high efficiency, it is possible for atoms to occupy sites that are normally vacant, called interstitial sites. The Frenkel defect contains interstitial-vacancy pairs, formed as a result of the transfer of atoms or ions into interstitial sites, leaving vacancies behind at the regular sites. This process is illustrated in Figure 2.6.
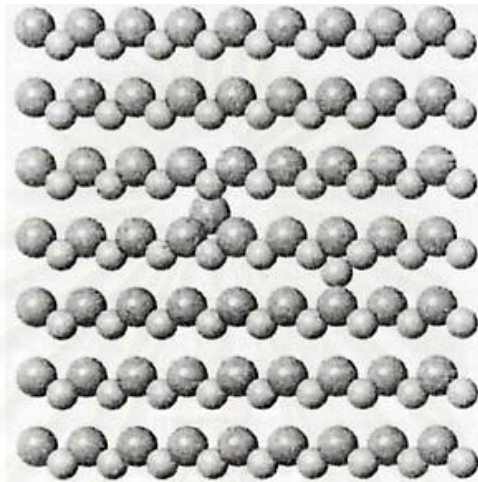
Figure 2.6 Pair of charge-balanced Frenkel defects in AgI. The metal atoms are smaller than the non-metal atoms. The defects consist of equal numbers of vacancies on either the metal or non-metal or non metal sub-lattice and interstitial ions of the same type.

2.5 Role of Semiconductor-metal (Au and Pt) nanocomposites for enhance the photocatalytic reaction rate (F. B. Li *et al*., 2002)

Platinum and gold can produce the highest Schottky barrier among the metals that facilitate electron capture. The capture of electrons by Platinum and gold is postulated to produce a longer electron–hole pair separation lifetime, and therefore hinder the recombination of electron–hole pairs and enhance the transfer of holes and possibly electrons to O_2 adsorbed on the semiconductor surface. Afterwards, excited electrons migrate to the metal, where they become trapped and the electron–hole pair recombination is suppressed. Therefore, many investigations have reported the enhancement of photoactivities in both liquid and gas phases results from depositing platinum and gold.
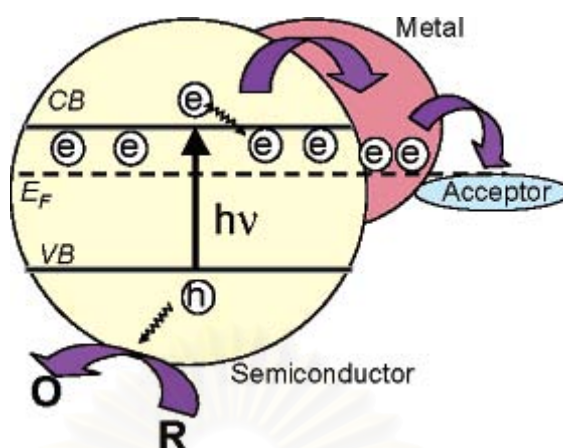
Figure 2.7 illustrates the mediating role of noble metals in storing and shuttling photogenerated electrons from the semiconductor to an acceptor in a photocatalytic process.

2.6 Fermi-Level Equilibration of the metal nanoparticles (Au,Pt) brought in contact with the irradiated semiconductor(ZnO). (V. Subramanian *et al*., 2003)

The interaction is ohmic type in the case of ZnO-Pt as the Pt capping merely facilitates discharge of the photogenerated electrons into the electrolyte. Such an interaction between semiconductor and metal has been proved to be beneficial for improving the efficiency of many photocatalytic reactions (for example, water splitting reactions in Pt-capped TiO_2.

The ZnO-Au system on the other hand shows unusual charge storage behavior. As illustrated in Scheme 2.5, the electrons transferred to gold nanoparticles are stored within the metal nanocore. Increased electron density within the nanoparticle thus shift the Fermi-level toward more negative potentials. The transfer of electrons to metal nanocore continues until the Fermi level reaches close to the conduction band edge of ZnO. Each injected electron within the gold nanoparticle is capable of shifting the Fermi level by 0.1 V. Thus, the storage of multiple electrons during the charge equilibration with the semiconductor can produce a significant shift in the Fermi level, thus driving the overall Fermi level to more negative potential. An independent photoelectrochemical experiment carried out with TiO_2/Au films show a shift in the Fermi-level of 150 mV. Thus, the Fermi level equilibration with a noble metal layer

has its own benefit toward improving the photoelectrochemical and photocatalytic performance.
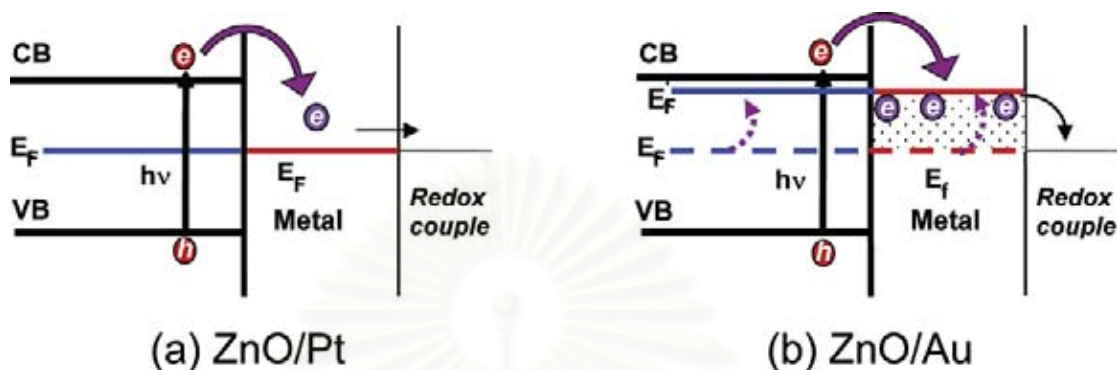
Figure 2.8 Photoinduced Charge Separation and Charge Distribution in (a) Pt/ZnO and (b) Au/ZnO Nanocomposites. E_F and $E_{F'}$ Represent Fermi Levels Attained before and after Charge Distribution.

2.7 PL mechanism of semiconductor nanomaterials (Liqiang *et al*., 2006)

A semiconductor is characterized by an electronic band structure in which the highest-occupied energy band, called valence band (VB), and the lowest-occupied energy band, called conduction band (CB), are separated by a band gap, i.e. a region of forbidden energies. There are some sub-bands in the band gap, which are closely related to surface defects and surface states. The band gap energy (Eg) is the energy difference between the CB bottom and VB top. To discuss the relationships between the PL spectrum and photocatalytic activity, only the PL phenomena of excited energy higher or equal to the band gap energy of semiconductor are presented here. Fig. 2.9 shows the main photophysical processes of semiconductors excited by light with no less than the band gap energy, and there are four main processes. Process I is the photo-excited process in which the electrons from the VB are promoted to the CB with different energy levels to become different excited states, with simultaneous generation of holes (h+) in the VB under irradiation. However, the excited electrons in the CB easily come back to the VB via a certain course to recombine with the holes, since they are very unstable. During the recombination process of photo-induced charge carriers, a certain amount of chemical energy can be released, which

would further transform possibly to heat or to light energy. The light energy can be dissipated as radiation, which results in a luminescence emission of semiconductor material, called the PL phenomenon of the semiconductor. In fact, the excited electrons with different energy levels in the CB easily transfer firstly to the CB bottom via non-radiative transitions; subsequently, the processes II, III or IV will possibly occur. Process II is the band–band PL process in which the electron transitions from the CB bottom to the VB top can take place, with simultaneously releasing of energy as radiation. In this case, the photon energy actually equals to the band gap energy. However, the photon energy can be higher than the band gap energy sometimes, which mainly results from the transitions of higher energy of excited electrons from the CB band to the VB top directly. This PL signal is also attributed to a kind of band–band PL phenomenon. Process III is the excitonic PL process in which the non-radiative transitions of excited electrons from the CB bottom to different sub-bands (or surface states) occur first, and subsequent radiative transitions from the sub-band to the VB top can take place. The energy of the radiative photon, which is the energy difference between the sub-band and VB top, is lower than the band gap energy. In general, the excitonic PL signal mainly results from surface oxygen vacancies and defects of semiconductors. Moreover, the nanoparticle size is fine, so that the average distance which the electrons can move freely to is very short. These factors can make surface oxygen vacancies and defects very easily bind electrons to form excitons in the sub-band. Thus, the excitonic PL process can occur, and the smaller the nanoparticle size, the larger the oxygen vacancy and defect content, the higher the probability of exciton occurrence and the stronger the PL signal. In addition, the excited electrons at the CB bottom can come back to the VB directly or indirectly by non-radiative transitions, which is the process IV.

The above discussions demonstrate that only photophysical processes II and III can give rise to PL phenomena, the former is attributed to the band–band PL, and the latter is attributed to the excitonic PL. According to PL attributes, the band–band PL spectrum can directly reflect the separation situation of photo-induced charge carriers, viz. the stronger the band–band PL signal, the higher the recombination rate of photo-induced carriers. The excitonic PL spectrum cannot directly reflect the separation situation of photo-induced carriers. However, it can reveal some important

information about surface defects, oxygen vacancies and surface states, which can strongly affect photocatalytic reactions.
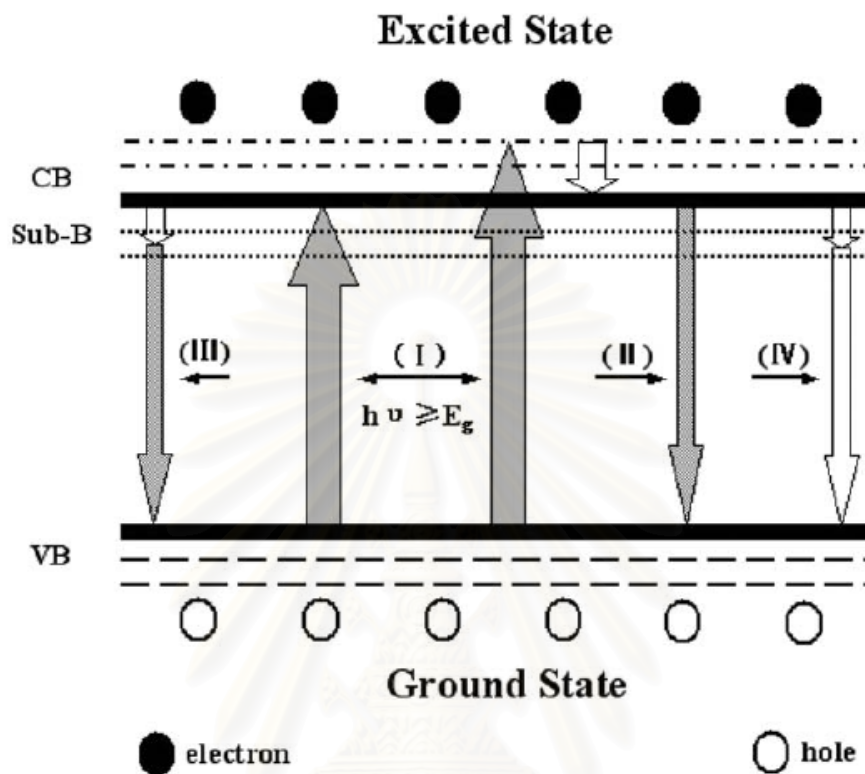
Fig. 2.9 Main photophysical processes of a semiconductor excited by light with equal to or higher than band gap energy (I—photo-excited process; II—band–band PL process; III—excitonic PL process; IV—non-radiative transition process).

CHAPTER III

LITERRATURE REVIEWS

3.1 Flame Spray Pyrolysis (FSP)

T. Tani et al. (2002) studied zinc oxide (ZnO) nanoparticles made by flame spray pyrolysis (FSP) of zinc acrylate–methanol–acetic acid solution. The effect of solution feed rate on particle specific surface area (SSA) and crystalline size was examined. The average primary particle diameter can be controlled from 10 to 20 nm by the solution feed rate. All powders were crystalline zincite. The primary particle diameter observed by transmission electron microscopy (TEM) was in agreement with the equivalent average primary particle diameter calculated from the SSA as well as with the crystalline size calculated from the X-ray diffraction (XRD) patterns for all powders, indicating that the primary particles were rather uniform in diameter and single crystals. Increasing the solution feed rate increases the flame height, prolonging particle residence time in the flame and therefore coalescence and/or surface growth was enhanced, resulting in larger primary particles. Compared with the other gas phase-made ZnO nanoparticles, the FSP-made powder exhibits some of the smallest and most homogeneous primary particles. The FSP-made powder also shows almost the same BET equivalent average primary particle diameter but higher crystallinity than a sol–gel derived powders. On the other hand, a sol–gel method using reversed micelles was considered better than FSP for close particle property control of ZnO nanoparticles.

T. Tani et al. (2005) studied zinc oxide (ZnO) and magnesia (MgO) powder made by flame spray pyrolysis of zinc acetate and magnesia acetate dissolved in methanol–water mixture respectively. The product powder were characterized by nitrogen adsorption, infrared adsorption (IR), X-ray diffraction (XRD) and transmission electron microscopy. The effect of solvent on powder characteristics were examined by changing methanol content (X = 1 – 0.4) in the solvent. Polyhedral

aggregates of nanoparticles were formed from the solvents with methanol content > 0.6 for both ZnO and MgO, suggesting complete evaporation of the metal spcies in the flame and particle formation in gas phase, whereas using the solvent with methanol content of 0.4 suppressed the evaporation, leading to particle formation both in gas and liquid phases, resulting in a mixture of nanoparticles and large particle also for both cases. The criteria for the complete evaporation were not changed in these experimental condition for ZnO and MgO synthesis in spite of the different physical properties of these oxides as well as their precursors. The XRD and IR spectra showed hydroxylation of MgO, which can be explained by the larger Gibbs energy change for hydroxylation in MgO than in ZnO. The d_{BET}, d_{XRD} and d_{TEM} (only for Z100) were in agreement with each other for Z100, Z80 and Z60, suggesting single crystalline primary particles, whereas the d_{BET}, d_{XRD} and d_{TEM} (only Z100) were not consistent for M100, M80 and M60. Hydoxylation of MgO may influence the product particle characteristics.

W. Y. Teoh et al. (2005) studied TiO_2 and Pt/TiO_2 nanoparticles prepared by a one-step flame spray pyrolysis (FSP) process that resulted in mostly anatase (69–85 wt%) powders with controlled specific surface area and crystallite size. These particles displayed better activity than Degussa P25 TiO_2 for photocatalytic mineralisation of sucrose. Co-precipitation of Pt on TiO_2 during FSP increased the rutile content and slightly increased the specific surface area. Close control over Pt deposit size during this process was possible by varying the Pt concentration in the feed precursor. The dispersion of the Pt was high, 45–77% (at 4.0–0.1 atom% Pt) and corresponded to metal deposit size of 2.5–1.4 nm, respectively. An optimum photocatalytic activity was observed at 0.5 atom% Pt loading. At loadings higher than optimum, hole recombination with negatively charged Pt deposits may decrease the adsorption of negatively charged oxidants and light shielding effects may also hinder the process. At low Pt loading (0.1 atom% Pt), the activity was lower than that of FSP-made TiO_2 since the high photocurrent density of the Pt deposits increased the electron-hole recombination. The deposit size was also too small to establish sufficient electrical contact for efficient interfacial charge transfer between the photocatalysts and sucrose. Additional studies on the photocatalytic mineralisation of sucrose under

oxygen enriched conditions reaffirmed the postulation that both FSP-made TiO_2 and improved Pt/TiO_2 photocatalysts favoured a reductive pathway which was different and faster than the pathway followed when using Degussa P25 TiO_2.

H. D. Jang et al. (2006) studied synthesis of silica (SiO_2) nanoparticles from sprayed droplets of tetraethylorthosilicate (TEOS) by the flame spray pyrolysis. The particles were characterized by TEM, XRD, and BET method. TEOS concentration, maximum flame temperature, and residence time of reactants in the flame were chosen as key experimental variables for the control of the particle morphology, and average particle diameter. Spherical SiO_2 nanoparticles ranged from 12 to 47 nm in average particle diameter were produced by through all the experiments. As the TEOS concentration in the flame increased from $5.5 * 10^{-6}$ to $2.2 * 10^{-5}$ mol/l, the average particle diameter of the SiO_2 nanoparticles increased from 12 to 45 nm maintaining narrow particle size distribution. Larger SiO_2 nanoparticles were synthesized as hydrogen and oxygen flow rate decreased in the flame, respectively. Crystal structure of all the product SiO_2 nanoparticles was found as amorphous.

W. Y. Teoh et al. (2007) studied visible light-active Fe-doped TiO_2 that was prepared by a one-step flame spray pyrolysis (FSP) technique. Introduction of Fe into TiO_2 matrix by flame synthesis was effective in extending the particle photoresponse to the visible regime ($\lambda > 400$ nm). At the same time, it also enhances transformation to rutile. Being a bottom-up approach, the short residence time coupled with a high quenching rate during the FSP process was found to be an excellent method in synthesising homogeneous Fe-doped TiO_2 solid solutions with high Fe solubility. The reported solubility of up to Fe/Ti = 0.05 in this work is significantly higher than the Fe/Ti ~ 0.01 commonly found for particles synthesised by wet techniques followed by high temperature calcination. Doping Fe above its solubility limit was accompanied by formation of amorphous structure and a UV–vis optical band centred at 490 nm. A slight shift in the XRD rutile (1 1 0) peak and a decrease in specific surface area were also observed at high Fe loadings. The Fe-TiO_2 sample was able to mineralise oxalic acid under visible light. This is also accompanied by a unique Fe-leaching and re-adsorption properties. Extraction of Fe (III) from photocatalyst

surface was found to take place even in the dark to form a Fe (III)-oxalate complex. The complex is photolysed under visible light irradiation leaving behind Fe (II) ions. Here, the presence of visible light-active Fe-TiO$_2$ is important to reoxidise the adsorbed Fe (II) to Fe (III) to sustain the photoreaction under visible light. A high extent of oxalic acid mineralisation (70%) for 10 ppm (as carbon) of oxalic acid was observed for Fe-doped TiO$_2$ with Fe/Ti ratio of 0.05 compared to just 50% for the same bulk amount of aqueous Fe (III) and TiO$_2$. In addition, most dissolved Fe ions are readsorbed back on the Fe-TiO$_2$ particles at the end of the oxalic acid oxidation reaction, thereby minimizing the loss of Fe and rendering its re-usability. On the other hand, a mixture of dissolved Fe (III) and bare TiO$_2$ resulted in significant loss of unadsorbed Fe after each run. Hence it is not surprising that the Fe-doped TiO$_2$ particles exhibited reproducible mineralization rates even after 5 repeated runs whereas the latter saw deteriorating rates after every run. The UV–vis absorption spectrum of Fe-doped TiO$_2$ was also found to be unchanged despite repeated photocatalytic runs.

Table 3.2 Summary of methylene blue (MB) photocatalysis studied

Catalyst	Particle size (nm)	Initial MB concentration	Catalyst concentration	Reaction condition	Conversion (60 min; %)	Rate constant	Reference
TiO_2 (sol-gel)	30	12.5 mg/L	1212 mg/L	110 W UV lamp	32	0.018 min^{-1}	X.Z. Li et al. (2001)
3% WOx-TiO_2 (sol-gel)	23	12.5 mg/L	1212 mg/L	110 W UV lamp	66	0.106 min^{-1}	X.Z. Li et al. (2001)
TiO2 (sol-gel)	18.3	12 mg/L	1212 mg/L	125 W UV lamp	n.d.	0.0955 min^{-1}	F. B. Li et al. (2002)
0.5% Au-TiO_2 (sol-gel)	19.4	12 mg/L	1212 mg/L	125 W UV lamp	n.d.	0.1752 min^{-1}	F. B. Li et al. (2002)
0.5% Au^{3+}-TiO_2 (photo-reduction)	11.8	12 mg/L	1212 mg/L	125 W UV lamp	n.d.	0.1944 min^{-1}	F. B. Li et al. (2002)
TiO2 (sol-gel)	20 - 30	15 mg/L	1212 mg/L	110 W UV lamp	n.d.	0.0672 min^{-1}	F. B. Li et al. (2002)
0.75%Pt–TiO_2 (photo-reduction)	40 - 80	15 mg/L	1212 mg/L	110 W UV lamp	n.d.	0.104 min^{-1}	F. B. Li et al. (2002)
ZnO	147	50 mg/L	1000 mg/L	16 W UV lamp	55	n.d.	S. Chakrabati et al. (2004)

3.2 Photocatalytic degradation of dye by ZnO and TiO$_2$

S. Chakrabati et al. (2004) investigated photocatalytic degradation (PCD) of Methylene Blue and Eosin Y with ZnO. A 16 W lamp was the source of UV-radiation in a batch reactor. In addition to the removal of colors, the reaction simultaneously reduced the COD suggesting that the dissolved organics were at least partially oxidized.The PCD efficiency has been generally, found to increase with increase in catalyst loading up to a limiting value, decrease in initial concentration, increase in airflow rate, pH, and UV light intensity. Of the two dyes, Methylene Blue was degraded faster. The rate equation for the PCD followed pseudo-first order kinetics and the rate-constants were determined, using Langmuir–Hinshelwood model. The kinetic model was based on hydroxyl radical attack. The efficiency of the once-recycled catalyst was reduced to 58.9% of the fresh catalyst.

Y. J. Jang et al. (2005) studied ZnO nanoparticles and its nano-crystalline particles on the photocatalytic degradation of methylene blue. ZnO nanoparticles and its nano-crystalline particles were synthesized from sprayed droplets of an aqueous zinc nitrate solution by flame spray pyrolysis and spray pyrolysis assisted with an electrical furnace, respectively. Photoactivity of the ZnO nanoparticles of 20 nm in the average diameter was higher than that of the ZnO nano-crystalline particles of 20 nm in mean grain size throughout the present experiments. The photocatalytic degradation of methylene blue using a commercial TiO$_2$ photocatalyst (P25) of 20 nm in average particle diameter was also measured to compare between the TiO$_2$ and the ZnO. As the reaction occurred, the TiO$_2$ was more effective on the degradation of methylene blue than the ZnO until 40 min. But no difference after 1 h. The efficiency of photodegradation of methylene blue using two kinds of ZnO photocatalyst has been generally found to increase with increase in catalyst loading and decrease in initial concentration regardless of particle morphology in the present study.

R. Kavitha et al. (2007) investigated the effects of substrate temperature and deposition time on particle size, phase composition, and texture of titania films using combustion flame pyrolysis method. The resulting TiO$_2$ film has anatase at low

substrate temperature, rutile at high substrate temperature and a mixture of these two phases at intermediate temperatures. Fine primary particles are obtained at low precursor concentrations. ZnO films are deposited from sprayed droplets by using this process and comparison of TiO_2 and ZnO films on the photocatalytic degradation of remazol brilliant blue is investigated. The photoactivity of ZnO film is higher than those of TiO_2 (anatase) and TiO_2 (rutile) films. This study proves that flame spray pyrolysis is a suitable method to deposit ZnO and TiO_2 films for photocatalytic application.

3.3 Effect of crystallite size of on the photocatalytic activity of ZnO

A.C. Dodd et al. (2006) studied a three-stage process consisting of mechanical milling, heat treatment, and washing has been used to manufacture nanoparticulate ZnO powders with a controlled particle size and minimal agglomeration. By varying the temperature of the post-milling heat treatment, it was possible to control the average particle size over the range of 28–57 nm. The photocatalytic activity of these powders was characterized by measuring the hydroxyl radical concentration as a function of irradiation time using the spin-trapping technique with electron paramagnetic resonance spectroscopy. It was found that there exists an optimum particle size of approximately 33 nm for which the photocatalytic activity is maximized. The existence of this optimal particle size is attributable to an increase in the charge carrier recombination rate, which counteracts the increased activity arising from the higher specific surface area for a sufficiently small particle size.

J. Liqiang et al. (2006) studied the ZnO nanoparticles are prepared by a precipitation process, and also are characterized by means of the modern testing techniques such as XPS, ESR, SPS and PL. The activity of the as-prepared ZnO is evaluated in the photocatalytic oxidation of gas phase n-C_7H_{16}. The relationships of surface oxygen vacancies (SOV) with photoluminescence (PL) and photocatalytic performance are discussed in details. The results show that the smaller the particle size, the larger the SOV content, the stronger the PL signal, the higher the

photocatalytic activity, indicating that the SOV, PL and photocatalytic activity have inherent relationships. This was because of the reasons that the PL signal is attributed to the free and binding excitons resulting from the SOV, while the SOV is favorable for a photocatalytic oxidation reaction since the SOV can easily capture the photoinduced electrons, and the captured electrons had strong interactions with the adsorbed oxygen. In addition, the surface states of ZnO nanoparticles, arising from the SOV and oxygen species, are very abundant.

H. Wang et al. (2007) studied ZnO powders with various size scales (mean diameter size: 10, 50, 200 and 1000 nm) have been prepared by two different preparation methods, thermal evaporation method and chemical deposition method, and examined as photocatalysts for the UV-induced degradation of methyl orange in water solution. ZnO nanoparticle with diameter size 50 nm prepared by thermal evaporation method showed the highest photocatalytic activity. In addition, the tetrapod ZnO nanopowders had the higher efficiency than irregular ZnO particles. However, the smallest 10 nm ZnO nanoparticle prepared by chemical deposition method indicated the lower efficiency contrast to 200 nm ZnO powders prepared by thermal evaporation method. The results indicated preparation method was the decisive factor rather than size and morphology. The experiments were conducted with 50 nm ZnO powders to investigate its photocatalytic activity under various process conditions. The results indicated that the catalyst loading, pH values and the initial dye concentration affected the degradation efficiency of ZnO powders obviously. We learned that the photodegradation efficiency is enhanced with the increase of catalyst loading and the reverse effect is obtained with the increase of initial dye concentration in our experiments. The photocatalytic decomposition of methyl orange was most efficient in the solution at pH 10.

3.4 Photocatalytic degradation of dye by using metal-doped ZnO and TiO$_2$

F. B. Li et al. (2002) investigated the mechanism of photosensitization and the recombination of excited electron–hole pairs that were affected by depositing platinum (Pt) on the surface of titanium dioxide (TiO$_2$). A new catalyst of Pt–TiO$_2$ was prepared by a photoreduction process. Being model reactions, the photocatalytic oxidation of methylene blue (MB) and methyl orange (MO) in aqueous solutions using the Pt–TiO$_2$ catalyst was carried out under either UV or visible light irradiation. The experimental results indicate that an optimal content of 0.75%Pt–TiO$_2$ achieves the best photocatalytic performance of MB and MO degradation. The interaction of Pt and TiO$_2$ was investigated by means of UV–Vis absorption spectra, photoluminescence emission spectra, and X-ray photoelectron emission spectroscopy. The Pt^0, Pt^{2+} and Pt^{4+} species existing on the surface of Pt–TiO$_2$, and the Ti^{3+} species existing in its lattice may form a defect energy level. The Pt impurities, including Pt, Pt(OH)$_2$, and PtO$_2$, and the defect energy level absorb visible light more efficiently in comparison with the pure TiO$_2$ and hinder the recombination rate of excited electron–hole pairs.
.

F. B. Li et al. (2002) studied gold ion-doped TiO$_2$ and gold-deposited TiO$_2$ by measuring the photo-activity, X-ray diffraction (XRD) spectra, photoluminescence (PL) spectra, and X-ray photo-electron spectra (XPS) of gold, oxygen and titanium. The results showed that anatase phase was the main component and that the electronic structure and interfacial electron transfer were significantly influenced by the presence of either gold ion or gold. The photo-activity was quantified in terms of methylene blue (MB) photo-degradation. As a result, the presence of gold ion in TiO$_2$ lattices or gold on TiO$_2$ surface greatly enhanced their photo-activity. The optimum molar content of gold ion doping and gold deposition was 0.5%. XPS measurements showed that there were Au, Au$^+$, or Au^{3+} species in/on gold modified TiO$_2$, and that Ti3$^+$ species formed in TiO$_2$ lattice owing to the presence of gold or gold ion. PL measurements showed that the recombination of electrons/holes was greatly hindered owing to gold or gold ion. The lower recombination of electron–hole pairs which had

a good agreement with the greater photo-activity might be attributable to the presence of defect energy level, gold impurity energy level, or the presence of gold or gold ion.

Sakthive et al. (2002) studied Pt, Au and Pd deposited TiO_2 have been prepared and characterised by surface analytical methods such as surface area, XRD, and scanning electron micrograph and photophysical characterisation by diffuse reflectance spectroscopy. The photocatalytic activity of the doped catalysts was ascertained by the photo-oxidation of leather dye, acid green 16 in aqueous solution illuminated with low-pressure mercury lamp (~254 nm). Surface area of TiO_2 decreases with increasing metal dopant mainly due to blocking of fine capillaries of parent TiO_2 surface by metal film islands which are proved to be invisible in X-ray analysis. The photonic efficiency of Pt deposited TiO_2 is almost comparable to Au/ TiO_2 but higher than Pd/ TiO_2. The metal-doped TiO_2 systems show an absorption threshold extended into the visible region. It is obvious that the metal clusters give rise to localised energy levels in the bandgap of TiO_2 into which the valence band electrons of TiO_2 are excited at wavelength longer than 400 nm. The highest photonic efficiency was observed with metal deposition level of less than 1 wt%. The photonic efficiency increases with increase in the metal loading up to an optimum level due to the effect of decreasing recombination of electron and hole. Above the optimum metal doping, the dopants behave as electron/hole recombination centers and hence lower photonic efficiency has been observed in all metal-doped TiO_2 catalysts. It is concluded that defect sites on the TiO_2 surface are necessary for the photo-oxidation of pollutants. These defect sites are identified as Ti^{3+} and are necessary for adsorption and photoactivation of oxygen. It is also evident that Ti^{3+} sites covered with metal particles are detrimental to the photo-oxidation of acid green 16.

M. J. Height et al. (2006) studied high surface area Ag-ZnO catalysts that were made by flame spray pyrolysis (FSP) and characterized by X-ray diffraction (XRD), nitrogen adsorption, UV–vis spectroscopy and electron microscopy (SEM and transmission electron microscopy (TEM)) combined with energy dispersive X-ray spectroscopy (EDXS) for elemental mapping. The Ag loading (1–5 at.%) controlled the Ag cluster size from 5 to 25 nm but did not influence the ZnO crystal size.

Photodegradation of 10 ppm methylene blue (MB) solution was used to evaluate the performance of these FSP-made Ag-ZnO showed higher photocatalytic activity than wet-made and reference titania powders. An Ag loading between 1 and 3 at.% gave the fastest photodegradation of MB and the reaction rate decreased at higher Ag loadings. This is consistent with the presence of discrete Ag clusters leading to retarded recombination of the photoinduced electron–hole pairs. Decreasing activity at higher loadings is likely to arise from decreasing surface availability on the particles for reactant adsorption and light absorption. The photocatalytic performance was improved for flame-made materials made at longer high-temperature residence times in the flame. The latter particles exhibited improved crystallinity, as measured by UV–vis absorption and XRD.

J. J. Wu et al. (2006) studied photodegradation of methyl orange (MO) under 365-nm irradiation over the nc-Au/ZnO nanorod composites and compared with those of the ZnO nanorods and the ZnO film. The ZnO nanorods and the ZnO film were deposited on the Si substrates using chemical vapor deposition. Photosyntheses of Au nanoparticles on the ZnO nanorods were conducted in $HAuCl_4$/ethanol solutions under 365-nm irradiation. The diameters and the densities of the Au nanoparticles formed on the surface of ZnO nanorods are tunable through varying the $HAuCl_4$ concentration and the irradiation period. The apparent first-order rate constant of MO photodegradation using the ZnO nanorods is two orders magnitude larger than that using the ZnO film. It is suggested that the enhancement is ascribed to the higher surface area and the charge separation by the surface Fermi-level pining effect. The enhancement of the photocatalytic activity for degradation of MO is achieved by loading Au nanoparticles with sizes smaller than 15 nm on the ZnO nanorods and is more pronounced as the size of the Au nanoparticles is reduced to 5 nm. However, the photocatalytic activity of the nc-Au/ZnO nanorod composite is much lower than that of the Zn nanorods when the diameter of the nc-Au is enlarged to 30 nm. The dramatic decrease of the photocatalytic activity of the 30-nm nc-Au/ZnO nanorod composites is suggested to be ascribed to the scattering of the incident irradiation by the Au nanoparticles and the formation of Schottky barriers at the junction of the ZnO nanorods and the Au nanoparticles.

Table 3.2 Summary of methylene blue (MB) photocatalysis studied

Catalyst	Particle size (nm)	Initial MB concentration	Catalyst concentration	Reaction condition	Conversion (60 min; %)	Rate constant	Reference
TiO_2 (sol-gel)	30	12.5 mg/L	1212 mg/L	110 W UV lamp	32	0.018 min^{-1}	X.Z. Li et al. (2001)
3% WOx-TiO_2 (sol-gel)	23	12.5 mg/L	1212 mg/L	110 W UV lamp	66	0.106 min^{-1}	X.Z. Li et al. (2001)
TiO2 (sol-gel)	18.3	12 mg/L	1212 mg/L	125 W UV lamp	n.d.	0.0955 min^{-1}	F. B. Li et al. (2002)
0.5% Au-TiO_2 (sol-gel)	19.4	12 mg/L	1212 mg/L	125 W UV lamp	n.d.	0.1752 min^{-1}	F. B. Li et al. (2002)
0.5% Au^{3+}-TiO_2 (photo-reduction)	11.8	12 mg/L	1212 mg/L	125 W UV lamp	n.d.	0.1944 min^{-1}	F. B. Li et al. (2002)
TiO2 (sol-gel)	20 - 30	15 mg/L	1212 mg/L	110 W UV lamp	n.d.	0.0672 min^{-1}	F. B. Li et al. (2002)
0.75%Pt–TiO_2 (photo-reduction)	40 - 80	15 mg/L	1212 mg/L	110 W UV lamp	n.d.	0.104 min^{-1}	F. B. Li et al. (2002)
ZnO	147	50 mg/L	1000 mg/L	16 W UV lamp	55	n.d.	S. Chakrabati et al. (2004)

Catalyst	Particle size (nm)	Initial MB concentration	Catalyst concentration	Reaction condition	Conversion (60 min; %)	Rate constant	Reference
TiO_2 (solution combustion)	10	100 ppm	1000 mg/L	Sunlight	60	$0.8*10^{-1}$ mol/L min	K. Nagaveni et al. (2004)
ZnO (FSP)	20	15 mg/L	1000-1500 mg/L	20 W UV lamp	86 - 99	n.d.	Y. J. Jang et al. (2005)
TiO_2 (sol-gel)	12	10 mg/L	125 mg/L	125 W UV lamp	n.d.	0.033 min^{-1}	S. Senthilkumaar et al. (2005)
ZnO (FSP)	17	10 ppm	300 mg/L	8 W UV lamp	37	0.47 h^{-1}	M. J. Height et al. (2006)
3% Ag-ZnO (FSP)	17	10 ppm	300 mg/L	8 W UV lamp	53	0.79 h^{-1}	M. J. Height et al. (2006)
Ti-Ag-US (solgel via ultrasonic irradiation)	44	10 mg/L	0.2-0.533 g/L	125 W UV lamp	n.d.	0.0517-0.3147 mg/L min	S. Senthilkumaar et al. (2006)

n.d. = not determined

Comments on the previous studies

From the previous studied, FSP process is an elegant process to produce highly crystalline nano-particles using high synthesis temperature and rapid cooling rate. This technique has the advantage of being able to utilize a broader spectrum of liquid precursors. Excellent controls over particle characteristics during flame synthesis including particle purity, surface areas, crystalline phases, and morphologies make it an ideal method for photocatalyst preparation. For many environmental applications, TiO_2 is the most widely employed as a photocatalyst while ZnO is a suitable alternative to TiO_2 as it has a similar band gap energy and higher photocatalytic efficiencies. In photocatalytic reaction the particle size of photocatalyst have affected on the photocatalytic activity. However, the effect of particle size on the photoactivity of ZnO has been addressed by a few approaches. In case of addition noble metal into support semiconductor, many investigations have reported that platinum and gold can be used for TiO_2 photocatalytic activity enhancement. They can improve photocatalytic activity by producing the highest Schotty barrier among the metals to facilitate the electron capture. However, the characteristics and catalytic properties of flame-made Pt/ZnO and Au/ZnO in photodegradation of methylene blue have never been studied. Thus, it is the aims of this study to synthesize Pt/ZnO and Au/ZnO by flame spray pyrolysis and investigate their catalytic behavior in photodegradation of methylene blue.

CHAPTER IV

EXPERIMENTAL

4.1 Catalyst Preparation

4.1.1   Materials

The chemical used in this study are specified as follows in Table 4.1.

Table 4.1 Chemicals used in catalyst preparation.

Chemical	Supplier
Platinum acetylacetonate	Fluka
Gold (III) chloride trihydrate (Aldrich; 99.9+ %)	Aldrich
Zinc naphthanate (< 50 % in mineral spirits)	Aldrich
Ethanol (99.9 vol.%)	J. T. Baker
Xylene (99.8 vol.%)	MERCK
Acetonitrile (99.5 vol.%)	Fluka

4.1.2   Flame-synthesis of ZnO

Synthesis of ZnO nanopowders with various particle sizes were carried out using a spray flame reactor (Tani, *et al*.,2002). Zinc naphthanate (Aldrich ;< 50 % in mineral spirits) was used as zinc precursor. The precursor was dissolved in ethanol (J.T. Baker; 99.9%). To obtained different ZnO crystallite sizes during particle synthesis, precursor solution ranged from 0.3 to 1 mol/l and liquid precursor feed rates varied from 3 to 8 ml/min were fed to the flame by a syringe pump. Precursors were dispersed with 3-5 l/min oxygen forming fine spray droplets. The conditions of synthesis are presented in Table 4.2. The pressure drop at the capillary tip was maintained at 1.5 bar by adjusting the orifice gap between the nozzle. The reactor was water-cooled to avoid evaporation or decomposition of the precursor within the feed lines. The spray flame was surrounded and ignited by a concentric premixed

methane/oxygen pilot flame (CH_4 1.5 L/min, O_2 3.0 L/min) that was sheathed further by flowing oxygen (25 L/min) through a sintered metal plate ring (8 mm wide, starting at a radius of 8 mm). The powder particles were collected on a glass–fiber filter (GF/D Whatman; 257 mm diameter) with the aid of a vacuum pump.

Table 4.2   Synthesis condition of ZnO with various crystallite sizes by the flame spray pyrolysis method.

Metal concentration (Molar)	Precursor flow rate (mL/min)	Dispersion oxygen flow rate (L/min)	Crystallite size d_{xrd} (nm)
0.3	3	5	8.8
0.3	8	3	19.4
0.5	8	3	30.0
0.8	8	3	40.7
1	8	3	47.0

4.1.3 Synthesis of annealed-ZnO

Annealing of the powders was performed in a Carbolite CWF1300 temperature programmed oven., ZnO powders with the crystallite size of 47 nm produced by FSP method was heated in air at 10°C/minute to a desired temperature (750, 800, 835, 850, 900 $^{\circ}$C) and maintained at that temperature for 1 h to form larger particles. The relationship between the annealing temperature and average size of the ZnO nano-crystallite is summarized in Table 4.3.

Table 4.3 Synthesis synthesis of annealed ZnO

Metal concentration (Molar)	Precursor flow rate (mL/min)	Dispersion flow rate (L/min)	Annealing Temperature ($^{\circ}$C)	Crystallite size d_{XRD} (nm)
1	8	3	750	52.6
1	8	3	800	67.1
1	8	3	835	80.3
1	8	3	850	90.6
1	8	3	900	103.5

4.1.4 Flame-synthesis of Au-ZnO and Pt-ZnO

Syntheses of Au-ZnO and Pt-ZnO powders were carried out using a spray flame reactor. Zinc naphthanate (Aldrich; < 50 % in mineral spirits) and Gold (III) chloride trihydrate (Aldrich; 99.9+ %) were used as zinc and gold precursors. The precursors were dissolved in ethanol (J.T. Baker; 99.9%) with total metal concentration maintained at 0.8 M while the gold concentration ranged between 0 and 5 wt.%. Using a syringe pump, 8 mL/min of precursor solution was dispersed into fine droplets by a gas-assist nozzle fed by 3 L/min of oxygen designated as a 8/3 flame. The pressure drop at the capillary tip was maintained at 1.5 bar by adjusting the orifice gap between the nozzle. The reactor was water-cooled to avoid evaporation or decomposition of the precursor within the feed lines. The spray flame was surrounded and ignited by a concentric premixed methane/oxygen pilot flame (CH_4 1.5 L/min, O_2 3.0 L/min) that was sheathed further by flowing oxygen (25 L/min) through a sintered metal plate ring (8 mm wide, starting at a radius of 8 mm). The powder particles were collected on a glass–fiber filter (GF/D Whatman; 257 mm diameter) with the aid of a vacuum pump.

Pt-ZnO was prepared using the same conditions as that of Au-ZnO but raw materials for preparation of a liquid-phase precursor was changed from Gold (III) chloride trihydrate to Platinum acetylacetonate (Fluka) and solvent for dissolved Platinum acetylacetonate from ethanol to xylene (MERCK; 99.8 vol.%)/acetonitrile (Fluka; 99.5 vol.%) mixtures 70/30 vol%. However, 5 wt.% Pt-ZnO has not been synthesized because the precursor solution mixture contained higher metal concentration than that the solvent can dissolve.

4.2 The Reaction Study in Photocatalytic Degradation of Methylene Blue

4.2.1 Instrument and Apparatus

1. Reactor beaker (pyrex) 250 ml.
2. UV lamp Phillips 15 W.
3. Magnetic stirrer plate

4. Plastic syringe 10 ml.

5. Stirrer bar

6. Centrifuged

7. Plastic cuvette 5 ml.

8. UV–vis spectrophotometer (Perkin Elmer Lambda 650)

### 4.2.2 Chemicals and Reagents

The chemicals and reagents used in the reactions are shown in Table 4.4.

Table 4.4 The chemicals and reagents used in the reaction.

The chemicals and reagents	Supplier
Methylene blue	Unilab, Asia Pacific Specialty Chemicals Limited
De-ionized water	Millipore Waters Milli Q purification unit

4.2.3 Phtocatalytic Degradation of Methylene blue Procedure

A basic aniline dye, MB was used as a probe molecule to evaluate the photocatalytic activities. The formula of MB is as following:
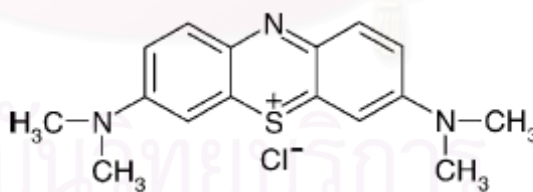
Fig 4.1 Structure of methylene blue.

For the photocatalytic test of methylene blue degradation, The photocatalytic reaction was conducted at room temperature under UV light 2 x 15 W UV tube predominantly emit at 365 nm (Philips) with the average light intensity 4.7×10^{-4} W cm^{-2} on the reaction beaker (pyrex) at a distance of 6 cm from the lamp. The reaction was carried out with 20 mg of catalyst dispersed in 200 ml of 10 ppm methylene blue aqueous solution. Prior to irradiation, the suspension was magnetically stirred in the dark for 30 min to establish the adsorption/desorption equilibrium of methylene blue.

Approximately 3.5 ml of the sample was withdrawn every 10 min. Before analysis, the aqueous sample was centrifuged to remove any suspended solid catalyst particles. The residual concentration of methylene blue was measured at 665 nm using the UV–vis spectrophotometer in a liquid cuvette configuration with de-ionized water as reference. The percentage of degradation was calculated by using the equation given below:

$$\text{Degradation (\%)} = \frac{(C_0 - C)}{C_0} \times 100 \tag{4.1}$$

In which C_0 is the initial dye concentration and C is the dye concentration after the treatments.

4.3 Catalyst Characterization

4.3.1 X-ray Diffraction (XRD)

The bulk crystal structure and chemical phase composition are determined by diffraction of an X-ray beam as a function of the angle of the incident beam. The XRD spectrum of the catalyst is measured by using a SIEMENS D500 X-ray diffractometer and Cu K$_\alpha$ radiation. The crystallite size (d_{XRD}) is calculated from Scherrer's equation.

4.3.2 Transmission Electron Microscopy (TEM)

The particle morphology was observed using JEOL Model JEM-2010 transmission electron microscope (TEM) operated at 200 keV Energy dispersive X-ray analysis (EDX) at National metal and materials technology center.

4.3.3 Nitrogen Adsorption

The BET powder-specific surface area, pore volume, and average pore diameter were measured by N$_2$ physisorption using a Micromeritics ASAP 2000 automated system and the Brunauer–Emmet–Teller (BET) method. Each sample was degassed under vacuum at $<1 \times 10^{-5}$ bar in the Micromeritics system at 300 $^\circ$C for 3 h prior to N$_2$ physisorption.

4.3.4 Photoluminescence (PL)

To study the recombination of electrons–holes, photoluminescence measurement was carried out on a Fluorescence spectrophotometer (Perkin–Elmer LS-50) at center of nanoscience and nanotechnology faculty of Science Mahidol University by using a Xenon lamp as the excitation source at room temperature. The sample was dispersed in ethanol using ultrasonic bath and the excitation wavelength used in photo luminescence (PL) measurement was 325 nm.

4.3.5 Atomic Absorption Spectroscopy (AAS)

The content of metal in Au-ZnO and Pt-ZnO samples was determined by Atomic Absorption Flame Emission Spectroscopy (varian spectra A800) at the Department of science service Ministry of science technology and environment. The metal loading of the samples is expressed in grams of metal per gram of sample: wt% metal = $m_{metal}/(m_{metal} + m_{ZnO})$ x 100.

4.3.6 UV-visible Absorption Spectroscopy (UV-vis)

To determine the light absorption band edge, the UV–Vis Absorption Spectra of the photocatalysts were obtained in the range of 300–900 nm using a UV–Vis scanning spectrophotometer (Perkin - Elmer lampda 650, λ between 300-900 nm and step size 1 nm), while $BaSO_4$ was used as refferance.

4.3.7 Electron Spin Resonance Spectrometry (ESR)

The defected surface O^{2-} ion vacancies are investigated by the Electron Spin Resonance Spectrometer (ESR) at STREC. It was conducted on ESR spectrometer of JEOL,model JES-RE2X on ES-IPRIT program with the X band Microwave unit and frequency : 8.8-9.6 GHz. The cavity is cylindrical and it was operating in TE $_{011}$ mode.

CHAPTER V

RESULTS AND DISCUSSION

The main topic of this study involves an attempt to improve the photocatalytic efficiency of ZnO by varying crystallite size and doping second metal (Pt and Au). In this chapter, the experimental results and discussion are described and divided into two major parts.

The first part describes the effect of ZnO crystallite size on the photocatalytic degradation of methylene blue by FSP made ZnO and annealed-FSP ZnO.

The second part describes the photocatalytic degradation of methylene blue by Pt/ZnO and Au/ZnO catalysts prepared by FSP method.

## 5.1 Effect of ZnO crystallite size on the photocatalytic activity of ZnO prepared by flame spray pyrolysis method.

5.1.1 Particle characterization

5.1.1.1 X-ray Diffraction (XRD)

The results from XRD analysis of all the ZnO powders are shown in Figure 5.1a-5.1b. The average crystallite size (d_{XRD}) of ZnO was estimated from the full-width half-maximum breadth of the (101) diffraction peak using the Scherrer equation.

Figure 5.1.a shows XRD patterns of the FSP made ZnO powders; (a) ZnO 8.8 nm, (b) ZnO 19.4 nm, (c) ZnO 30.0 nm, (d) ZnO 40.0 nm, and (e) ZnO 47.0 nm. All of the indexed peaks in the obtained spectrum are well matched with that of bulk ZnO (JCPDS Card No. 36–1451) possesses wurtzite hexagonal phase. No other diffraction peaks or amorphous phase was detected. It was found that the diffraction peaks intensities increased and the peaks became sharper as the precursor concentration and

the ratio of fed liquid and dispersion gas flow rates through the nozzle increased. These results imply the growth of ZnO crystallite and it becomes more crystalline. Figure 5.1b similarly shows the XRD patterns of ZnO powders prepared by FSP after annealed at different temperature; (f) ZnO 52.6 nm, (g) ZnO 67.1 nm, (h) ZnO 80.3 nm, (i) ZnO 90.6 nm, and (j) ZnO 103.5 nm. All the powders exhibited similar XRD patterns as those in Figure 5.1a. However, the intensity of diffraction peaks for annealed FSP ZnO powders were not changed much when annealing temperature increased. It could be due to the high crystallinity of the starting FSP-made sample (47 nm).

(a) FSP made ZnO   (b) annealed-FSP ZnO
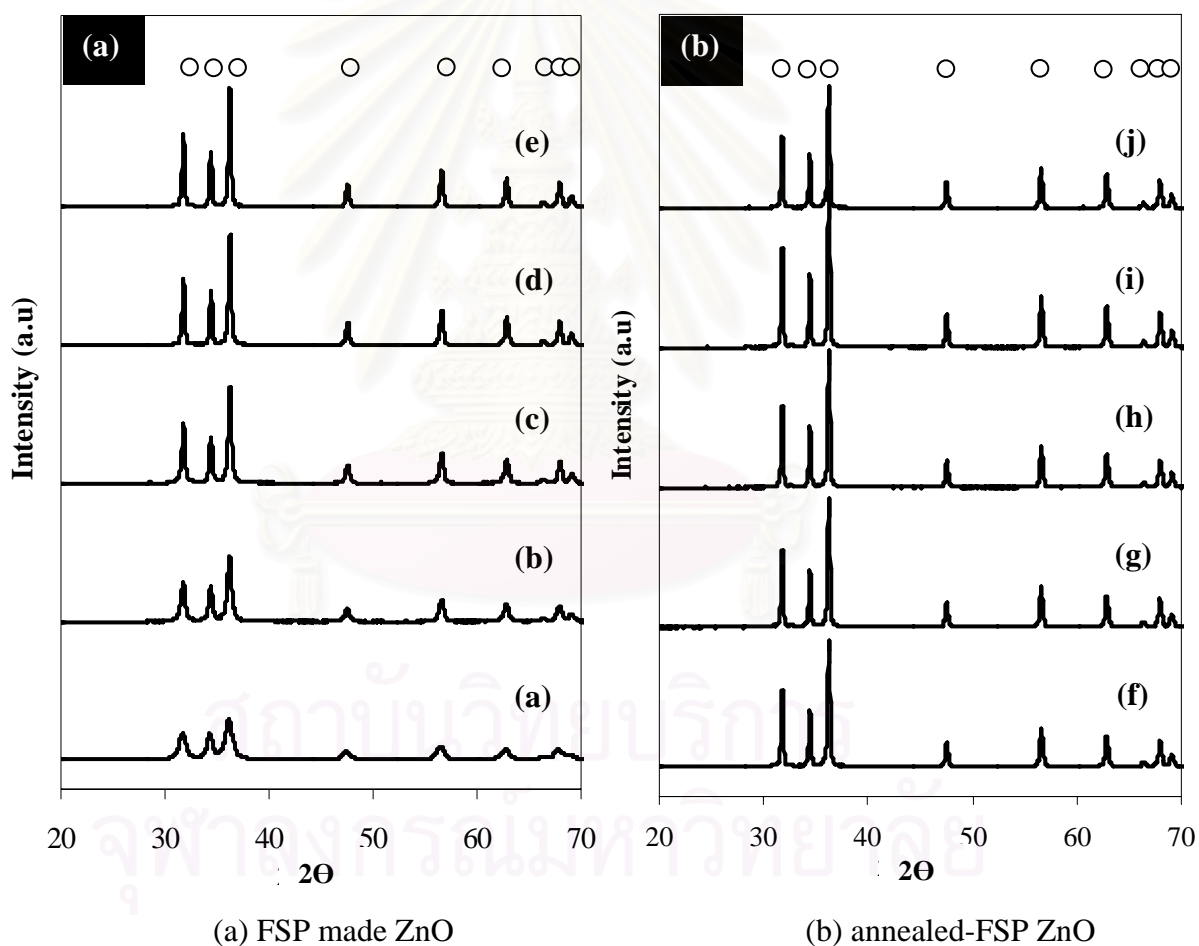
Figure 5.1 XRD patterns of as-prepared flame-made ZnO various crystallite sizes (a) 8.8 nm, (b) 20 nm, (c) 30 nm (d) 40 nm, and (e) 47 nm and Flame-made ZnO with annealed in air at different temperature various crystallite sizes (f) 52.6 nm, (g) 67.1

nm, (h) 80.3 nm (i) 90.6 nm, and (j) 103.5 nm . All powders exhibit the typical pattern for hexagonal zincite ( ).

5.1.1.2 Nitrogen Adsorption

Specific surface area, pore volume, and average pore size of ZnO with various crystallite sizes were determined from nitrogen adsorption isotherms and are displayed in Table 5.1.

Table 5.1 BET surface area, pore size, and pore volume of the FSP-made ZnO with various crystallite sizes.

| Sample	Surface Area (m²/g)	Pore Volume (cm³/g)	Pore Size (nm)
ZnO 8.8 nm	63.1	0.26	13.3
ZnO 19.4 nm	35.5	0.07	7.1
ZnO 30.0 nm	26.2	0.06	7.3
ZnO 40.0 nm	13.6	0.02	7.9
ZnO 47.0 nm	15.1	0.03	6.3
ZnO 52.6 nm	12.0	0.02	5.4
ZnO 67.1 nm	8.0	0.01	8.7
ZnO 80.3 nm	6.8	0.01	8.6
ZnO 90.6 nm	5.9	0.01	7.6
ZnO 103.5 nm	5.8	0.01	7.3

Table 5.1 summarizes BET surface area (SSA), average pore size, pore volume, and crystallite size (d_{XRD}) of all the ZnO powders. The d_{XRD} of ZnO increased from 9 to 47 nm corresponding to the decreasing on BET surface area from 63.1 to 15.1 m^2/g as the precursor concentration increased from 0.3 to 1 M and the feed rate increased from 3 to 8 ml/min. This result is consistent with previous study by Pratsinis et al. for FSP production of TiO_2 (Pratsinis *et al*.,1996), SiO_2 (Briesen *et al*.,2004), CeO_2(Mädler *et al*.,2002), Pt/Al_2O_3 (Hannemann *et al*.,2004), and Ag/ZnO (Height *et al*.,2006). Generally, increasing of precursor feed flow rate and/or precursor concentration while keeping the oxygen flow rate constant results in longer residence times and hotter flames (Tani *et al*.,2002 and Pratsinis *et al*.,1996). This phenomena is due to the fact that the combustion of the precursor is an exothermic reaction,

contributing to the overall increase in energy dissipation within the flame. Additionally, as the precursor feed flow rate and precursor concentration increases, the Zn and the particle concentration within the flame also increases. This, coupled with the mentioned increased residence time and higher flame temperature, resulted in increased coalescence and sintering of the particles. After annealing, the d_{XRD} of ZnO also increased from 47 to 103 nm and BET surface area decreased from 12.0 to 5.8 m^2/g as the annealing temperature increased from 750 to 900°C, which due to sintering of the ZnO particles by heat treatment. From this table, pore volume of the FSP made ZnO powders rapidly decreased from 0.26 to 0.03 when crystallite size of ZnO increased but in case of annealed-FSP ZnO pore volume remained unchanged when crystallite size of ZnO increased. Average pore size of the ZnO powders show ranged between 5.4-13.2 nm without any obvious trend as the crystallite size increased from 8.8-103.5 nm.

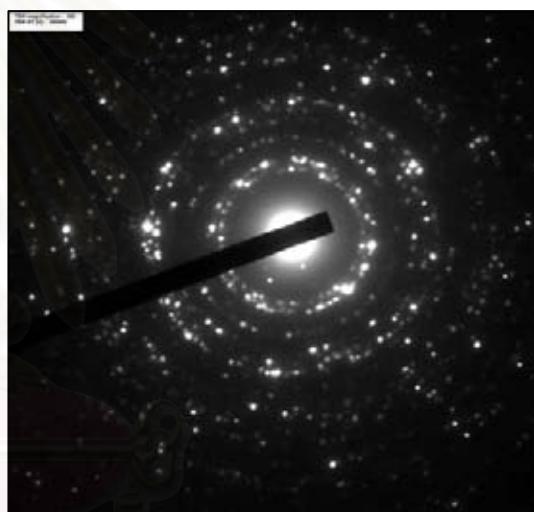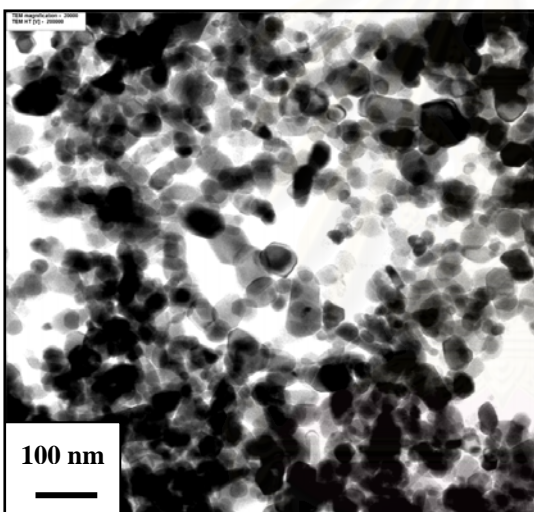### 5.1.1.3 Transmission Electron Microscopy (TEM)

TEM is a useful tool for determining particle morphology and average particle size of supported metals. TEM micrographs of ZnO with various crystallite sizes are shown in Figure 5.2.
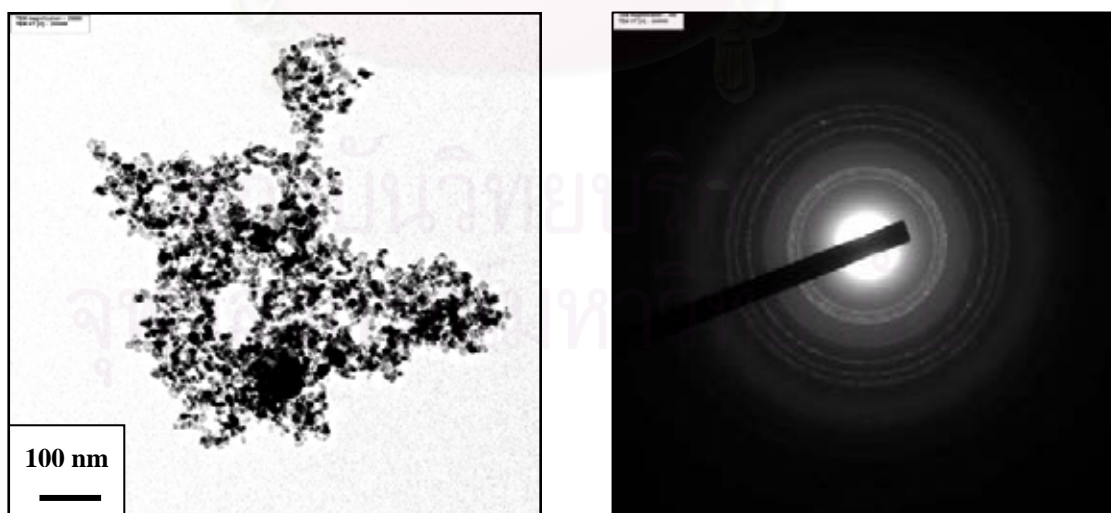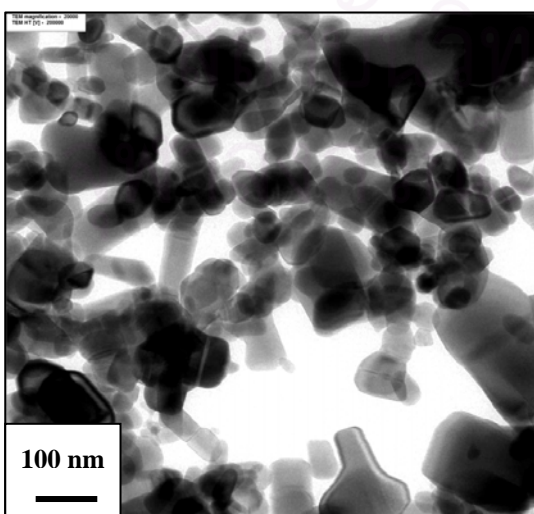

(a) ZnO 8.8 nm
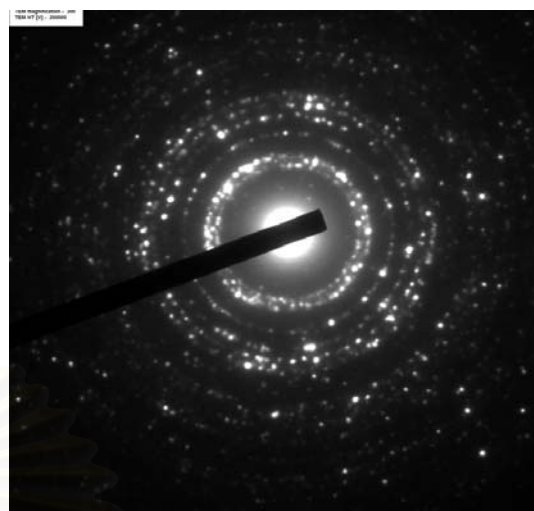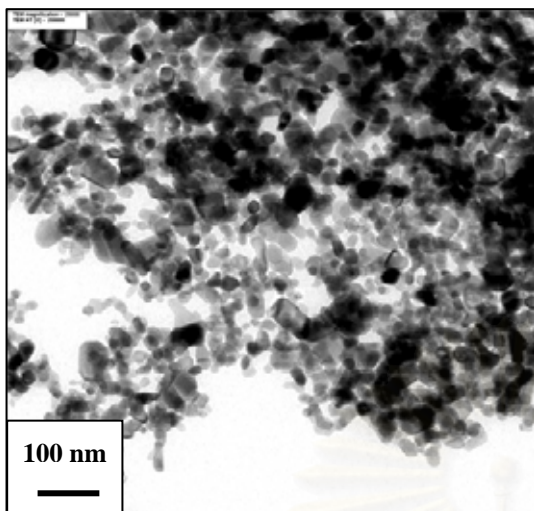
(b) ZnO 19.4 nm

(c) ZnO 30.0 nm

(d) ZnO 40.0 nm

(e) ZnO 47.0 nm

(c) ZnO 52.6 nm

(d) ZnO 67.1 nm

(e) ZnO 80.3 nm
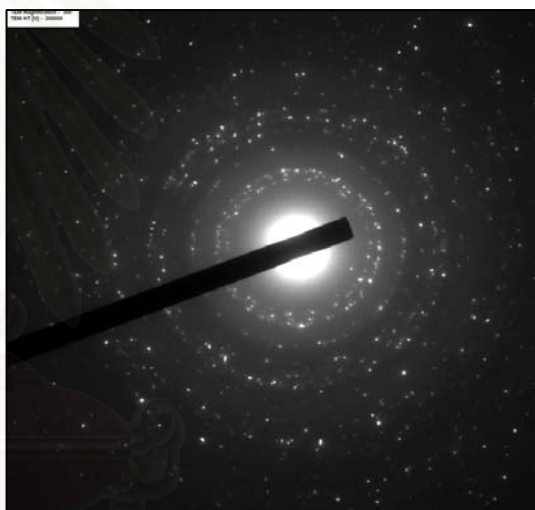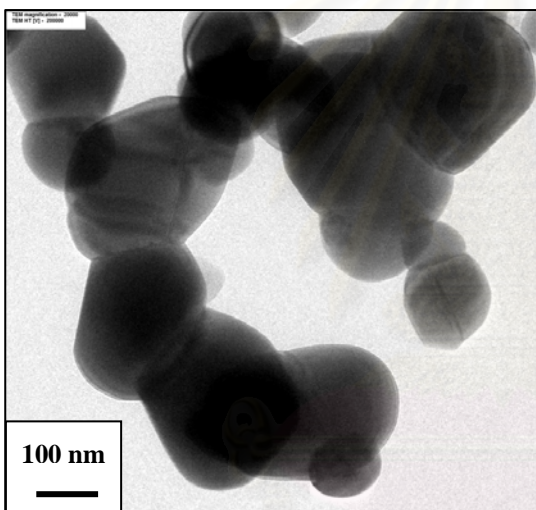
(i) ZnO 90.6 nm
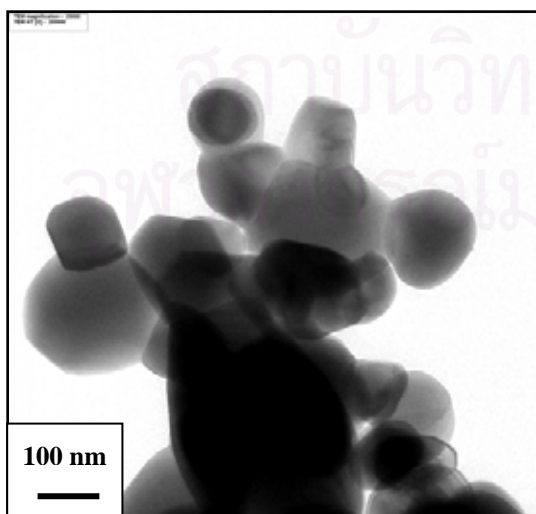
(j) ZnO 103.5 nm

Figure 5.2   TEM images and SAED of FSP made ZnO 8.8 nm (a), ZnO 19.4 nm (b), ZnO 30.0 nm (c), ZnO 40.0 nm (d) and ZnO 47.0 nm (e) powders and annealed-FSP made ZnO 52.6 nm (f), ZnO 67.1 nm (g), ZnO 80.3 nm (h), ZnO 90.6 nm (i), and ZnO 103.5 nm (j) powders.
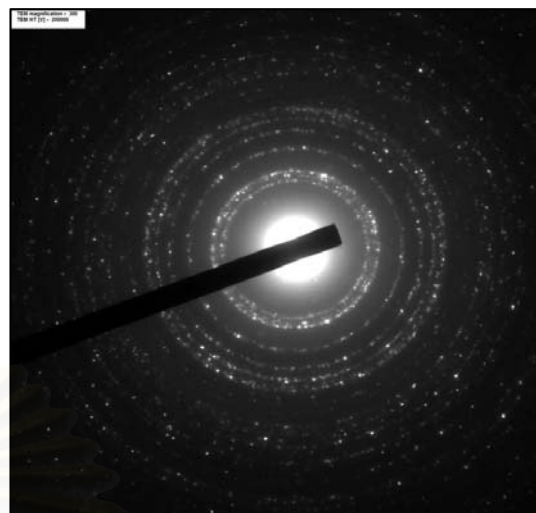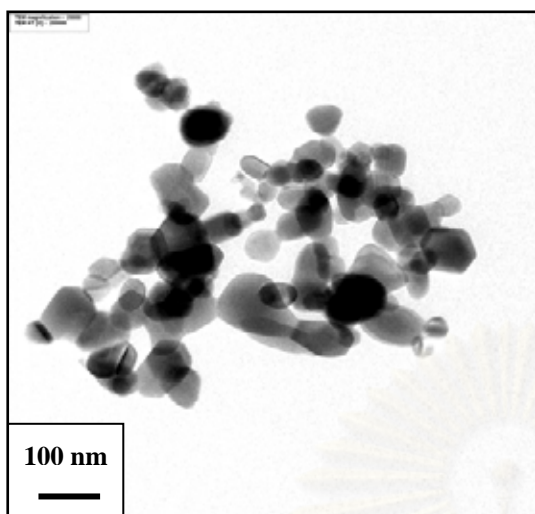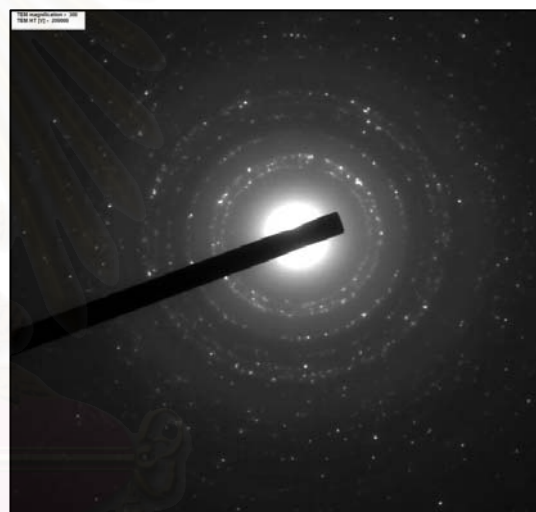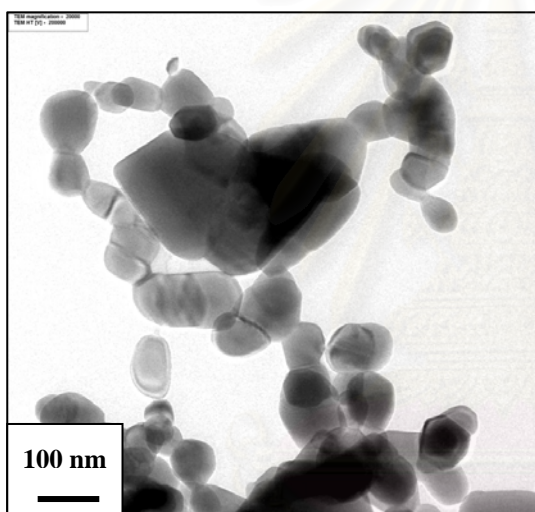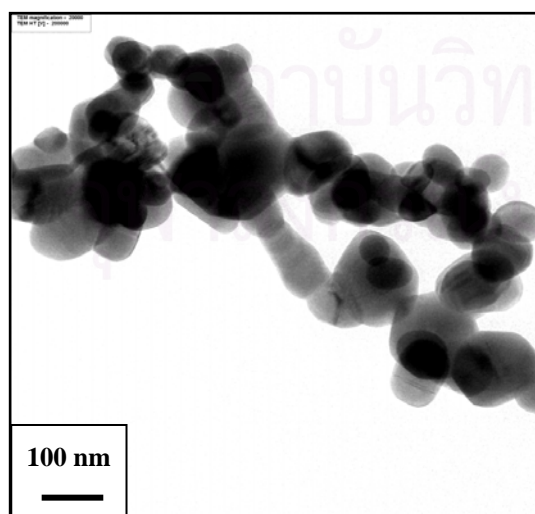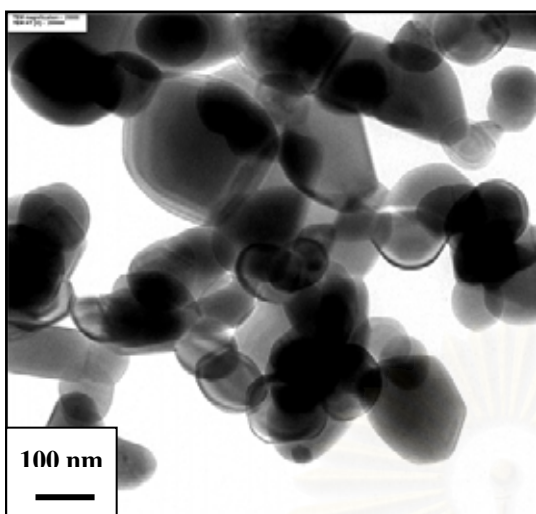
It can be noticed that FSP-made (a) ZnO 8.8 nm, (b) ZnO 19.4 nm (c) ZnO 30.0 nm, (d) ZnO 40.0 nm, and (e) ZnO 47.0 nm and annealed-FSP made (f) ZnO 52.6 nm (g) ZnO 67.1 nm, (h) ZnO 80.3 nm, (i) ZnO 90.6 nm, and (j) ZnO 103.5 nm consists of polyhedral primary shape, typically seen in flame-made powders (Pratsinis *et al*.,1998), with spheroidal particles and rod-like particles. The average primary particle diameters (d_{TEM}) of ZnO with various crystallite sizes were obtained by counting 50 particles and are summarized in Table 5.2. The d_{TEM} data is in good agreement with the d_{XRD} values indicating that the particles are single crystalline. The corresponding selected-area electron diffraction (SAED) patterns of all the ZnO powders illustrate spot patterns of the hexagonal structure of ZnO, indicating that ZnO nanoparticles consisted of single crystal.

Table 5.2 The average particle size (d_{TEM}) of ZnO with various crystallite sizes.

Sample	Average primary particle d_{TEM} (nm)
ZnO 8.8 nm	11.1
ZnO 19.4 nm	20.5
ZnO 30.0 nm	31.3
ZnO 40.0 nm	39.8
ZnO 47.0 nm	48.7
ZnO 52.6 nm	57.7
ZnO 67.1 nm	71.7
ZnO 80.3 nm	98.9
ZnO 90.6 nm	116.7
ZnO 103.5 nm	159.9

5.1.1.3 Photoluminescence (PL)

The PL emission spectra are useful to disclose the efficiency of charge carrier trapping, immigration, and transfer, and to understand the fate of electron–hole pairs in semiconductor particles since PL emission results from the recombination of free

carriers. Room temperature PL spectra of all the ZnO powders are shown in Figure 5.3.
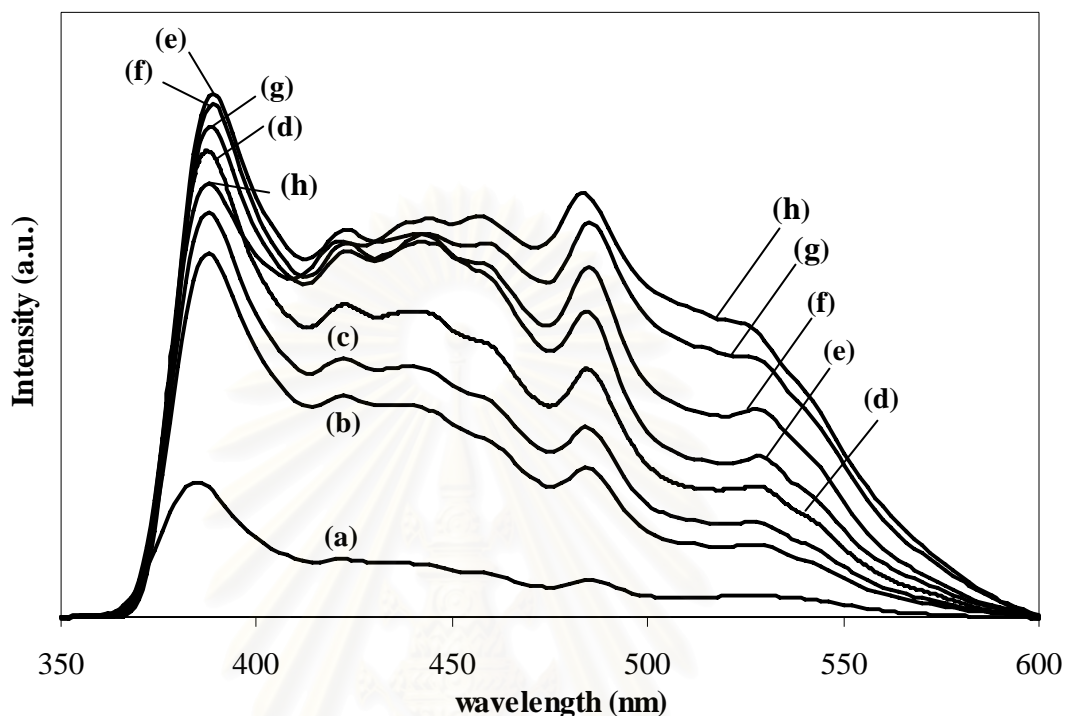
**Figure 5.3** PL spectra of ZnO various crystallite sizes (a) ZnO 8.8 nm, (b) ZnO 19.4 nm, (c) ZnO 30.0 nm, (d) ZnO 40.0 nm, (e) ZnO 47.0 nm (f) ZnO 67.1 nm, (g) ZnO 80.3 nm, and (h) ZnO 103.5 nm with the excitation wavelength of 325 nm.

The spectrum of the ZnO powders mainly consists of two emission bands. The first band is the UV near-band-edge emission (NBE) at ~385 nm (Marı´ *et al*.,2006 and Lim *et al*.,2004). Sharp NBE emission peak results from recombination of excitons and its position and structure is an indication of crystal quality. NBE emission intensities in the PL spectra increased as the crystallite size of ZnO increased and reached the highest value for FSP-made ZnO with the crystallize size of 47 nm. Improvement of crystal quality of ZnO would be attributed to the increasing of the flame enthalpy and Zn atomic concentration in gas phase that contributes typically to longer and hotter flames, which produce larger and more crystalline particles. However, after further annealing the excitonic peak intensity was slightly decreased as the treating temperature increased. This would be due to the occurrence of sintering phenomenon. The other band is the visible emission that usually associates with the

deep level emission (DLE) in ZnO. Most researchers believe that the DLE come from oxygen vacancies (V_O), zinc vacancies (Zn_O), interstitial zinc (Zn_i), or interstitial oxygen (O_i) (Leiter *et al*.,2003 and Li *et al*.,2006). The blue emission at ~ 425 nm and weak blue at ~ 445 nm most likely occurs from the donor level of Zn interstitial (Zn_i) to acceptor energy level of Zn vacancy (Zn_O) (Wei *et al*.,2007). The blue–green band around 470 nm by radiative transition of electron from shallow donor levels, created by the oxygen vacancy to valence band (Chu *et al*.,2007). The green emission at ~ 530 is commonly observed for ZnO, and is attributed to the singly ionized oxygen vacancy in ZnO (Vanheusden *et al*.,1996). This emission results from the recombination of a photo-generated hole with the singly ionized charge state of the specific defect (Wang *et al*.,2004). The peak intensity of the blue and weak blue peak light emission increased with the increasing of crystallize size from 8.8 to 47.0 nm and then was found remained unchanged. While, the weak blue–green band and green band emission peaks intensity increased with increasing crystallize size from 8.8 nm to 103.5 nm. When ZnO powders were heated at higher temperature, a reduction in the oxygen content with an increase in oxygen vacancy related defects may be expected with associated increase in the intensity of weak blue–green and green band emission.

5.1.1.4 Electron Spin Resonance Spectrometry (ESR)

The electron spin resonance spectrometry (ESR) is an effective method for investigating the electron spin state and the structure of the surface of nanosized crystallites. The ESR intensity per surface area of ZnO with various crystallite sizes are shown in Figure 5.4.

The FSP-made ZnO powders showed a strong and stable ESR signal with a *g* factor of 2.01 at room temperature (Liqiang *et al*.,2004, Yu *et al*.,1998). The ESR signal resulted from the O_2^- deficiencies on the FSP-made ZnO surface which can capture and restrict the electrons so that the paramagnetic resonance sources with $S = 1/2$ were produced, exhibiting the stable ESR signal. The amount of surface O_2^- deficiencies are given in the Table 5.3. From this table, it is demonstrated that the

ESR intensity per surface of the FSP-made ZnO rapidly increased as the crystallite size increased except the ZnO 52.6 nm and ZnO 67.1 nm, which the intensity of surface O_2^- deficiencies decreased from ZnO 47 nm. Therefore, the action essences of the oxygen vacancies on the surface of ZnO nanoparticles could easily capture and bind electrons. Moreover, there might be a strong interaction between the captured electrons and adsorbed oxygens, which favored the PL and photocatalytic oxidation reaction.
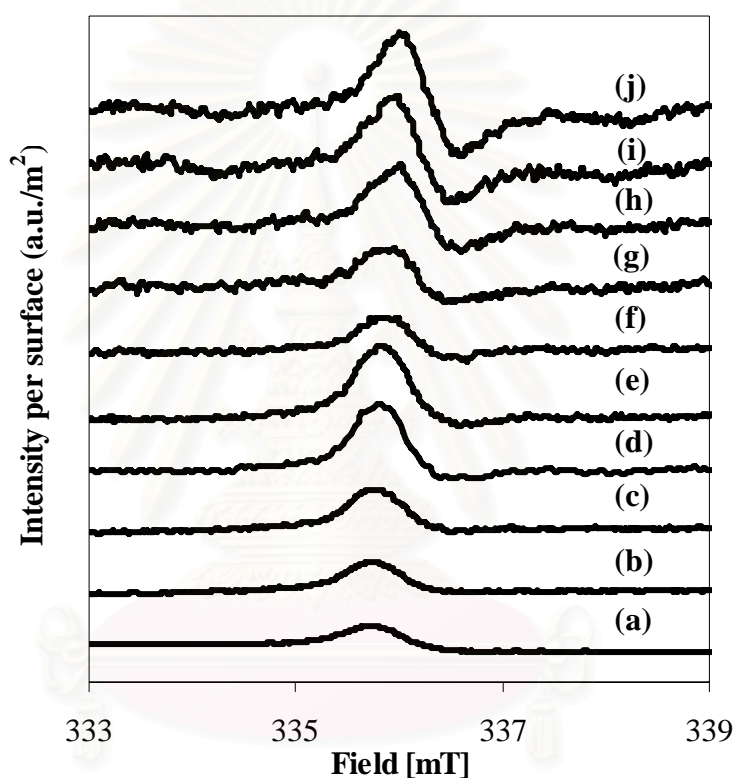
Figure 5.4 ESR spectrum of FSP made ZnO 8.8 nm (a), ZnO 19.4 nm (b), ZnO 30.0 nm (c), ZnO 40.0 nm (d) and ZnO 47.0 nm (e) powders and annealed-FSP made ZnO 52.6 nm (f), ZnO 67.1 nm (g), ZnO 80.3 nm (h), ZnO 90.6 nm (i), and ZnO 103.5 nm (j) powders.

Table 5.3 Intensity of O_2^- ion vacancies per surface area of ZnO various crystallite sizes.

Samples	BET surface Area (m²/g)	Weight (g)	Intensity of O_2^- ion vacancies per surface area
ZnO 8.8 nm	63.1	0.048	245
ZnO 19.4 nm	35.5	0.071	289
ZnO 30.0 nm	26.2	0.064	404
ZnO 40.0 nm	13.6	0.077	709
ZnO 47.0 nm	15.1	0.063	768
ZnO 52.6 nm	12.0	0.064	416
ZnO 67.1 nm	8.0	0.065	581
ZnO 80.3 nm	6.8	0.065	836
ZnO 90.6 nm	5.9	0.064	1009
ZnO 103.5 nm	5.8	0.070	1172

5.1.2 Photocatalytic testing
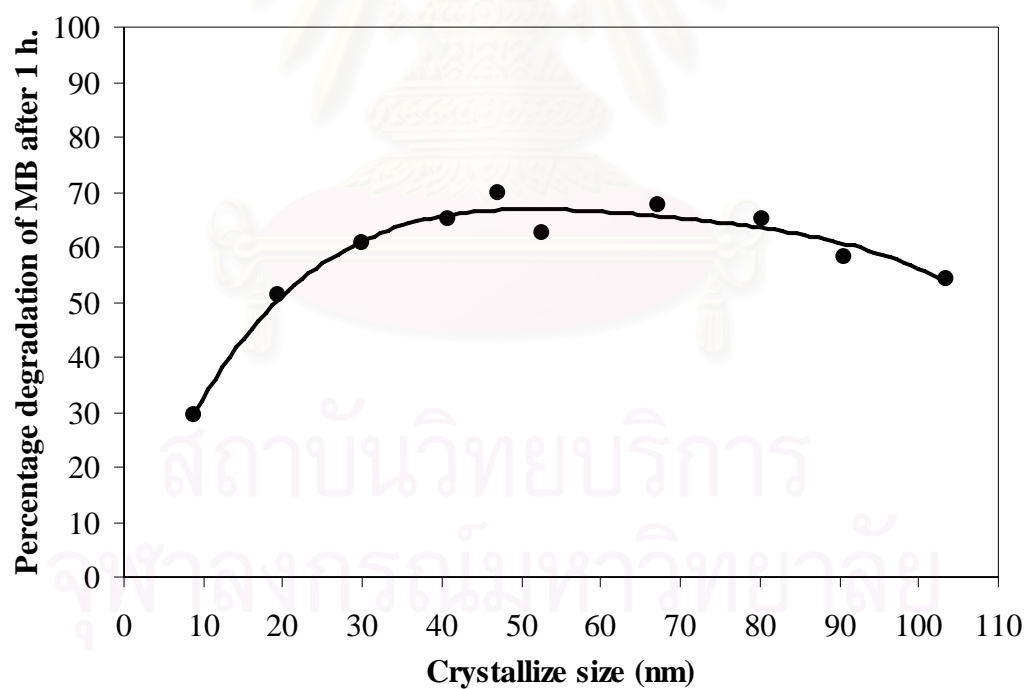
Figure 5.5 Relation between for the percentage of degradation of MB after 1 h. and crystallite sizes of ZnO catalyst prepared by FSP method.

Figure 5.5 shows the dependence of percent conversion of MB decomposition after 60 min versus the crystallite sizes of ZnO powders. The trend line of percentage degradation increased from 30 to 70 percent when the crystallite size of ZnO powders increased from 8.8 to 47 nm. The reason for this would be related to the improvement of crystallinity of ZnO, surface oxygen vacancies and defects of ZnO nanoparticles in the flame during synthesis. When particle size becomes extremely small, surface recombination becomes an important process. Most of the e^-/h^+ pairs are generated sufficiently close to the surface. They may quickly reach the surface, and undergo rapid surface recombination mainly due to abundant surface trapping sites and the lack of driving force for e^-/h^+ pair separation (Zhang et al.,1998 and Serpone *et al*.,1998). As we can see in Figure 5.3**,** ZnO with the crystallite size of 47 nm had highest crystallinity, surface oxygen vacancies contents and defects, which possibly gave the highest photocatalytic activity because surface oxygen vacancies and defects can become centers to capture photo-induced electrons to form excitons in the sub-band, so that the recombination of photo-induced electrons and holes can be effectively inhibited. Moreover, oxygen vacancies can promote O_2 adsorbing, and there is a strong interaction between the photo-induced electrons bound by oxygen vacancies and the adsorbed O_2. This indicates that oxygen vacancies favor the adsorbed O_2 to capture photo-induced electrons, simultaneously producing $^\bullet O_2$ radical groups. The radical groups are active to promote the oxidation of organic substances (Liqiang *et al*.,2006). However, when the particle size of ZnO powders increased from 47 to 103.5 nm the trend line of percentage degradation gradually decreased from 70 to 55 percent. The lower photocatalytic efficiency may be attributed to two reasons: (1) lower crystalline quality as shown by the PL signals that lower electrons were generated and resulted in lower photocatalytic efficiency (Park *et al*.,2007), (2) decreasing of surface area, which lowered the adsorption of dye molecules on the catalyst surface**.**

Figure 5.6 shows the kinetics of MB photodegradation in the presence of using ZnO with various crystallite sizes as the photocatalysts. Degussa P25 (d_{xrd} = 20.1 nm) and JRC titania (d_{xrd} = 15.5 nm) are included here as reference samples. The MB concentration keeping the initial value during 60 min irradiation in the absence of any

52

photocatalyst is also shown in this figure, revealing that the MB cannot be degraded
by 365-nm irradiation directly. The plot of $-\ln(C_t/C_0)$ versus time curves of the
methylene blue photodegradation using ZnO with various crystallite sizes as the
photocatalysts are shown in Figure 5.7. All the curves are linear, revealing that the
kinetic data of the methylene blue photodegradation fitted well to the first-order
reaction kinetic model. The apparent first-order reaction rate constants calculated
from the slopes of those curves are shown in Table 5.4. It demonstrates that when the
crystallite sizes of ZnO powders were larger than 30 nm, the catalytic activity for
methylene blue photodegradation was higher than both P25 and JRC titania. The first-
order kinetic constant of ZnO crystallite size 47 nm that showed the optimum of the
photocatalytic activity was about 1.7 times higher than that of degussa P25 and 7.2
times higher than of using JRC titania.
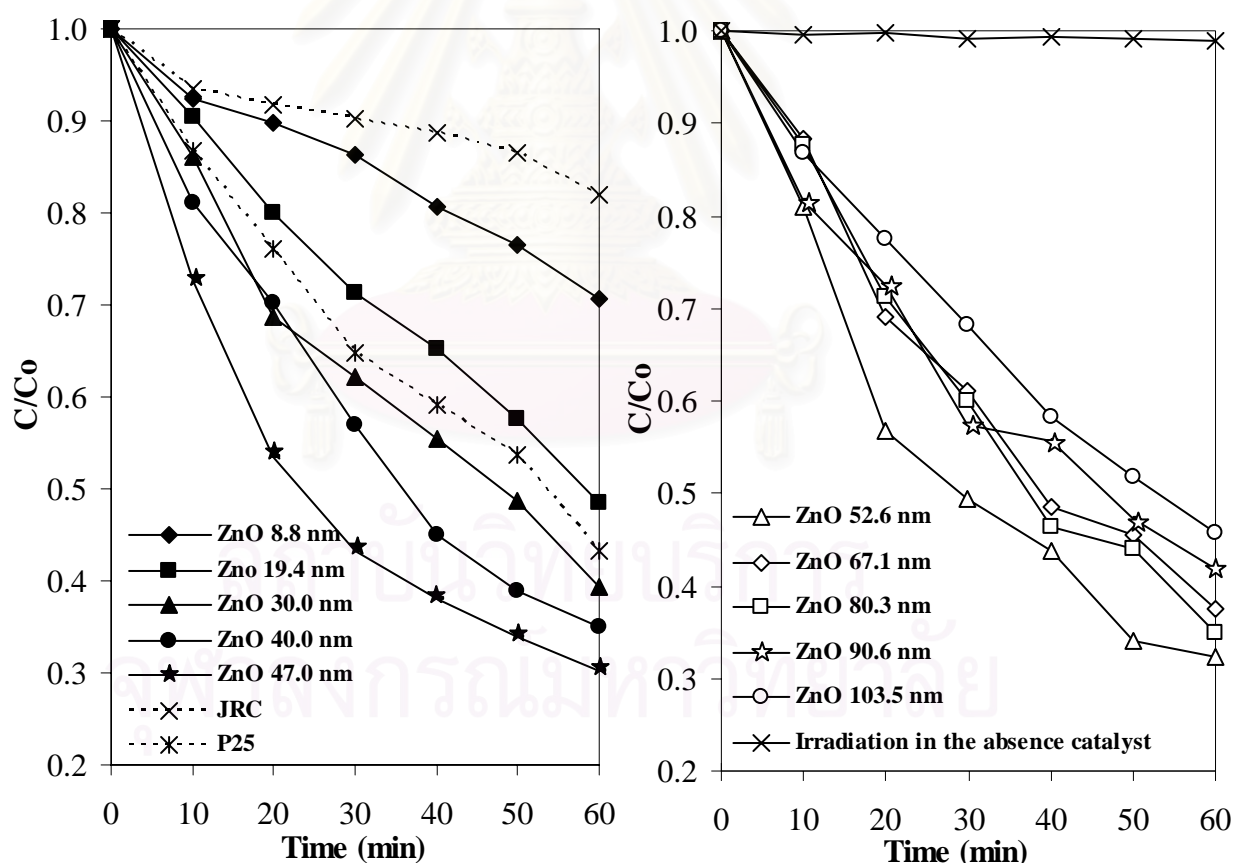
Figure 5.6 Photodegradation kinetics of MB using ZnO various crystallite size (a)
FSP made ZnO and (b) annealed-FSP ZnO (bold lines) and commercial catalysts for
comparison (P25 and JRC titania) (dashed lines).
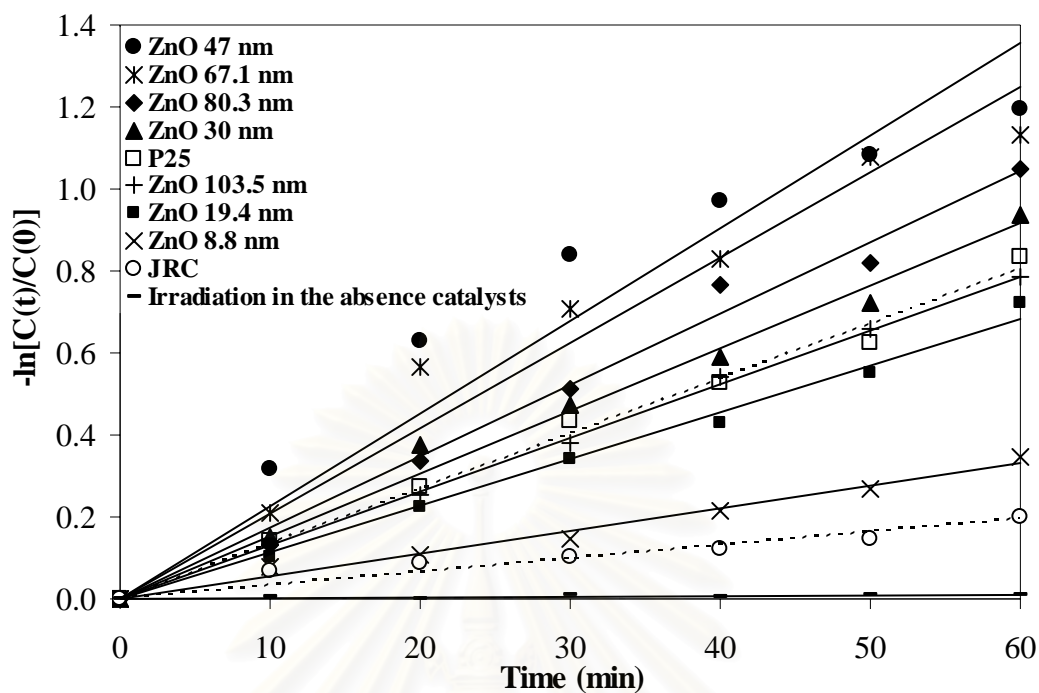
Figure 5.7 The first-order kinetics of MB photo-degradation in presence of FSP-made ZnO various crystallite sizes (bold lines) and commercial catalysts for comparison (P25 and JRC titania) (dashed lines).

Table 5.4 Reaction performance in photodegradation methylene blue of ZnO various crystallite sizes prepared via FSP method. P25 and JRC titania are also reported for comparison purpose.

Sample	MB conversion after 1 h. (%)	Rate constant (h^{-1})
ZnO 8.8 nm	29	0.33
ZnO 19.4 nm	51	0.68
ZnO 30.0 nm	61	0.92
ZnO 40.0 nm	65	1.11
ZnO 47.0 nm	69	1.36
ZnO 52.6 nm	63	1.00
ZnO 67.1 nm	68	1.25
ZnO 80.3 nm	65	1.04
ZnO 90.6 nm	58	0.91
ZnO 103.5 nm	54	0.79
TiO_2 (JRC)	18	0.19
TiO_2 (P25)	57	0.80

5.2 Photocatalytic degradation of methylene blue by Pt/ZnO and Au/ZnO catalysts prepared by the FSP method.

5.2.1 Particle characterization

5.2.1.1 X-ray Diffraction (XRD)

X-ray diffraction is used to investigate the changes of phase structure and crystallite size of the as-prepared ZnO powders before and after Pt and Au deposit.
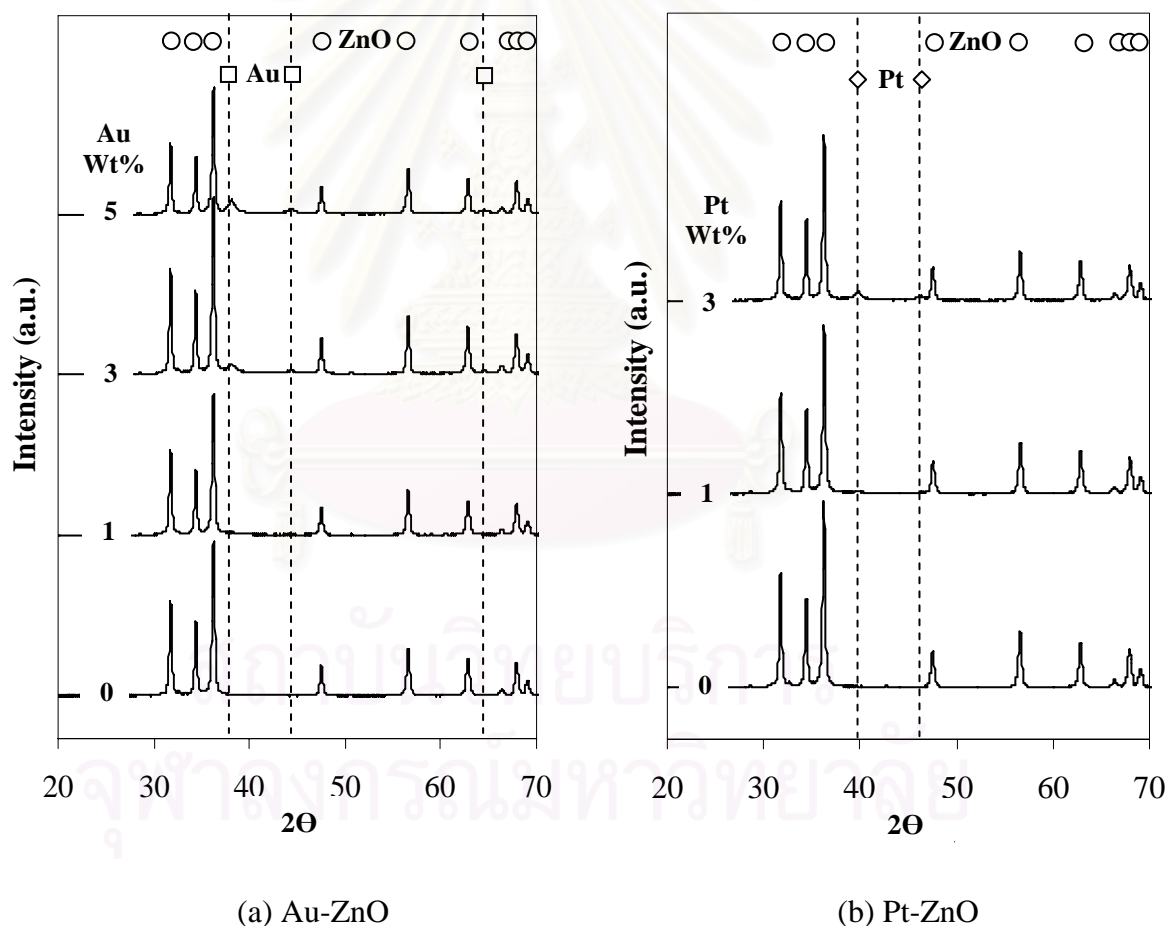
(a) Au-ZnO   (b) Pt-ZnO

Figure 5.8 XRD patterns of flame-made (a) Au/ZnO and Flame-made (b) Pt/ZnO powders. All powders exhibit the typical pattern for hexagonal zincite (○). (□) and (◇) represent the characteristic pattern of Au and Pt metal, respectively.

Figure 5.8a shows the XRD patterns of flame-made Au/ZnO powders. All the powders exhibited the typically pattern for hexagonal zincite (JCPDS Card File No. 36-1451). The crystallite size (d_{XRD}) of ZnO which calculated from the (101) diffraction peak of ZnO by using Scherrer equation did not change much after metal loading as shown in Table 5.5. When the Au content reached 3 wt %, the diffraction peaks corresponding to the (111), (200), and (220) planes of gold were observed at 38.0°, 44.3°, and 64.5°, respectively. The peak intensity increased with increasing Au loading. It should be noted that metal was obtained directly in the as-produced material without a need for a post-synthesis reduction step. These results suggest that, gold atoms were not incorporating into the ZnO lattice (or only to a very limited extent) but rather form on to the ZnO surface late in the flame after the ZnO has been formed. The XRD crystallite size (d_{XRD}) of Au calculated from the (111) diffraction peak of Au by using Scherrer equation was about 5.8 nm for Au 3 wt.% and 9.4 nm for Au 5 wt.%. Figure 5.8b similarly shows the XRD patterns of the flame-made Pt/ZnO powders. The XRD characteristic peaks associated with Pt metal patterns of the (111) and (200) planes are observed at 39.7° and 46.2°, respectively after loading of 3 wt.% Pt. No XRD peaks were corresponding to platinum oxide phases are observed in the flame-made Pt/ZnO powders. The XRD crystallite size (d_{XRD}) of Pt 3 wt.% calculated from the (111) diffraction peak of Pt by using Scherrer equation was about 5.8 nm

Table 5.5 The average crystallite sizes of pure ZnO, Pt/ZnO, and Au/ZnO catalysts synthesized by FSP method.

Sample	The XRD crystallite size (d_{XRD}) (nm)	
	ZnO	metal
ZnO	37.5	n.d.
Pt 1 wt.% - ZnO	34.6	n.d.
Pt 3 wt.% - ZnO	38.9	5.8
Au 1 wt.% - ZnO	37.3	n.d.
Au 3 wt.% - ZnO	38.9	5.8
Au 5 wt.% - ZnO	39.8	9.4

n.d. = not determined

5.2.1.1 Transmission Electron Microscopy (TEM) with Energy dispersive X-ray analysis (EDX)

Morphological characterization of the as-prepared ZnO powders before and after Pt and Au deposit was carried out using Transmission Electron Microscopy (TEM). The presence of Au and Pt was confirmed by Energy dispersive X-ray analyzer (EDX).

Figure 5.9a shows the TEM images of ZnO nanoparticles prepared by FSP method without metal addition. It consists of polyhedral primary particles with size around 25-50 nm. Figure 5.9b and c show the TEM images of FSP made 1 and 3 wt.% Pt/ZnO. The density of dark spot increased with increasing Pt content from 1 to 3 wt.% and the average diameter of Pt deposits were determined to be approximately 4.0 and 6.1 nm, respectively. Figure 5.9d, e, and f show TEM images of Au/ZnO prepared by FSP method. The spherical Au nanoparticles dispersed on the surface of ZnO particles were observed as dark spots having obvious contrast with the support. The average diameter of Au particles gradually increased with the increase of Au loading, e.g., ~ 4.1 nm for Au-ZnO 1 %wt., ~ 6.3 nm for Au-ZnO 3 %wt., and ~ 10.3 nm for 5 %wt Au/ZnO., together with an increase of the number of Au particles on the surface of ZnO. The corresponding selected-area electron diffraction (SAED) patterns are shown below the TEM images. The diffraction patterns of all images illustrate spotty rings patterns, indicating its highly crystalline ZnO wurtzite structure, which was in good agreement with the XRD data. EDX spectra acquired for the FSP-ZnO and the Pt-loaded and Au-loaded FSP-ZnO are also shown in these figures. Clear Au and Pt peaks were detected on the corresponding samples. The weak copper and carbon signals were originated from the TEM copper grids and the carbon adhesion film.

(a) ZnO

(b) Pt-ZnO 1 wt.%

(c) Pt-ZnO 3 wt. %

(d) Au-ZnO 1 wt.

(e) Au-ZnO 3 wt.%

(f) Au-ZnO 5 wt.%
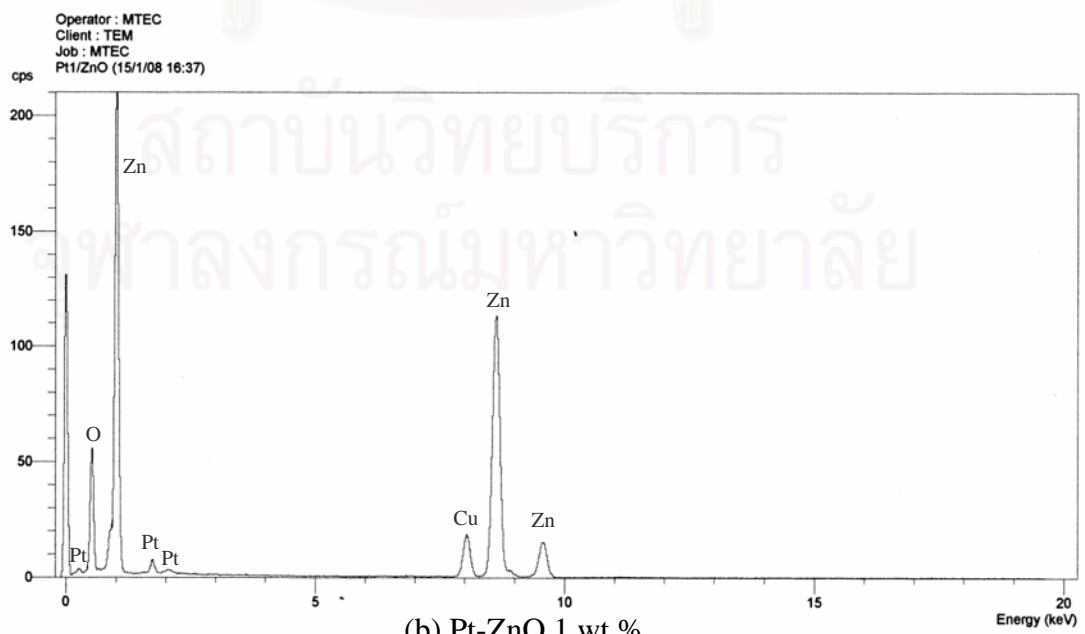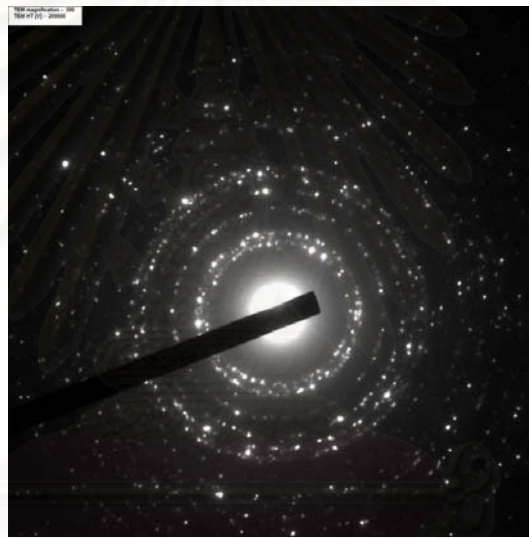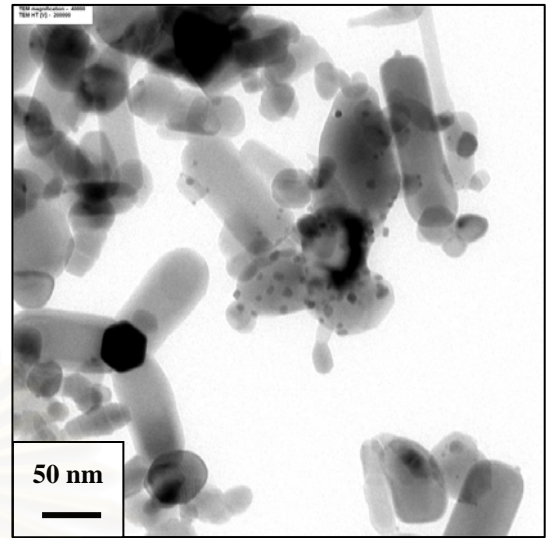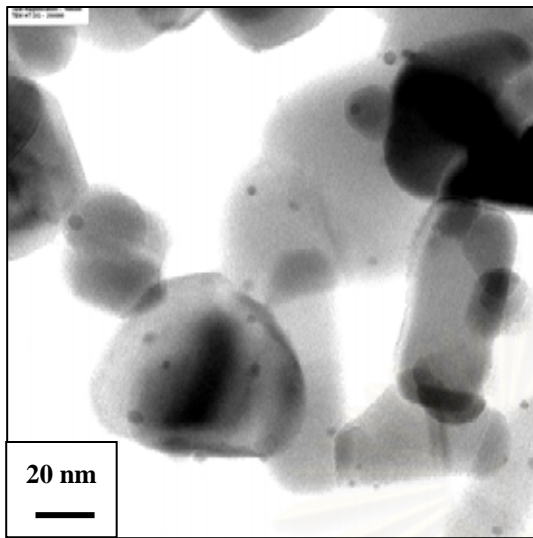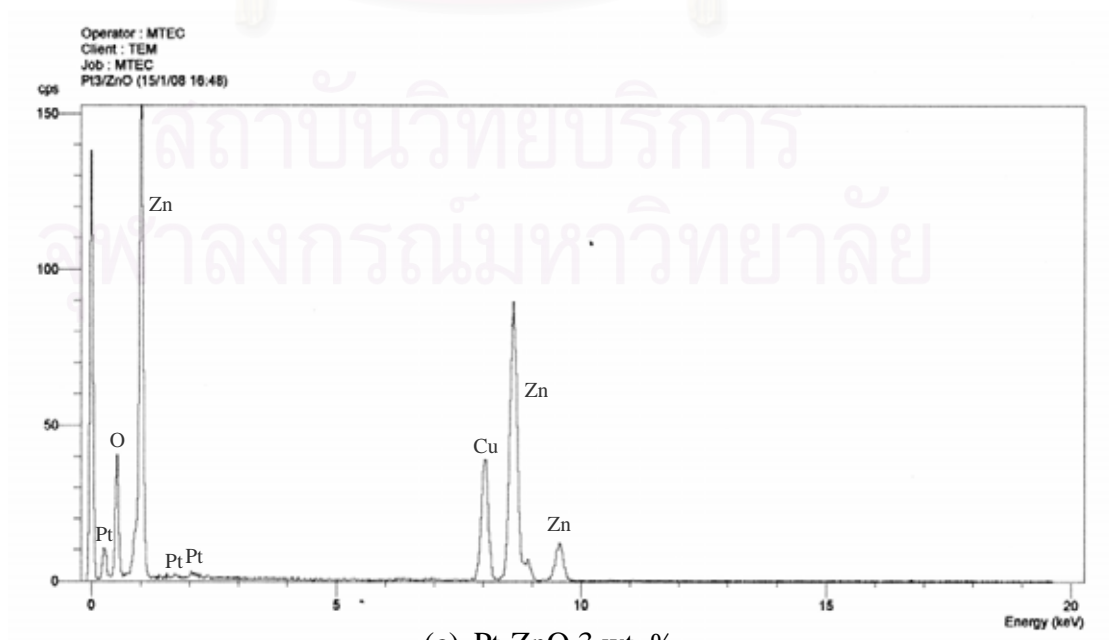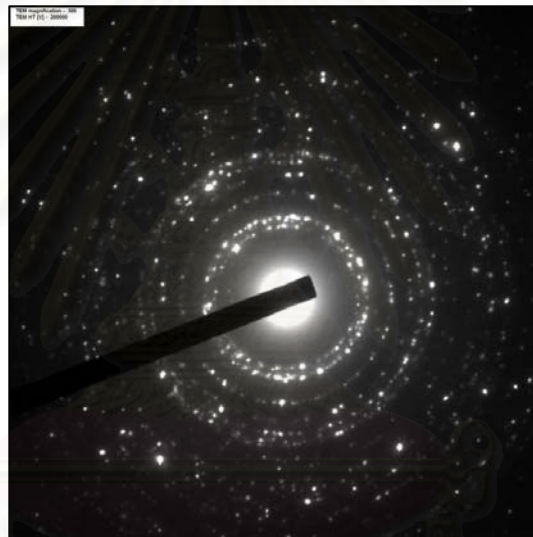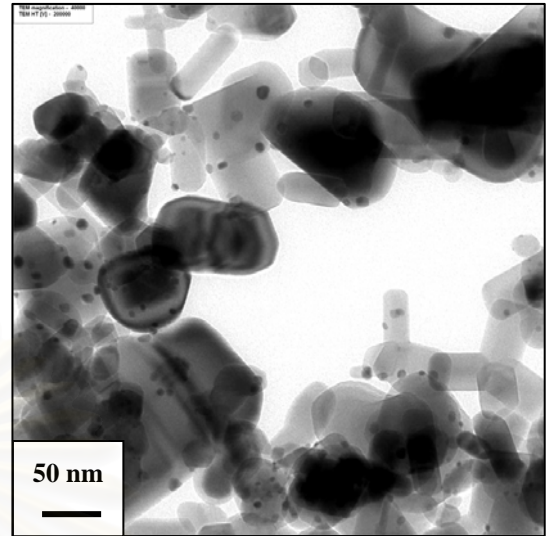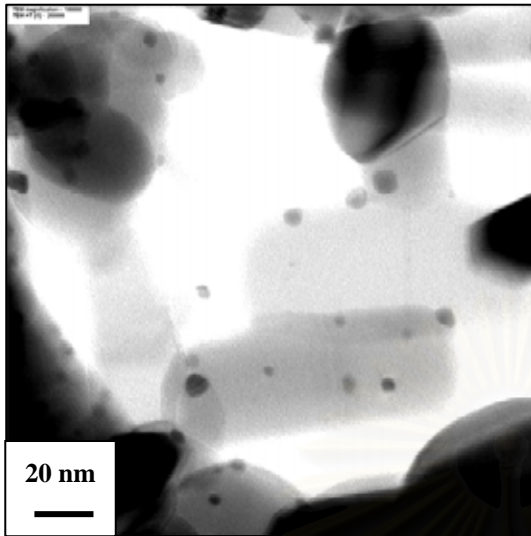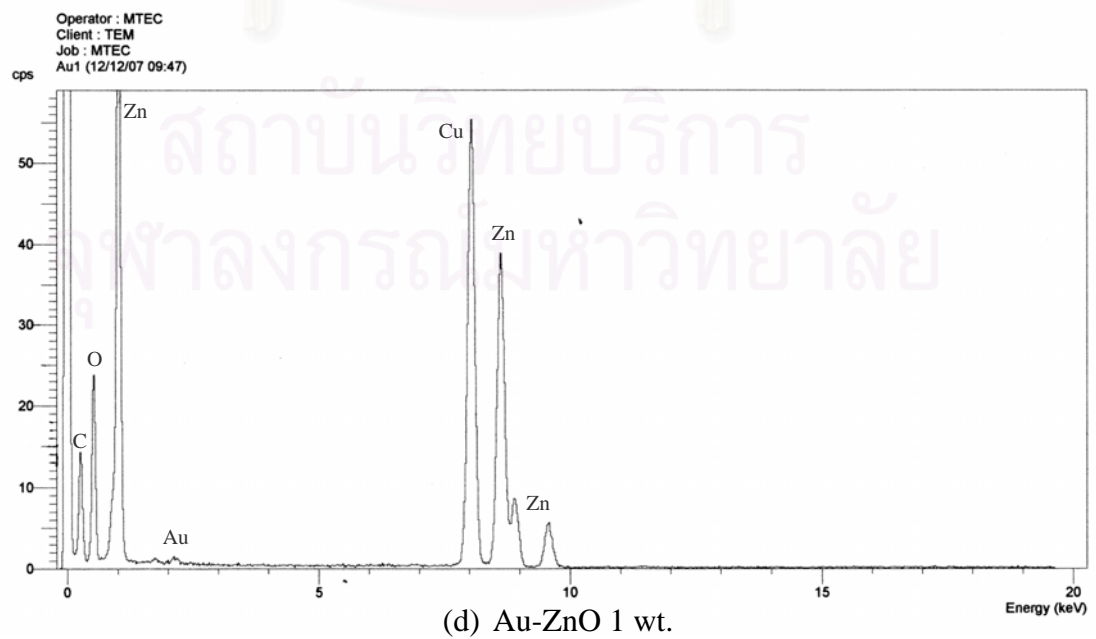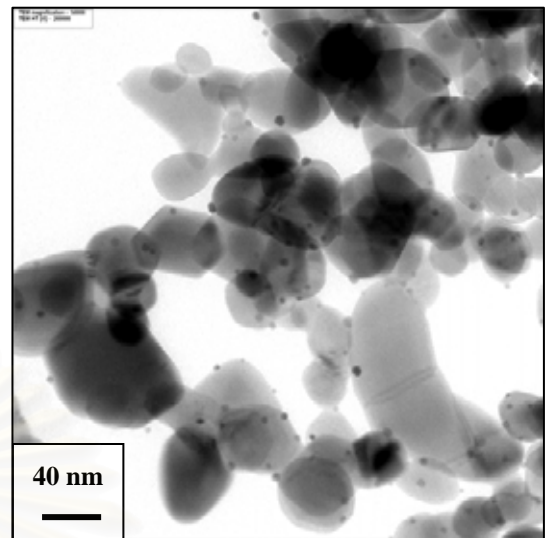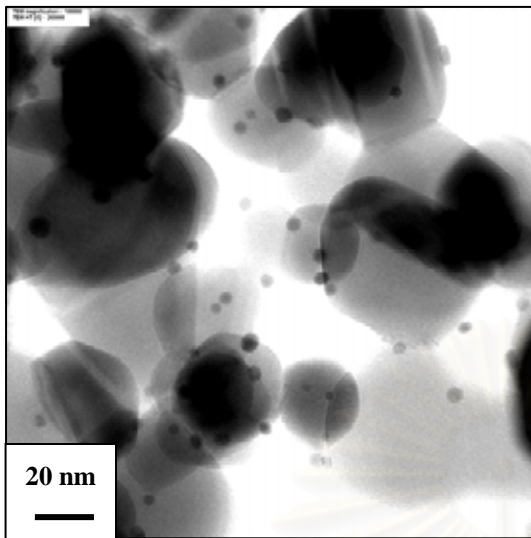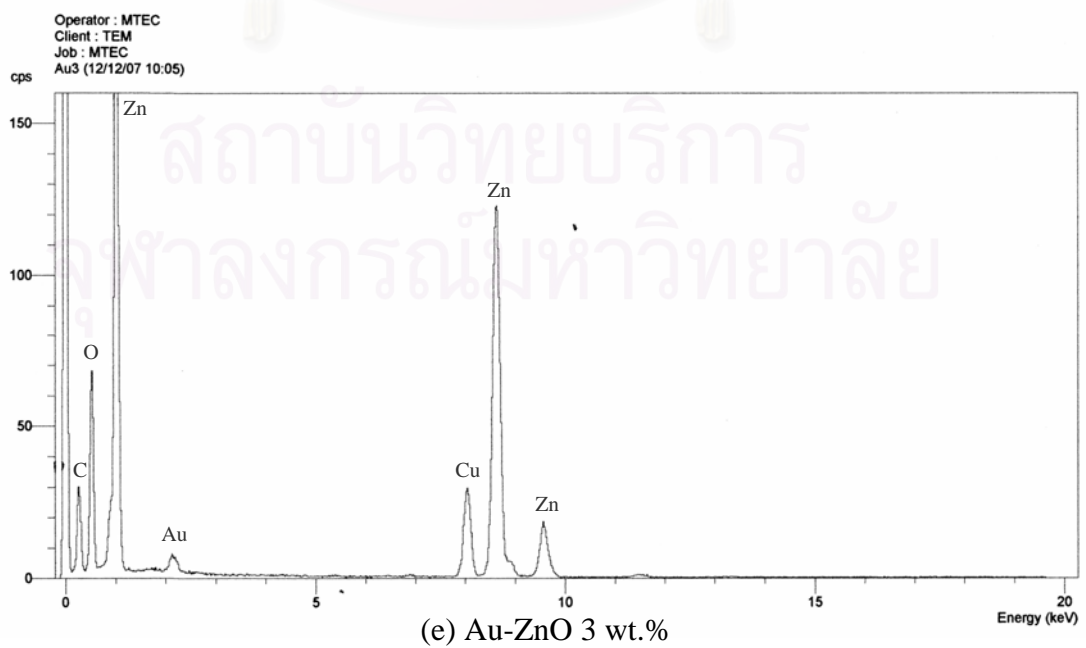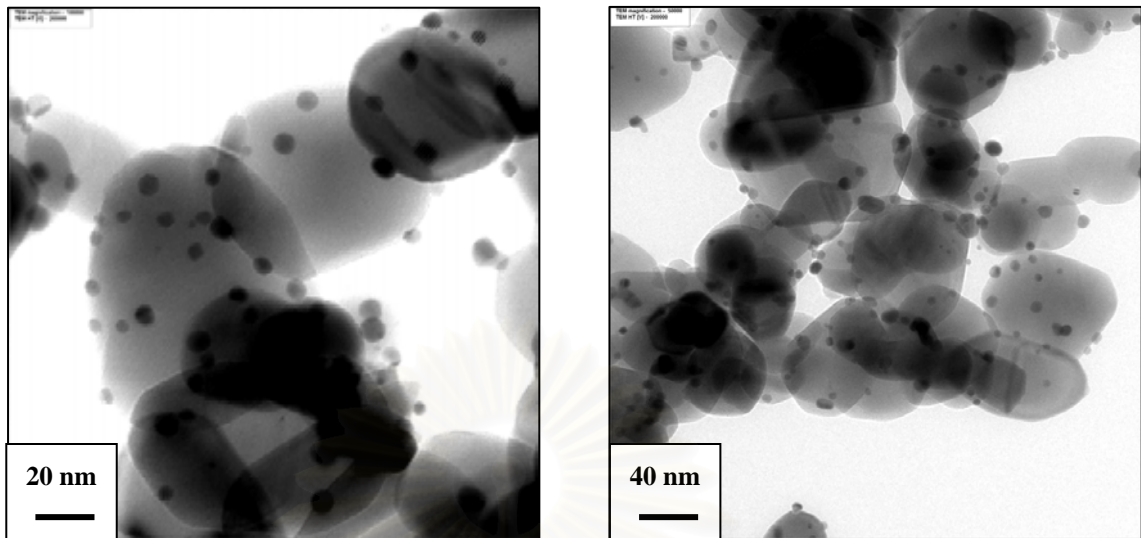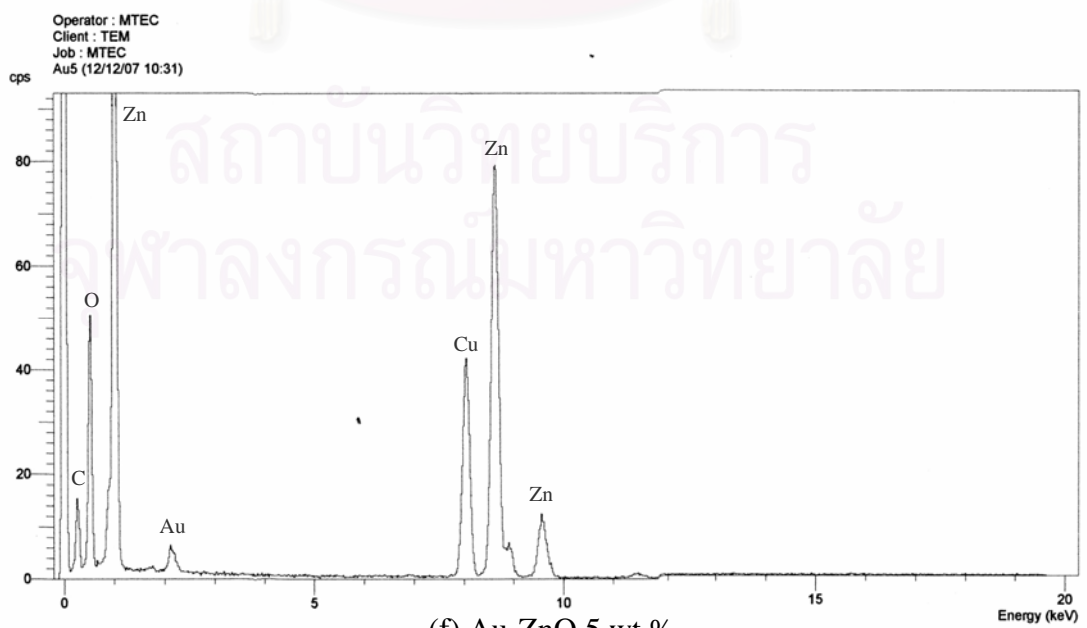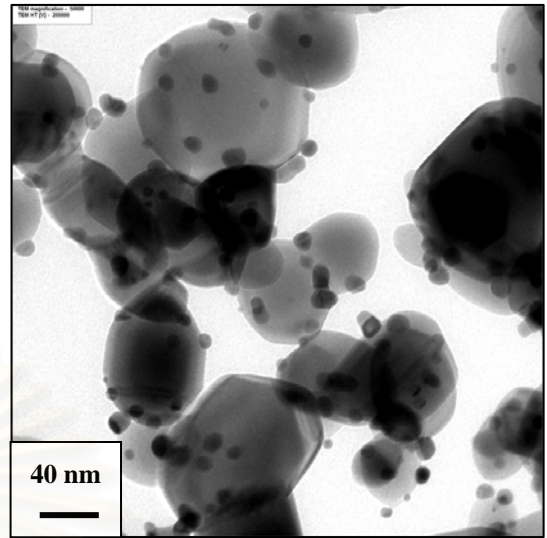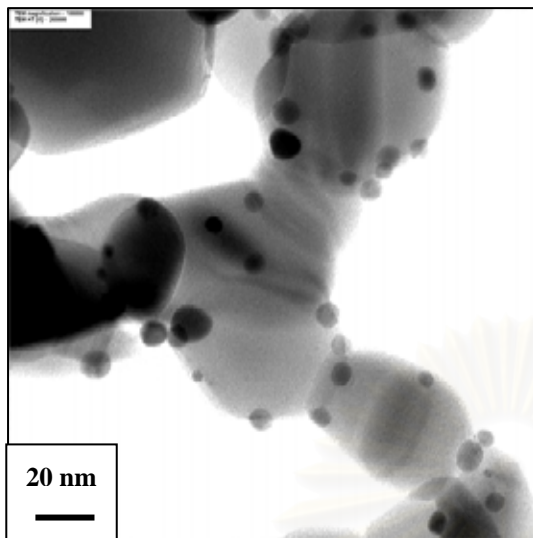
Figure 5.9 TEM images, SAED, and EDX spectrum of FSP-made pure ZnO (a), 1 wt.% Pt/ZnO (b), and 3 wt.% Pt/ZnO (c) 1 wt.% Au/ZnO (d), 3 wt.% Au/ZnO (e), and 5 wt.% Au/ZnO (f) powders. The darker spots on the TEM images (b and c) are Pt deposits and (d, e, and f) are Au deposits.

Table 5.6 The average particle size of pure ZnO, Pt/ZnO, and Au/ZnO catalysts synthesized by FSP method.

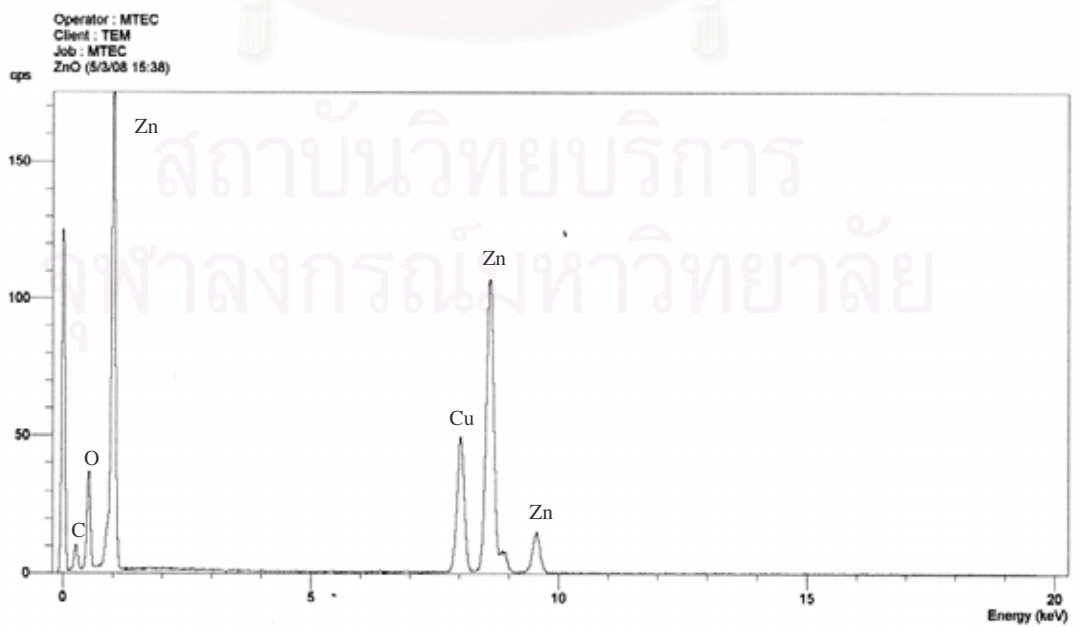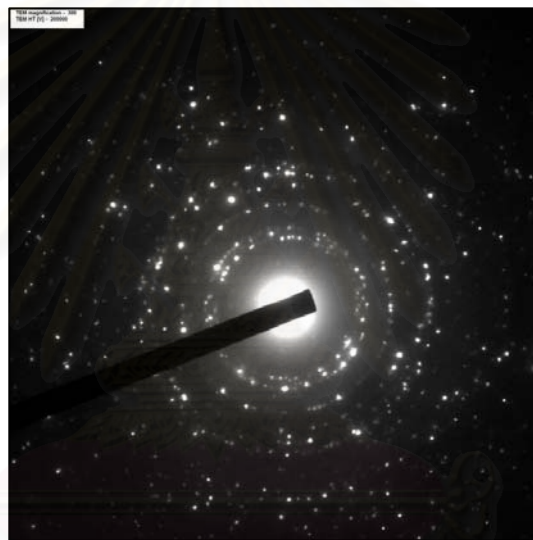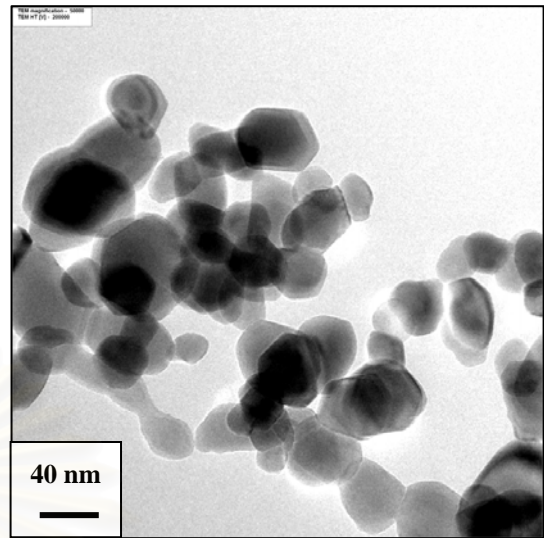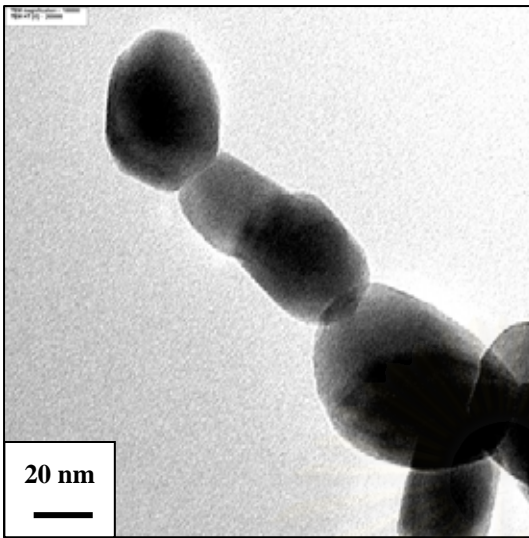| Sample	The average particle size d_{TEM} (nm)	
	ZnO	metal
ZnO	38.3	n.d.
Pt 1 wt.% - ZnO	35.0	4
Pt 3 wt.% - ZnO	36.5	6.1
Au 1 wt.% - ZnO	37.1	4.1
Au 3 wt.% - ZnO	38.9	6.3
Au 5 wt.% - ZnO	43.6	10.3

n.d. = not determined

5.2.1.1 Nitrogen Adsorption

Table 5.7 Bet surface area, pore size, and pore volume of ZnO, Pt/ZnO, and Au/ZnO catalysts synthesized by FSP method.

Sample	Surface Area (m²/g)	Pore Volume (cm³/g)	Pore Size (nm)
ZnO	18.6	0.03	6.6
Pt 1 wt.% - ZnO	23.9	0.04	6.1
Pt 3 wt.% - ZnO	19.1	0.03	5.8
Au 1 wt.% - ZnO	19.2	0.04	6.9
Au 3 wt.% - ZnO	16.1	0.03	6.8
Au 5 wt.% - ZnO	13.3	0.03	7.4

The SSA for Au/ZnO and Pt/ZnO ranged from 18.6 for pure ZnO to 13.3 and 19.1 m^2/g for 5 wt.% Au and 3 wt.% Pt loading, respectively. From this table, pore size and pore volume of these samples ranged from 58-74 Å and 0.03-0.04 cm³/g,

respectively. There were no significantly differences in the SSA, pore volume, and pore size of FSP made Au and Pt modified ZnO with various metal content.

5.2.1.1 UV-Visible Absorption Spectroscopy (UV-vis)

Figure 5.10a presents UV–vis spectra of the FSP made Au/ZnO powders. The absorption at visible wavelengths increased with increasing gold content, consistent with the visible powder color shift from white, to light purple, and dark purple, with increasing Au loading. The increase of absorption band at 400–900 nm with increasing Au content was due to the surface plasmon resonance of the Au nanoparticles indicating the presence of Au metal clusters which was in agreement with the XRD patterns. Figure 5.10b shows the UV–vis spectra for the FSP made Pt/ZnO powders. The absorption at visible wavelengths increased with increasing platinum content, consistent with the visible powder color shift from white, to light gray, and gray. The absorption at visible wavelengths of FSP made Pt/ZnO showed constant absorption while that of FSP made Au/ZnO showed variation absorption. In general, equal sized metal clusters are formed, it will lead to constant absorption in the visible region corresponding to the excitation from the valence band of ZnO to the unoccupied level of metal cluster (Sakthivel *et al*.,2004).
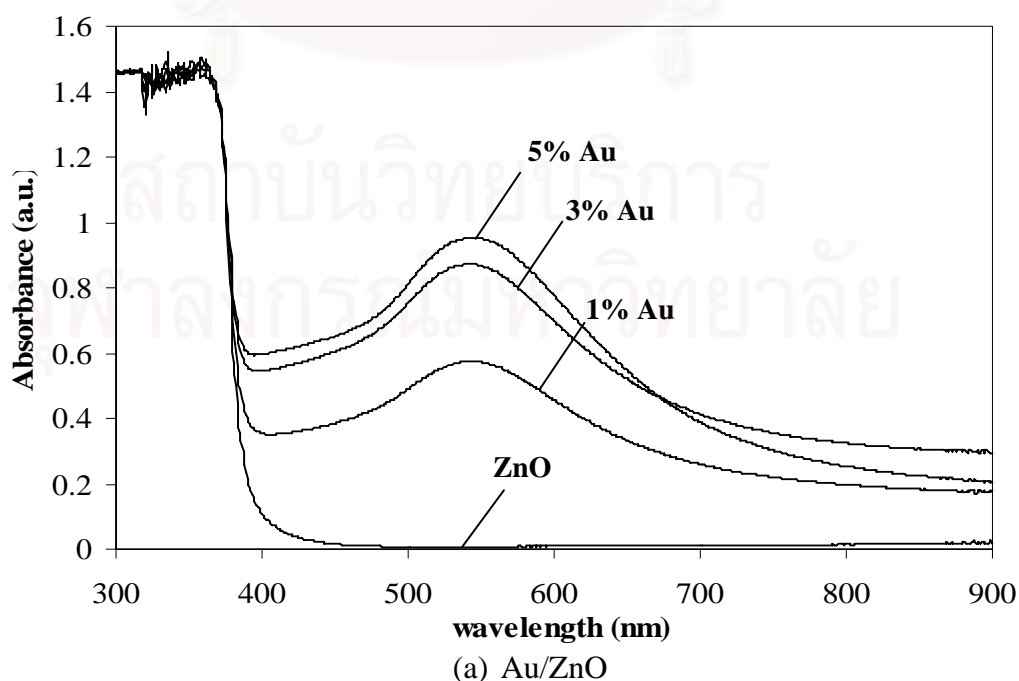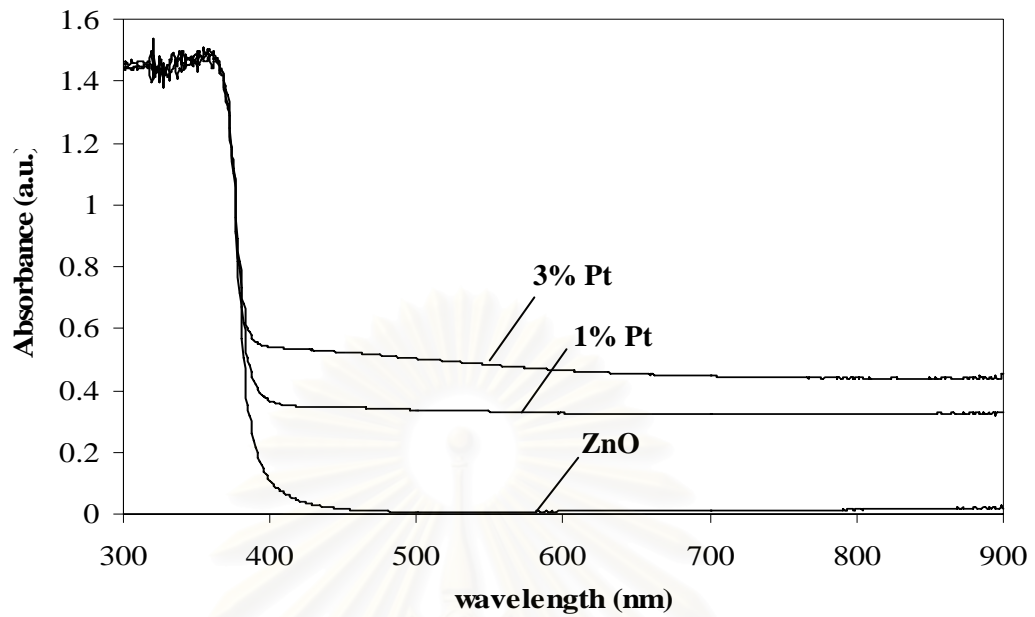
(a) Au/ZnO

(b) Pt/ZnO

Figure 5.10 UV–vis spectra of the FSP made Au/ZnO(a) and Flame-made Pt/ZnO.

5.2.1.1 Photoluminescence (PL)
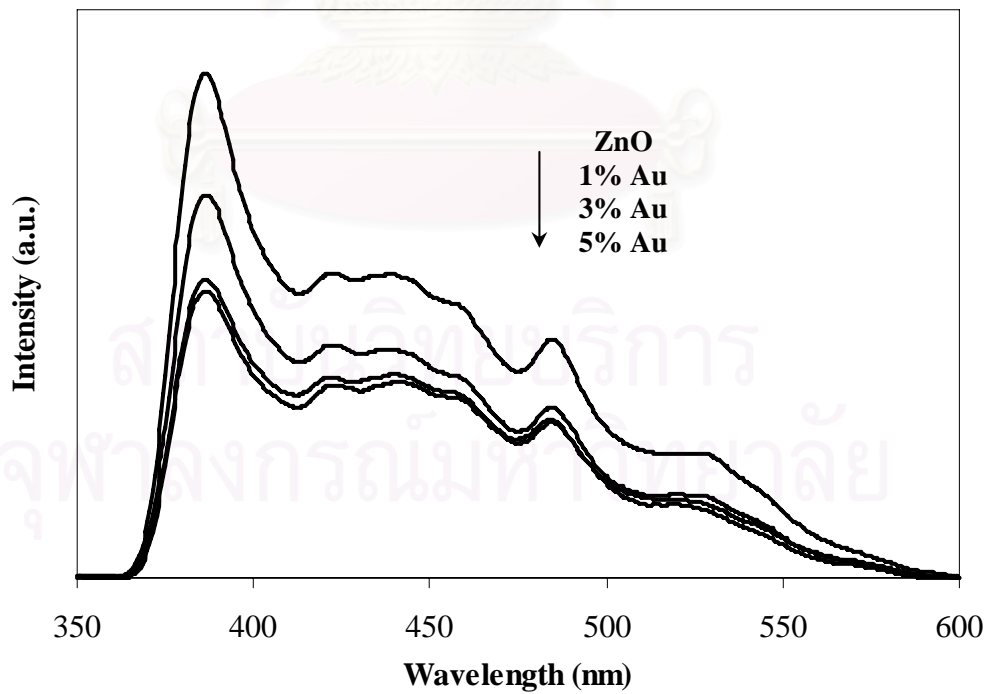
(a) Au/ZnO
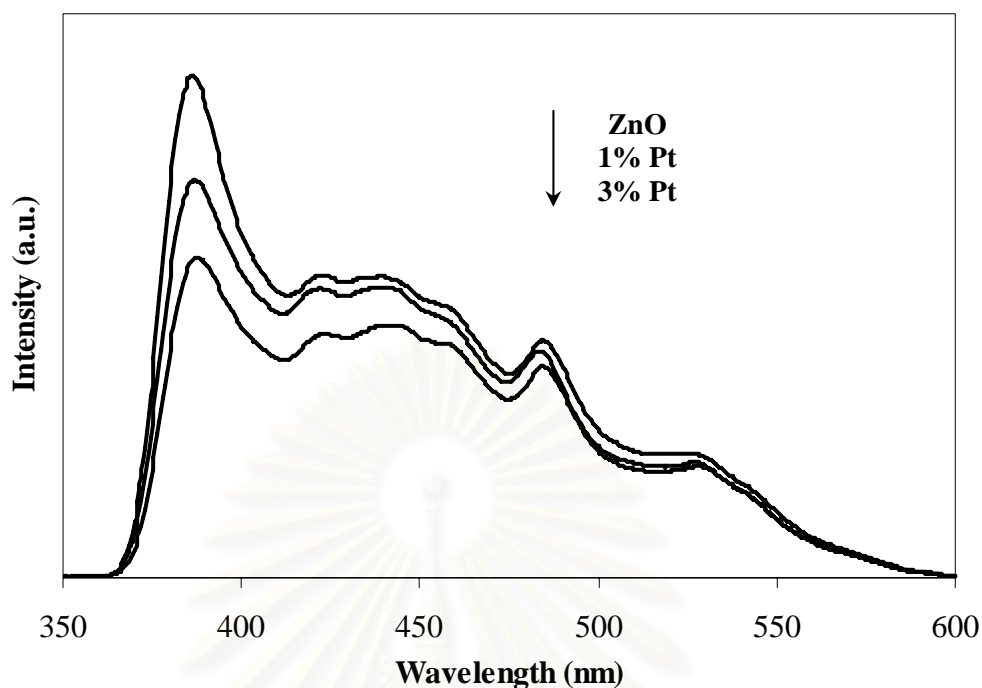
(b) Pt/ZnO

Figure 5.11 PL spectra for Au/ZnO (a) and Pt/ZnO (b) composites with various metal content with the excitation wavelength of 325 nm.

In this study, the PL emission spectra of different FSP made Au/ZnO ant Pt/ZnO catalysts were examined and compared to the pure ZnO with excitation wavelength of 325 nm. The results are shown in Figure 5.11 the spectrum of pure ZnO powders mainly consists of two emission bands: one is the UV near-band-edge emission (NBE) at ~385 nm. The other is the visible emission that usually associates with the deep level emission (DLE) in ZnO. The blue emission at ~ 425 nm and weak blue emission at ~ 445 nm most likely occurs from the donor level of Zn interstitial (Zn_i) to acceptor energy level of Zn vacancy (Zn_O). The blue–green band around 470 nm by radiative transition of electron from shallow donor levels, created by the oxygen vacancy to valence band. The green emission at ~ 530 is commonly observed for ZnO, and is attributed to the singly ionized oxygen vacancy in ZnO. The UV near-band-edge emission (NBE) spectra of the Pt/ZnO, Au/ZnO and Pure ZnO showed similar positions peaks, but with different PL intensities. It can be concluded that deposition of Pt and Au on ZnO did not change the band edge very much, but could

reduce PL emission significantly. The PL intensity of ZnO nanoparticles decreased with increasing amount of both Au and Pt deposited. It may be possibly attributable to the capture of noble metal ions. Moreover, the PL emission mainly results from the recombination of excited electrons and holes, the lower PL intensity suggests the lower recombination rate of electron–holes under irradiation of visible light. Therefore, for the noble metal-doped system, the weaker the excitonic PL spectrum results in the higher separation rate of photo-induced charges carriers (Liqiang *et al.*,2006). From this figure, the PL emission spectrum of Au/ZnO was lower than that of Pt/ZnO especially at deep level emission. Thus, FSP-made Au/ZnO had higher separation rate of the photo-induced charges than the FSP-made Pt/ZnO.

5.1.1.1 Atomic Absorption Spectroscopy (AAS)

The actual amounts of gold and platinum on the FSP-Au/ZnO and FSP-Pt/ZnO catalysts were determined using Atomic Absorption Spectroscopy and the results are shown in Table 5.8. The actual metal loadings of FSP made Au/ZnO were not different from the desired Au loading. However, the actual metal loadings of FSP made Pt/ZnO were only half of the desired Pt loadings.

Table 5.8 Atomic absorption Spectroscopy (AAS) of FSP made Au/ZnO and Pt/ZnO.

Sample	Metal loading (wt%)
Pt 1 wt.% - ZnO	0.5
Pt 3 wt.% - ZnO	1.5
Au 1 wt.% - ZnO	0.9
Au 3 wt.% - ZnO	2.7
Au 5 wt.% - ZnO	4.9

5.2.2 Photocatalytic testing

(a) Au/ZnO   (b) Pt/ZnO
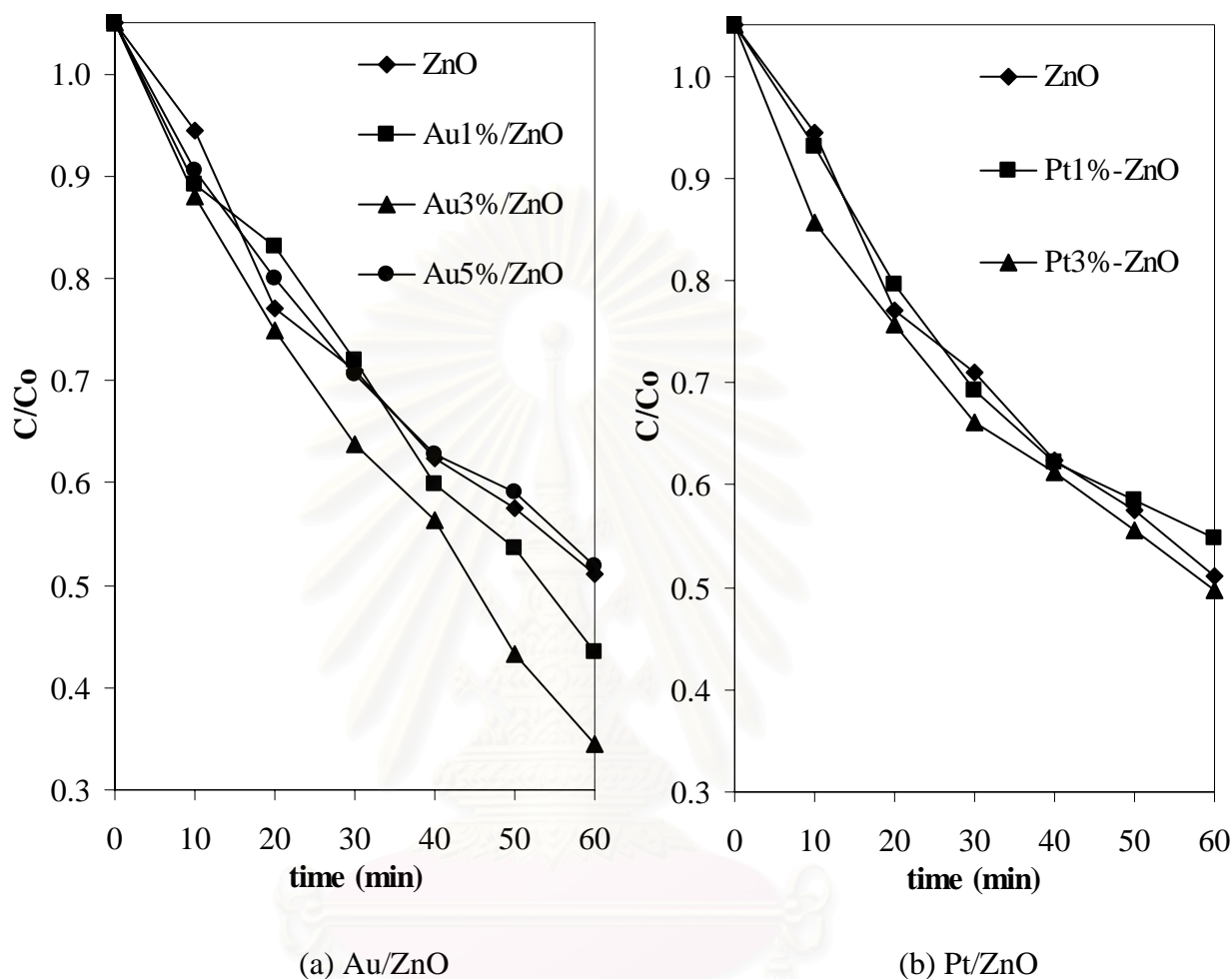
Figure 5.12 Photodegradation kinetics of MB using FSP made Au/ZnO (a) FSP made Pt/ZnO (b).

Figure 5.12 shows photodegradation kinetics of MB using FSP made Au/ZnO (a) nand FSP made Pt/ZnO (b). For FSP-made Au/ZnO powders, the experiment demonstrated that the observed photo-activity was increased by increasing the content of Au up to 3 wt.%, and then decreased by further increasing the content of Au to the 5 wt.%. This result implies that there was an optimum molar content of Au at 3 wt.%. The results showed that addition Au can enhance the photo-catalytic activity of pure ZnO. The enhancement of the photocatalytic activities can be achieved through the inclusion of a low loading of Au on the FSP-made ZnO particles. Au clusters at a lower concentration (smaller size of Au nanoparticles) probably act as a separation

center. The photogenerated electrons are stored in the Au nanoparticles and induce the Fermi-level shift toward more negative potentials. The transfer of electrons to Au nanoparticles continues until the Fermi level reaches close to the conduction band edge of ZnO. The recombination of the photogenerated electron–hole pairs in the ZnO crystal are thus reduced, and thereby, promoting the photocatalytic activity (Subramanian *et al*.,2003). These results were consistent with the PL spectra measurement from Figure 5.11a. However, in the case of FSP-made Au/ZnO nanoparticles with Au loading higher than 3 wt.% (larger size of Au nanoparticles), the intensity of the incident irradiation for ZnO nanoparticles absorption was reduced by scattering due to the larger Au nanoparticles deposited on ZnO nanoparticles. With a decreased in surface area, the adsorption of dye molecules on the catalyst surface was also reduced. From Figure 5.11a, the intensity of PL spectra of the FSP-made 5 wt.% Au/ZnO was not reduced much from that of the FSP-made 3 wt.% Au/ZnO, indicating that FSP-made 5 wt.% Au/ZnO did not improve the separation of photo-induced charges. Therefore, the enhancement of the photocatalytic activities was not achieved when the FSP made 5 wt.% Au/ZnO was used in the photodegradation of MB.

In case of FSP Pt/ZnO, the poor photocatalytic activity of Pt/ZnO was observed. The reason for this would be related with the nature of metal nanoparticles brought in contact with the irradiated semiconductor. Pt is ohmic type which differs from case of FSP made Au/ZnO. Pt deposited on ZnO did not induce the Fermi-level shift toward more negative potentials and store photogenerated electrons in the Pt nanoparticles but it capping merely facilitates discharge of the photogenerated electrons into the electrolyte (Subramanian *et al*.,2003). The mechanism of photoinduced charge separation and charge distribution in Pt/ZnO and Au/ZnO nanocomposites are shown in figure 2.8. Thus, Pt deposited on ZnO did not produce a longer electron–hole pair separation lifetime and enhance photocatalytic activity. These results are in agreement with the PL spectra measurement from Figure 5.11b. Moreover, Pt deposited on ZnO would block the UV light penetration into samples and reduced the surface contact area between MB solution and ZnO. Therefore, the

enhancement of the photocatalytic activities could not be achieved when the FSP made Pt/ZnO was used in photodegradation of MB.

The $-\ln(C/C_0)$ versus time curves of the MB photodegradation using ZnO, Au/ZnO and Pt/ZnO photocatalysts are shown in Fig. 5.13. All curves are linear, revealing that the kinetic data of the MB photodegradation fitted well to the first-order reaction kinetic model. The apparent first-order reaction rate constants calculated from the slopes of those curves are shown in Table 5.9.
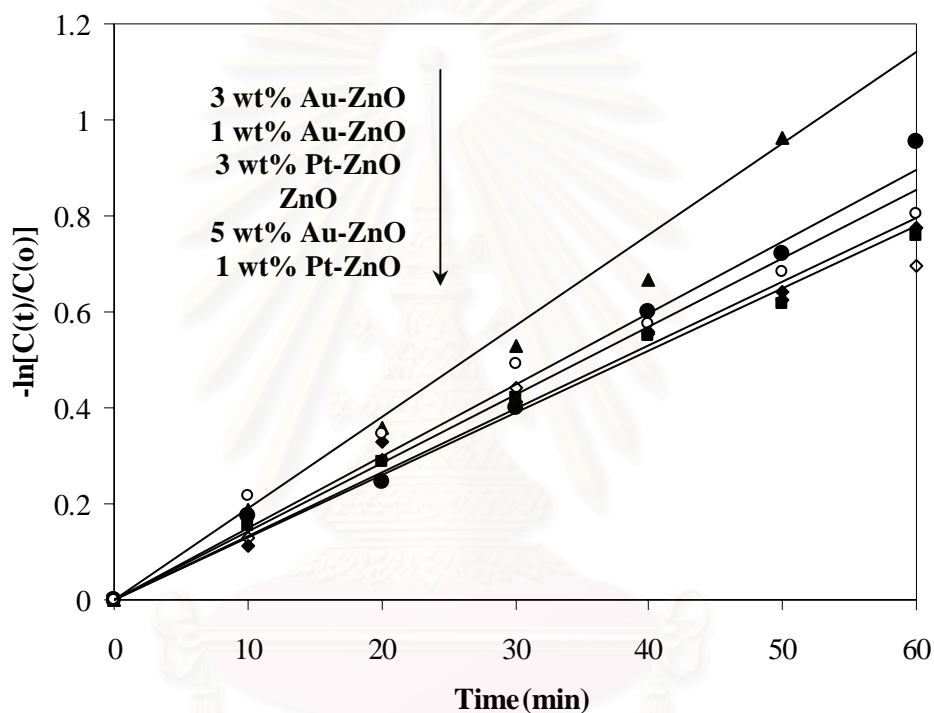
Figure 5.13 The first-order kinetics of MB photo-degradation in presence of FSP-made Au/ZnO (filled symbols) and Pt/ZnO (open symbols).

Table 5.9 Reaction performance in photodegradation methylene blue of pure ZnO, Au/ZnO, and Pt/ZnO prepared via FSP method and P25 and JRC titania are reported for comparison.

Sample	MB conversion after 1 h. (%)	Rate constant (1/h)
ZnO	54	0.80
Pt 1 wt.% - ZnO	50	0.73
Pt 3 wt.% - ZnO	55	0.85
Au 1 wt.% - ZnO	62	0.89
Au 3 wt.% - ZnO	71	1.14
Au 5 wt.% - ZnO	53	0.78
TiO_2 (JRC)	18	0.19
TiO_2 (P25)	57	0.80

Table 5.9 shows summary percent degradation of methylene blue and pseudo first-order rate constants of pure ZnO, Au/ZnO, and Pt/ZnO prepared by the FSP method. Degussa P25 (d_{xrd} = 20.1 nm and surface area = 51.6 m^2/g) and JRC titania (d_{xrd} = 15.5 nm and surface area = 73.2 m^2/g) are included here as reference samples. From this table, the FSP made 3 wt.% Au/ZnO exhibited the highest photocatalytic activity. The percent degradation of MB increased from pure ZnO about 17 %. It also outperformed the commercial titania powder about 14 % for Degussa P25 and 53 % for JRC nanosized titania. The FSP made 3 wt.% Pt/ZnO, on the other hand, showed little improvement in the photocatalytic activity of MB while the 1 wt.% Pt/ZnO showed lower photocatalytic activity than pure ZnO.

CHAPTER VI

CONCLUSIONS AND RECOMMENDATIONS

In this chapter, section 6.1 provides the conclusions obtained from the experimental results of the effect of crystallite size on the photocatalytic activity of FSP made ZnO and annealed-FSP ZnO and photocatalytic degradation of methylene blue by Pt/ZnO and Au/ZnO catalysts prepared by FSP method. Additionally, recommendations for future study are given in section 6.2.

6.1 Conclusions

1. The photocatalytic activity of ZnO nanoparticles synthesized by the FSP method with various crystallite sizes (8.8-47.0 nm) in degradation of methylene blue increased with increasing ZnO crystallite size with ZnO-47 nmexhibited the highest activity. The improvement in photocatalytic performance is suggested to be due to the higher crystllinity, surface oxygen vacancies, and defects of ZnO particles so that surface trapping sites and e^-/h^+ pair separation were enhanced.

2. Further increase of the ZnO crystallite size to 53.6-103.5 nm by annealing at high temperature gradually decreased the photocatalytic performance at ZnO. Decreasing of the activity of ZnO with crystallite size larger than size 47 nm was likely to arise from the decreasing of crystallite quality and surface availability of the ZnO particles for reactant adsorption and light absorption.

3. Compare to the commercial titania powder Degussa P25 and JRC nanosized titania, the FSP-ZnO with average crystallite size 30 nm and greater show higher performance in the photocatalytic degradation of MB.

4. The FSP-made Au/ZnO exhibited higher photocatalytic activity than pure FSP-ZnO and the reference commercial titania powders with the 3 wt.% Au/ZnO gave the highest photodegradation rate of MB. However, the reaction rate was decreased as the Au loadings increased further to 5 wt.%. The experimental results demonstrated that

the ZnO doped with Au had a stronger absorption of visible light and a lower intensity of PL emission than the undoped ZnO. The presence of discrete Au clusters may retarded the recombination of the photoinduced electron–hole pairs by shift in the Fermi level and store photogenerated electrons in them. Decreasing activity at higher loading (5 wt.%.) is likely to arise from the effect of larger size of Au resulting in a decreased surface availability on the particles for reactant adsorption and light absorption.

5. Addition of Pt did not improve the photocatalytic activity of the FSP-ZnO. The poor photocatalytic activity of Pt/ZnO was probably resulted from the ohmic type of Pt which facilitated discharge of the photogenerated electrons into the electrolyte and the effect of Pt particles blocking the UV light penetration into the samples.

6.2 Recommendations

1. The photocatalytic activity of ZnO with various crystallite sizes, nanocrystalline Au/ZnO, and Pt/ZnO catalysts that were prepared by FSP method should be investigated in other reaction conditions that catalyst loading, pH value, and the initial dye concentration are varied.

2. The measurement of active site of the nanocrystalline Au/ZnO and Pt/ZnO catalysts should be reported.

REFERENCES

Akyol, A.; Yatmaz, H.C. and Bayramoglu, M. Photocatalytic decolorization of Remazol Red RR in aqueous ZnO suspensions. <u>Applied Catalysis B: Environmental</u> 54 (2004): 19–24.

Alinsafi, A.; Khemis, M.; Pons, M.N.; Leclerc, J.P.; Yaacoubi, A.; Benhammou, A. and Nejmeddine, A. Coagulation–flocculation–decantation of dye house effluents: concentrated effluents. <u>Chemical Engineering and Processing</u> 44 (2005): 461–470.

Alivisatos, A. P. Perspectives on the Physical Chemistry of Semiconductor Nanocrystals. <u>Journal of Physical Chemistry</u> 100 (1996): 13226-13239.

Behnajady, M.A.; Modirshahla, N. and Hamzavi, R. Kinetic study on photocatalytic degradation of C.I. Acid Yellow 23 by ZnO photocatalyst. <u>Journal of Hazardous Materials</u> B133 (2006): 226–232.

Benedix, R.; Dehn, F.; Quaas, J. and Orgass, M. Application of Titanium Dioxide Photocatalysis to Create Self-Cleaning Building Materials. <u>LACER</u> 5 (2000): 152-168.

Beydoun, D.; Amal, R.; Low, G. and McEvoy, S. Role of nanoparticles in photocatalysis. <u>Journal of Nanoparticle Research</u> 1(1999): 439–458.

Cerischer, H. and Heller, A. The Role of Oxygen in Photooxidation of Organic Molecules on Semiconductor Particles. <u>Journal of Physical Chemistry</u> 95 (1991): 5261-5267.

Chakrabarti, S. and Dutta, B. K. Photocatalytic degradation of model textile dyes in wastewater using ZnO as semiconductor catalyst. <u>Journal of Hazardous Materials B</u> 112 (2004): 269–278.

Chu, D.; Zeng, Y. and Jiang, D. Hydrothermal synthesis and optical properties of Pb_2^+ doped ZnO nanorods. <u>Materials Letters</u> 60 (2006): 2783–2785.

Daneshvar, N.; Salari, D.and Khataee, A.R. Photocatalytic degradation of azo dye acid red 14 in water on ZnO as an alternative catalyst to TiO_2. <u>Journal of Photochemistry and Photobiology A: Chemistry</u> 162 (2004): 317–322.

Dodd, A. C.; McKinley, A. J.; Saunders, M. and Tsuzuki, T. Effect of particle size on the photocatalytic activity of nanoparticulate zinc oxide. <u>Journal of Nanoparticle Research</u> 8 (2006): 43–51.

Golob, V.; Vinder, A. and Simonič, M. Efficiency of the coagulation/flocculation method for the treatment of dyebath effluents. Dyes and Pigments 67 (2005): 93-97.

Gouvêa, C.; Wypycha, F.; Moraesb, S.G.; Durʾan, N. and Peralta-Zamora, P. Semiconductor-assisted photodegradation of lignin, dye, and kraft effluent by Ag-doped ZnO. Chemosphere 40 (2000): 427-432.

Height, M. J.; Pratsinis, S. E.; Mekasuwandumrong, O. and Praserthdam, P. Ag-ZnO catalysts for UV-photodegradation of methylene blue. Applied Catalysis B: Environmental 63 (2006): 305–312.

Henglein, A. Small-Particle Research: Physicochemical Properties of Extremely Small Colloidal Metal and Semiconductor Particles Chemical Reviews 89 (1989): 1861-1873.

Hoffmann, M. R.; Martin, S. T.; Choi, W.; and Bahnemannt, D. W. Environmental Applications of Semiconductor Photocatalysis. Chemical Reviews 95 (1995): 69-96.

Jang, H. D.; Chang, H.; Suh, Y. and Okuyama, K. Synthesis of SiO_2 nanoparticles from sprayed droplets of tetraethylorthosilicate by the flame spray pyrolysis. Current Applied Physics 6S1 (2006): e110–e113.

Jang, Y. J.; Simer, C. and Ohm, T. Comparison of zinc oxide nanoparticles and its nano-crystalline particles on the photocatalytic degradation of methylene blue. Materials Research Bulletin 41 (2006): 67–77.

Kavitha, R.; Meghani, S. and Jayaram, V. Synthesis of titania films by combustion flame spray pyrolysis technique and its characterization for photocatalysis. Materials Science and Engineering B 139 (2007): 134–140.

Khodja, A. A.; Sehili, T.; Pilichowski, J. and Boule ,P. Photocatalytic degradation of 2-phenylphenol on TiO_2 and ZnO in aqueous suspensions. Journal of Photochemistry and Photobiology A: Chemistry 141 (2001): 231–239.

Kolen'ko, Y. V.; Churagulov, B. R.; Kunst, M.; Mazerolles, L. and Colbeau-Justin, C. Photocatalytic properties of titania powders prepared by hydrothermal method. Applied Catalysis B: Environmental 54 (2004): 51–58.

Leiter, F.; Alves, H.; Pfisterer, D.; Romanov, N.G.; Hofmann, D.M. and Meyer, B.K. Oxygen vacancies in ZnO. Physica B 340–342 (2003): 201–204.

Li, D.; Balek, V.; Ohashi, N.; Mitsuhashi, T.; Hishita, S.; Haneda, H. Self-assembly prismatic aggregates formed during the calcination of ZnO powders: In situ monitoring by ETA technique and their photocatalytic properties. Journal of Colloid and Interface Science 289 (2005): 472–478.

Li, F. B. and Li, X. Z. The enhancement of photodegradation efficiency using Pt–TiO_2 catalyst. Chemosphere 48 (2002): 1103–1111.

Li, F. B. and Li, X. Z. Photocatalytic properties of gold/gold ion-modified titanium dioxide for wastewater treatment. Applied Catalysis A: General 228 (2002): 15–27.

Li, X. Z.; Li, F. B.; Yang, C. L. and Ge, W. K. Photocatalytic activity of WOx-TiO2 under visible light irradiation. Journal of Photochemistry and Photobiology A: Chemistry 141 (2001): 209–217.

Li, X. Z.; B.; Zhu, H.; Dong, X.; Xia, X.; Cui, Y.; Huang, K. and Du, G. Properties of ZnO thin films grown on Si substrates by photo-assisted MOCVD. Applied Surface Science (2007).

Lim, J.; Shin, K.; Kim, H.W. and Lee, C. Effect of annealing on the photoluminescence characteristics of ZnO thin films grown on the sapphire substrate by atomic layer epitaxy. Materials Science and Engineering B107 (2004): 301–304.

Liqiang, J.; Dejun, W.; Baiqi, W.; Shudan, L.; Baifu, X.; Honggang, F. and Jiazhong, S. Effects of noble metal modification on surface oxygen composition, charge separation and photocatalytic activity of ZnO nanoparticles. Journal of Molecular Catalysis A: Chemical 244 (2006): 193–200.

Liqiang, J.; Fulong, Y.; Haige, H.; Baifu, X.; Weimin, C. and Honggang, F. Relationships of surface oxygen vacancies with photoluminescence and photocatalytic performance of ZnO nanoparticles. Science in China Series B Chemistry 48 (2005): 25-30.

Liqiang, J.; Yichun, Q.; Baiqi, W.; Shudan, L.; Baojiang, J.; Libin, Y.; Wei, F.; Honggang, F. and Jiazhong, S. Review of photoluminescence performance of nano-sized semiconductor materials and its relationships with photocatalytic activity. Solar Energy Materials & Solar Cells 90 (2006): 1773–1787.

Marı´, B.; Manjo´n, F.J.; Mollar, M.; Cembrero, J. and Go´mez, R. Photoluminescence of thermal-annealed nanocolumnar ZnO thin films grown by electrodeposition. Applied Surface Science 252 (2006): 2826–2831.

Mills, A. and Lee, S. K. A web-based overview of semiconductor photochemistry-based current commercial applications. Journal of Photochemistry and Photobiology A: Chemistry 152 (2002): 233–247.

Nagaveni, K.; Sivalingam, G.; Hegde, M.S. and Madras, G. Solar photocatalytic degradation of dyes:high activity of combustion synthesized nano TiO_2. Applied Catalysis B: Environmental 48 (2004): 83–93.

Papić, S.; Koprivanac, N.; Božić, A. L.; Metes, A. Removal of some reactive dyes from synthetic wastewater by combined Al(III) coagulation/carbon adsorption process. Dyes and Pigments 62 (2004): 291–298.

Park, S.; Park, H.; Yoo, K.; Lee, J. and Lee, J.C. Photocatalytic recovery of Ag ions from wastewater using ZnO nanopowders immobilized on microporous alumina substrates. Colloids and Surfaces A: Physicochemical and Engineering Aspects 300 (2007): 30–34.

Pratsinis, S. E. Flame aerosol synthesis of ceramic powders. Progress in Energy and Combustion Science 24 (1998): 197-219.

Robert, D. and Malato, S. Solar photocatalysis: a clean process for water detoxification. The Science of the Total Environment 291 (2002): 85–97.

Sakthivel, S.; Neppolian, B.; Shankar, M.V.; Arabindoo, B.; Palanichamy, M. and Murugesan, V. Solar photocatalytic degradation of azo dye: comparison of photocatalytic efficiency of ZnO and TiO_2. Solar Energy Materials & Solar Cells 77 (2003): 65–82.

Sakthivel, S.; Shankar, M.V.; Palanichamy, M.; Arabindoo, B.; Bahnemann, D.W. and Murugesan, V. Enhancement of photocatalytic activity by metal deposition: characterisation and photonic efficiency of Pt, Au and Pd deposited on TiO_2 catalyst. Water Research 38 (2004): 3001–3008.

Senthilkumaar, S.; Porkodi, K.; Gomathi, R.; Maheswari, A. G. and Manonmani, N. Solegel derived silver doped nanocrystalline titania catalysed

photodegradation of methylene blue from aqueous solution. <u>Dyes and Pigments</u> 69 (2006): 22–30.

Senthilkumaar, S.; Porkodi, K. and Vidyalakshmi, R. Photodegradation of a textile dye catalyzed by sol–gel derived nanocrystalline TiO_2 via ultrasonic irradiation. <u>Journal of Photochemistry and Photobiology A: Chemistry</u> 170 (2005): 225–232.

Serpone, N.; Lawless, D. and Khairutdinov, R. Subnanosecond Relaxation Dynamics in TiO_2 Colloidal Sols (Particle Sizes R, =1.0- 13.4 nm). Relevance to Heterogeneous Photocatalysis. <u>Journal of Physical Chemistry</u> 99 (1995): 16655-16661.

Sharma, A.; Rao P.; Mathur R.P. and Ameta S. C. Photocatalytic reactions of xylidine ponceau on semiconducting zinc oxide powder <u>Journal of Photochemistry and PhotobiologyA: Chemistry</u> 86 (1995): 197-200.

Subramanian, V.; Wolf, E. E. and Kamat, P. V. Catalysis with TiO2/Gold Nanocomposites. Effect of Metal Particle Size on the Fermi Level Equilibration. <u>Journal of Physical Chemistry B</u> 105 (2001): 11439–11446.

Subramanian, V.; Wolf, E. E. and Kamat, P. V. Green Emission to Probe Photoinduced Charging Events in ZnO-Au Nanoparticles. Charge Distribution and Fermi-Level Equilibration. <u>Journal of Physical Chemistry B</u> 107 (2003): 7479–7485.

Strobel, R.; Krumeich, F.; Stark, W.J.; Pratsinis S.E. and Baiker, A. Flame spray synthesis of Pd/Al_2O_3 catalysts and their behavior in enantioselective hydrogenation <u>Journal of Catalysis</u> 222 (2004): 307–314.

Tanaka, K.; Padermpole, K. and Hisanaga, T. Photocatalytic Degradation of Commercial AZO dyes. <u>Water Research</u> 34 (2000): 327 – 333.

Tani, T.; Kato, A. and Morisaka, H. Effect of solvent on powder characteristic of Zinc Oxide and Magnesia prepared by flame spray pyrolysis. <u>Journal of the Ceramic Society of Japan</u> 113 [3] (2005): 255–258.

Tani, T.; Madler, L. and Pratsinis, S. E. Homogeneous ZnO nanoparticles by flame spray pyrolysis. <u>Journal of Nanoparticle Research</u> 4 (2002): 337–343.

Teoh, W. Y.; Amal, R.; Madlera, L. and Pratsinisa, S. E. Flame sprayed visible light-active Fe-TiO$_2$ for photomineralisation of oxalic acid. <u>Catalysis Today</u> 120 (2007): 203–213.

Teoh, W. Y.; Madlera, L.; Beydounb, D.; Pratsinisa, S. E. and Amal, R. Direct (one-step) synthesis of TiO$_2$ and Pt/TiO$_2$ nanoparticles for photocatalytic mineralisation of sucrose. <u>Chemical Engineering Science</u> 60 (2005): 5852 – 5861.

Vanheusden, K.; Warren, W. L.; Seager, C. H.; Tallant, D. R.; Voigt, J. A. and Gnade, B. E. Mechanisms behind green photoluminescence in ZnO phosphor powders. <u>Journal of Applied Physics</u> 79 (1996): 7983-7990.

Wang, H.; Xie, C.; Zhang, W.; Cai, S.; Yang, Z.; Gui, Y. Comparison of dye degradation efficiency using ZnO powders with various size scales. <u>Journal of Hazardous Materials</u> 141 (2007): 645–652.

Wang, J. and Gao, L. Hydrothermal synthesis and photoluminescence properties of ZnO nanowires. <u>Solid State Communications</u> 132 (2004): 269–271.

Wei, X.Q.; Man, B.Y.; Liu, M.; Xue, C.S.; Zhuang, H.Z. and Yang, C. Blue luminescent centers and microstructural evaluation by XPS and Raman in ZnO thin films annealed in vacuum, N$_2$ and O$_2$. <u>Physica</u> B 388 (2007): 145–152.

Wu, J. J. and Tseng, C. H. Photocatalytic properties of nc-Au/ZnO nanorod composites. <u>Applied Catalysis B: Environmental</u> 66 (2006): 51–57.

Zhang, Z.; Wang, C.; Zakaria, R. and Ying, J.Y. Role of Particle Size in Nanocrystalline TiO$_2$-Based Photocatalysts. <u>Journal of Physical Chemistry B</u> 102 (1998): 10871-10878.

APPENDICES

APPENDIX A

CALCULATION FOR CATALYST PREPARATION
FLAME SPRAY PYROLYSIS

Preparation of ZnO nanopowders with various crystallite sizes and nanocrystalline Au-ZnO and Pt-ZnO catalysts by flame spray pyrolysis (FSP) are shown as follows:

Reagent:
- Platinum acetylacetonate
    Molecular weight = 393.31 g
- Gold (III) chloride trihydrate
    Molecular weight = 393.83 g
- Zinc naphthanate
    8 wt.% of Zinc
    Density = 0.962 g/ml
- Ethanol
- Acetonitrile
- Xylene

Example calculation for the preparation of 1 wt.% Au/ZnO 0.8 molar Volume of solution 200 ml

The total concentration of metal was 0.8 molar = total metal 0.8 mole in volume of solution

Volume of solution 200 ml = $\dfrac{200 \text{ ml} \times 0.8 \text{ mole}}{1000 \text{ ml}}$ = 0.16 mole

Based on 100 g for catalyst used, the composition of the catalyst will be as follows:

$$Au \quad = \quad 1 \text{ g}$$
$$ZnO \quad = \quad 100 - 1 \ = 99 \text{ g}$$

Convert unit from mass to mol

$$\text{Au} \quad = \quad \frac{1 \text{ g}}{196.9665 \text{ g}} \quad = 5.08 \times 10^{-3} \text{ mole}$$

$$\text{ZnO} \quad = \quad \frac{99 \text{ g}}{81.39 \text{ g}} \quad = 1.216 \text{ mole}$$

Mole of total metal = 5.08×10^{-3} mole + 1.216 mole = 1.221 mole

Adjust mol of total metal to 0.16 mole

$$\text{Au} \quad = \quad \frac{5.08 \times 10^{-3} \text{ mole} \times 0.16 \text{ mole}}{1.221 \text{ mole}} \quad = 8.31 \times 10^{-4} \text{ mole}$$

$$\text{ZnO} \quad = \quad \frac{1.216 \text{ mole} \times 0.16 \text{ mol}}{1.221 \text{ mole}} \quad = 1.593 \text{ mole}$$

Au 8.31×10^{-4} mole was prepared from Gold (III) chloride trihydrate and as ZnO 1.593 mole was prepared from Zinc naphthanate

Gold (III) chloride trihydrate required = 8.31×10^{-4} mole × 393.83 g = 0.263 g

Zinc required = 1.593 mole × 65.39 g = 10.42 g

$$\text{zincnaphthanate required} = \quad \frac{100 \text{ g} \times 10.42 \text{ g}}{8 \text{ g.} \times 0.962 \text{ ml/g}} \quad = 135.38 \text{ ml}$$

For 200 ml of solution

$$\text{Ethanol required} \quad = 200 \text{ ml} - 135.38 \text{ ml} = 64.62 \text{ ml}$$

Example calculation for the preparation of 1 wt.% Pt/ZnO 0.8 molar Volume of solution 200 ml

The total concentration of metal was 0.8 molar = total metal 0.8 mole in volume of solution

$$\text{Volume of solution 200 ml} = \frac{200 \text{ ml} \times 0.8 \text{ mole}}{1000 \text{ ml}} = 0.16 \text{ mole}$$

Based on 100 g for catalyst used, the composition of the catalyst will be as follows:

$$\text{Pt} \quad = \quad 1 \text{ g}$$

$$\text{ZnO} \quad = \quad 100 - 1 = 99 \text{ g}$$

Convert unit from mass to mol

$$\text{Pt} \quad = \quad \frac{1 \text{ g}}{196.078 \text{ g}} \quad = 5.126 \times 10^{-3} \text{ mole}$$

$$\text{ZnO} \quad = \quad \frac{99 \text{ g}}{81.39 \text{ g}} \quad = 1.216 \text{ mole}$$

Mole of total metal = 5.126×10^{-3} mole + 1.216 mole = 1.221 mole

Adjust mol of total metal to 0.16 mole

$$\text{Au} \quad = \quad \frac{5.126 \times 10^{-3} \text{ mole} \times 0.16 \text{ mole}}{1.221 \text{ mole}} = 6.74 \times 10^{-4} \text{ mole}$$

$$\text{ZnO} \quad = \quad \frac{1.216 \text{ mole} \times 0.16 \text{ mol}}{1.221 \text{ mole}} = 1.593 \text{ mole}$$

Au 6.74×10^{-4} mole was prepared from Platinum acetylacetonate and as ZnO 1.593 mole was prepared from Zinc naphthanate

Gold (III) chloride trihydrate required = 6.74×10^{-4} mole $\times$ 393.31 g = 0.265 g

Zinc required =1.593 mole $\times$ 65.39 g = 10.418 g

zincnaphthanate required = $\dfrac{100 \text{ g} \times 10.418 \text{ g}}{8 \text{ g.} \times 0.962 \text{ ml/g}}$ = 135.38 ml

For 200 ml of solution

Acetonitrile required = (200 ml – 135.38 ml) $\times$0.3 = 19.39 ml

Xylene required = (200 ml – 135.38 ml) $\times$ 0.7 = 45.24 ml

APPENDIX B

CALCULATION OF THE CRYSTALLITE SIZE

Calculation of the crystallite size by Scherrer equation

The crystallite size was calculated from the half-height width of the diffraction peak of XRD pattern using the Debye-Scherrer equation.

From Scherrer equation:

$$D = \frac{K\lambda}{\beta \cos \theta} \tag{B.1}$$

where D = Crystallite size, Å

K = Crystallite-shape factor = 0.9

λ = X-ray wavelength, 1.5418 Å for CuKα

θ =   Observed peak angle, degree

β = X-ray diffraction broadening, radian

The X-ray diffraction broadening (β) is the pure width of a powder diffraction free of all broadening due to the experimental equipment. Standard α-alumina is used to observe the instrumental broadening since its crystallite size is larger than 2000 Å. The X-ray diffraction broadening (β) can be obtained by using Warren's formula.

From Warren's formula:

$$\beta^2 = B_M^2 - B_S^2 \tag{B.2}$$

$$\beta = \sqrt{B_M^2 - B_S^2}$$

Where B_M = The measured peak width in radians at half peak height.

B_S = The corresponding width of a standard material.

Example: Calculation of the crystallite size of ZnO (47.0 nm) prepared by Flame spray pyrolysis method

The half-height width of peak $\quad$ = $\quad 0.32^{\circ}$ (from Figure B.1)

$\qquad\qquad\qquad\qquad\qquad\qquad$ = $\quad (2\pi \times 0.30)/360$

$\qquad\qquad\qquad\qquad\qquad\qquad$ = $\quad 0.00524$ radian

The corresponding half-height width of peak of α-alumina $\quad$ = $\quad 0.00524$ radian

The pure width $\qquad$ = $\qquad \sqrt{B_M^2 - B_S^2}$

$\qquad\qquad\qquad\qquad$ = $\qquad \sqrt{0.00524^2 - 0.0041^2}$

$\qquad\qquad\qquad\qquad$ = $\qquad 0.00326$ radian

$\beta \quad = \quad 0.003796$ radian

$2\theta \quad = \quad 36.24^{\circ}$

$\theta \quad = \quad 18.12^{\circ}$

$\lambda \quad = \quad 1.5418$ Å

The crystallite size $\quad$ = $\quad \dfrac{0.9 \times 1.5418}{0.003796 \cos 18.12}$ $\qquad$ = $\qquad 470.98$ Å

$\qquad\qquad\qquad\qquad\qquad$ = $\qquad 47.10$ nm

86
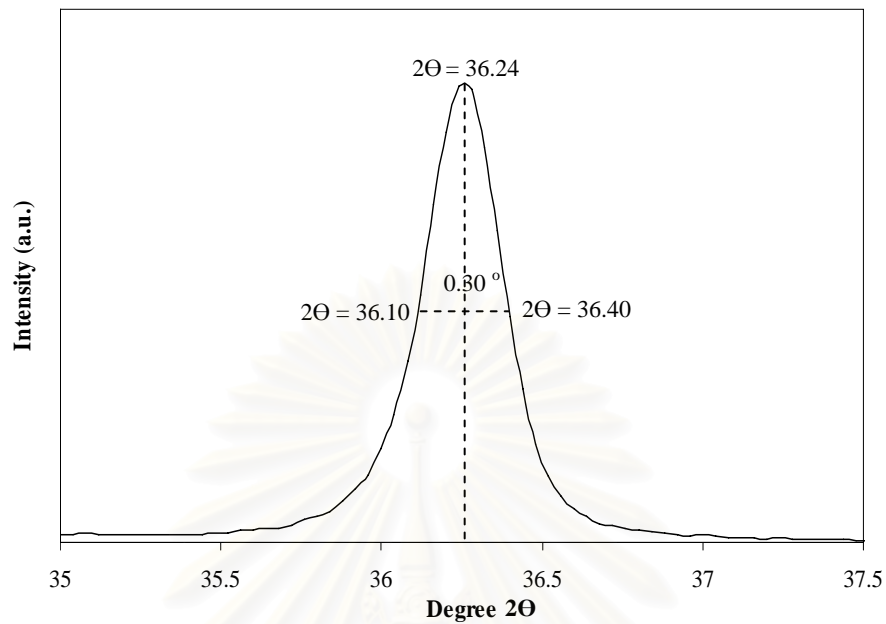
Figure B.1 The measured peak of ZnO (47.0 nm) prepared by Flame spray pyrolysis method to calculate the crystallite size.
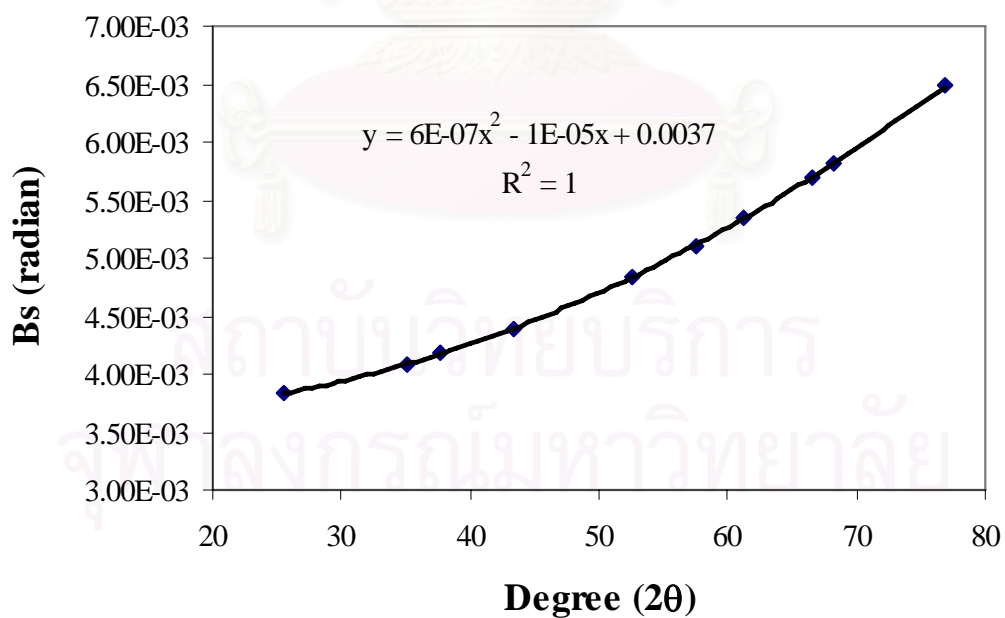
Figure B.2 The plot indicating the value of line broadening due to the equipment. The data were obtained by using α-alumina as standard

APPENDIX C

CALIBRATION CURVE

This appendix showed the calibration curves for calculation concentration of methylene blue in Photocatalytic degradation of methylene blue reaction.

$y = 0.1655x - 0.0418$
$R^2 = 0.9991$
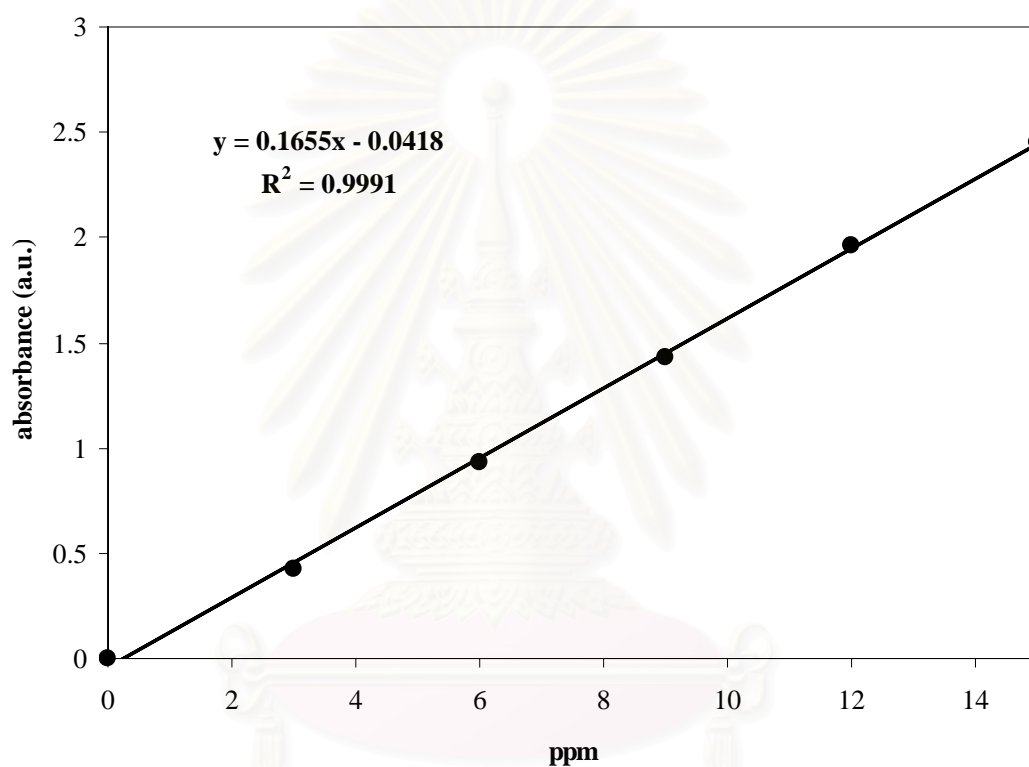
Figure C.1 The calibration curve of methylene blue from UV–Vis scanning spectrophotometer Perkin - Elmer lampda 650.

APPENDIX D

LIST OF PUBLICATIONS

1. Pongsapak Pawinrat, Joongjai Panpranot, Okorn Mekasuwandumrong and Piyasan Praserthdam, "Photocatalytic Degradation of Methylene blue by ZnO Catalysts Prepared by Flame Spray Pyrolysis Method", <u>Proceeding of the 17th Thailand Chemical Engineering and Applied Chemistry Conference</u>, Chiang Mai Thailand, October, 2007.

2. Pawinrat, P., Panpranot, J., Praserthdam, P., and Mekasuwandumrong, O., Direct one-step synthesis of ZnO nanoparticles: Relations between crystallite size and photocatalytic activity. <u>Applied Catalysis A: General</u> (2008), submitted.

3. Pawinrat, P., Panpranot, J., Praserthdam, P., and Mekasuwandumrong, O., Synthesis of nanocrystalline Au-ZnO and Pt-ZnO by flame spray pyrolysis and its application for photocatalytic degradation of dyes. <u>Applied Catalysis B. Environment</u> (2008), submitted.

การประชุมวิชาการวิศวกรรมเคมีและเคมีประยุกต์แห่งประเทศไทย ครั้งที่ 17

TIChE17

29 – 30 ตุลาคม 2550
ณ โรงแรมดิเอ็มเพรส
จ.เชียงใหม่

จัดโดย
สมาคมวิศวกรรมเคมีและเคมีประยุกต์แห่งประเทศไทย
ร่วมกับ
ภาควิชาเคมีอุตสาหกรรม คณะวิทยาศาสตร์ มหาวิทยาลัยเชียงใหม่

การย่อยสลายโดยใช้แสงของเมธิลีนบลูด้วยตัวเร่งปฏิกิริยาซิงค์ออกไซด์ที่สังเคราะห์
โดยวิธีเฟลมสเปรย์ไพโรไลซิส

พงศภัค ภวิลรัตน์[1], จูงใจ ปั้นประณต[1]*, โอกร เมฆาสุวรรณดำรง[2] และ ปิยะสาร ประเสริฐธรรม[1]

1) ศูนย์เชี่ยวชาญเฉพาะทางด้านคาตาไลซิสและวิศวกรรมปฏิกิริยาที่ใช้ตัวเร่งปฏิกิริยา ภาควิชาวิศวกรรมเคมี
คณะวิศวกรรมศาสตร์ จุฬาลงกรณ์มหาวิทยาลัย เขตพญาไท กรุงเทพฯ 10330

2) ภาควิชาวิศวกรรมเคมี คณะวิศวกรรมศาสตร์และเทคโนโลยีอุตสาหกรรม มหาวิทยาลัยศิลปากร นครปฐม 73000

1. บทนำ

น้ำเสียที่เจือปนด้วยกากของสีย้อมจากโรงงานทอผ้า, โรงงานกระดาษและโรงงานอื่นๆเป็นสาเหตุให้เกิดปัญหามลภาวะทางน้ำขึ้น โดยทั่วไปนั้นการบำบัดน้ำเสียจะใช้วิธีการดูดซับหรือวิธีการตกตะกอนด้วยสารเคมี ซึ่งทั้งสองวิธีนี้จะต้องเปลี่ยนสีย้อมจากสภาวะของเหลวให้กลายเป็นของแข็งก่อน แล้วจึงนำไปกำจัดต่อไป เป็นสาเหตุให้เกิดมลภาวะลำดับที่ 2 ขึ้น ดังนั้นการย่อยสลายโดยใช้แสงที่ใช้สารกึ่งตัวนำเป็นตัวเร่งปฏิกิริยาจึงเป็นทางเลือกหนึ่งซึ่งสามารถย่อยสลายสีย้อมได้

ในปฏิกิริยาการย่อยสลายโดยใช้แสงด้วยตัวเร่งปฏิกิริยานั้น ไทเทเนียมไดออกไซด์ได้ถูกนำมาใช้เป็นตัวเร่งปฏิกิริยาอย่างกว้างขวาง โดยซิงค์ออกไซด์นั้นเป็นตัวเลือกที่เหมาะสมที่จะนำมาใช้แทนไทเทเนียมไดออกไซด์เนื่องจากมีช่องว่างแถบพลังงานใกล้เคียงกันแต่ซิงค์ออกไซด์จะมีราคาถูกกว่าและมีประสิทธิภาพในปฏิกิริยาการย่อยสลายโดยใช้แสงด้วยตัวเร่งปฏิกิริยาสูงกว่าสำหรับการย่อยสลายสารอินทรีย์ในวัฏภาคของเหลว

มีหลากหลายวิธีที่ใช้ในการสังเคราะห์อนุภาคตัวเร่งปฏิกิริยาที่ใช้ในปฏิกิริยาการย่อยสลายโดยใช้แสงด้วยตัวเร่งปฏิกิริยา โดยวิธีเฟลมสเปรย์ไพโรไลซิสเป็นวิธีที่น่าสนใจและมีข้อดีคือ เป็นวิธีการสังเคราะห์อนุภาคโลหะออกไซด์ที่มีขนาดระดับนาโนเมตรในขั้นตอนเดียว สามารถควบคุมขนาดของอนุภาคได้ดี ผลิตอนุภาคที่มีขนาดระดับนาโนเมตรได้หลากหลายชนิดและให้ผลผลิตปริมาณมากในราคาต้นทุนต่ำ

2. อุปกรณ์และวิธีการทดลอง

2.1. สารเคมี

ซิงค์แนฟทาเนต, เอทานอล, เมธิลีนบลู, ไทเทเนียมไดออกไซด์ (Degussa P25), ไทเทเนียมไดออกไซด์ (JRC)

2.2. การสังเคราะห์ตัวเร่งปฏิกิริยาซิงค์ออกไซด์โดยเปลี่ยนแปลงขนาดของผลึกด้วยวิธีเฟลมสเปรย์ไพโรไลซิส

การสังเคราะห์ตัวเร่งปฏิกิริยาซิงค์ออกไซด์เริ่มจากเตรียมสารตั้งต้นโดยการละลายซิงค์แนฟทาเนตในเอทานอลเพื่อให้ได้ความเข้มข้นตั้งแต่ 0.3 ถึง 1โมลาร์ หลังจากนั้นป้อนสารตั้งต้นเข้าสู่เปลวไฟที่อัตราการป้อน 3, 5 และ 8 มิลลิลิตรต่อนาทีและใช้ออกซิเจนเพื่อช่วยในการกระจายตัวของสารตั้งต้นที่อัตราการป้อน 8, 5 และ 3 ลิตรต่อ

นาทีตามลำดับ เพื่อให้ได้ตัวเร่งปฏิกิริยาซิงค์ออกไซด์ที่มีขนาดผลึกต่างกัน

คือ 8.8, 19.4, 30, 40.9 และ 47 นาโนเมตร โดยให้ความดันลดที่ปลายหลอดคาปิลลารีรักษาไว้ที่ 1.5 บาร์ ส่วนละอองของสารตั้งต้นจะถูกจุดติดไฟโดยเปลวไฟที่ได้จากการป้อนมีเทน 1.5 ลิตรต่อนาทีและออกซิเจน 3 ลิตรต่อนาที โดยผงตัวเร่งปฏิกิริยาจะถูกกรองผ่านกระดาษกรองใยแก้ว และก๊าซเสียจะถูกดึงออกโดยใช้ปั๊มสุญญากาศ

2.3 ปฏิกิริยาการย่อยสลายเมธิลีนบลูโดยใช้แสงด้วยตัวเร่งปฏิกิริยา

ทุกสภาวะการทดลองเริ่มจากใส่เมธิลีนบลูที่มีความเข้มข้น 10 พีพีเอ็ม ปริมาณ 200 มิลลิลิตรบีกเกอร์ขนาด 250 มิลลิลิตร จากนั้นใส่ตัวเร่งปฏิกิริยา 20 มิลลิกรัม ทิ้งไว้ให้ตัวเร่งปฏิกิริยาดูดซับเมธิลีนบลูในความมืดนานเป็นเวลา 30 นาที จากนั้นเปิดหลอดยูวี (ฟิลิปส์) 15 วัตต์ 2 หลอด โดยเก็บตัวอย่างเมธิลีนบลูปริมาณ 3.5 มิลลิลิตร ทุกๆ 10 นาที เป็นเวลา 1 ชั่วโมง โดยก่อนที่จะนำตัวอย่างเมธิลีนบลูไปวัดค่าการดูดกลืนแสงด้วยเครื่องยูวี-วิสิเบิล สเปกโตรโฟโตมิเตอร์ที่ความยาวคลื่น 665 นาโนเมตรจะนำตัวอย่างเมธิลีนบลูไปแยกตัวเร่งปฏิกิริยาโดยใช้เครื่องเหวี่ยงสารตกตะกอน

2.4 การตรวจสอบคุณลักษณะของตัวเร่งปฏิกิริยา

การดูดซับทางกายภาพด้วยไนโตรเจน(BET) เพื่อวิเคราะห์ขนาดพื้นผิว ขนาดของรูและปริมาตรรูพรุน การกระเจิงรังสีเอ็กซ์ (XRD) เพื่อศึกษาโครงสร้างและขนาดของผลึก การดูดซับด้วยแก๊สคาร์บอนมอนออกไซด์เพื่อศึกษาการกระจายตัวของโลหะ กล้องจุลทรรศน์อิเล็กตรอนแบบส่องผ่าน(TEM) เพื่อวิเคราะห์หาขนาดของอนุภาคและแจกแจงรายละเอียดของอนุภาคและอิเล็คตรอนสปินเรโซแนนซ์ (ESR)

3. ผลการทดลองและวิจารณ์ผล

งานวิจัยนี้แสดงให้เห็นถึงคุณลักษณะและสมบัติในการเร่งปฏิกิริยาของตัวเร่งปฏิกิริยาซิงค์ออกไซด์ขนาดนาโนเมตรที่เตรียมด้วยวิธีเฟลมสเปรย์ไพโรไลซิสให้ได้ขนาดของผลึกที่แตกต่างกันในปฏิกิริยาการย่อยสลายเมธิลีนบลูโดยใช้แสงด้วยตัวเร่งปฏิกิริยา โดยเปรียบเทียบกับตัวเร่งปฏิกิริยาที่ใช้ทางการค้าเช่น ไทเทเนียมไดออกไซด์(Degussa P25) และไทเทเนียมไดออกไซด์ (JRC)

---

* corresponding author; Joongjai.P@chula.ac.th

การกระเจิงรังสีเอ็กซ์ของตัวเร่งปฏิกิริยาซิงค์ออกไซด์ดังรูปที่ 1 พบว่าประกอบด้วยรูปแบบของซิงค์ไคต์ที่มีโครงสร้างโมเลกุล 6 เหลี่ยม และเมื่อเพิ่มความเข้มข้นของสารตั้งต้นและอัตราส่วนระหว่างอัตราการป้อนสารตั้งต้นกับออกซิเจนที่ใช้ในการกระจายตัวของสารตั้งต้นเพิ่มขึ้นพบว่าจะทำให้ขนาดผลึกมีขนาดใหญ่ขึ้น 8.8 , 19.4, 30, 40.7 และ 47 นาโนเมตรตามลำดับ
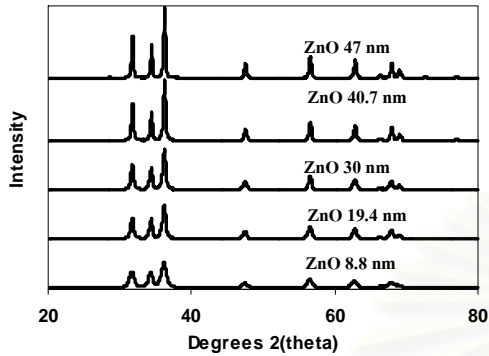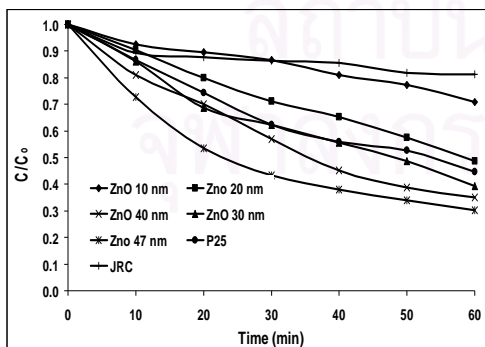

รูปที่ 1 รูปแบบ XRD ของตัวเร่งปฏิกิริยาซิงค์ ออกไซด์ขนาดผลึกต่างกัน ซึ่งเตรียมโดยวิธีแฟลมสเปรย์ไพโรไลซิส
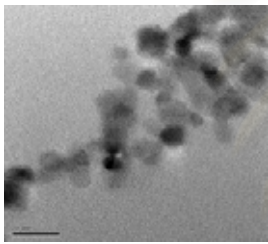
รูปที่ 2 รูป TEM ของตัวเร่งปฏิกิริยาตัวเร่งปฏิกิริยาซิงค์ออกไซด์ขนาดผลึก 8.8 นาโนเมตร

การศึกษาขนาดของอนุภาคด้วยกล้องจุลทรรศน์อิเล็กตรอนแบบส่องผ่านดังรูปที่ 2 พบว่าซิงค์ออกไซด์ประกอบด้วยอนุภาคหลายเหลี่ยมที่มีขนาดอนุภาคประมาณ 10-50 นาโนเมตร โดยมีแนวโน้มสอดคล้องกับค่าที่วัดได้จากเทคนิค XRD

รูปที่ 3 การย่อยสลายโดยใช้แสงของเมธิลีนบลูด้วยตัวเร่งปฏิกิริยาซิงค์ออกไซด์ที่มีขนาดผลึกต่างๆกัน

ผลการทดสอบตัวเร่งปฏิกิริยาซิงค์ออกไซด์ที่มีขนาดผลึกต่างกันเมื่อนำไปใช้ในปฏิกิริยาการย่อยสลายโดยใช้แสงของเมธิลีนบลูด้วยตัวเร่งปฏิกิริยาพบว่าเมื่อขนาดผลึกของซิงค์ออกไซด์มีขนาดใหญ่ขึ้นจะสามารถย่อยสลายเมธิลีนบลูได้เร็วขึ้นดังรูปที่ 3 ซึ่งเมื่อขนาดผลึกของซิงค์ออกไซด์มีขนาด 10 นาโนเมตรขึ้นไปจะให้ประสิทธิภาพในการย่อยสลายได้ดีกว่าตัวเร่งปฏิกิริยาไทเทเนียมไดออกไซด์ (JRC) ส่วนซิงค์ออกไซด์ขนาด 30 นาโนเมตรขึ้นไป จะให้ประสิทธิภาพในการย่อยสลายได้ดีกว่าตัวเร่งปฏิกิริยาไทเทเนียมไดออกไซด์ (P25)

4. สรุปผลการทดลอง

วิธีเฟลมสเปรย์ไพโรไลซิสสามารถเตรียมตัวเร่งปฏิกิริยาซิงค์ออกไซด์ให้มีขนาดของอนุภาคที่มีระดับนาโนเมตรได้และสามารถควบคุมขนาดของอนุภาคได้ดี โดยขนาดผลึกของตัวเร่งปฏิกิริยาซิงค์ออกไซด์จะมีขนาดใหญ่ขึ้นตามการเพิ่มขึ้นของความเข้มข้นของสารตั้งต้นและอัตราส่วนของอัตราการป้อนสารตั้งต้นกับออกซิเจนที่ใช้ในการกระจายตัวของสารตั้งต้น ซึ่งตัวเร่งปฏิกิริยาซิงค์ออกไซด์ที่มีขนาดผลึกใหญ่ขึ้น จะสามารถช่วยเพิ่มประสิทธิภาพในการย่อยสลายเมธิลีนบลูโดยใช้แสงของด้วยตัวเร่งปฏิกิริยาได้ เนื่องจากเมื่อขนาดผลึกของตัวเร่งปฏิกิริยา ซิงค์ออกไซด์ใหญ่ขึ้นจะมีปริมาณออกซิเจนที่อยู่ในโครงร่างผลึกมากขึ้นด้วย

5. กิตติกรรมประกาศ

6. เอกสารอ้างอิง

[1] Height, M.J., Pratsinis, S.E., Mekasuwandumrong, O. and Praserthdam, P. (2006), Ag-ZnO catalysts for UV-photodegradation of methylene blue, Applied Catalysis B: Environmental, 63, 305–312.

[2] Jang, Y.J., Simer, C. and Ohm, T. (2006), Comparison of zinc oxide nanoparticles and its nano-crystalline particles on the photocatalytic degradation of methylene blue, Materials Research Bulletin, 41, 67–77.

[3] Li, F.B. and Li, X.Z. (2002), Photocatalytic properties of gold/gold ion-modified titanium dioxide for wastewater treatment, Applied Catalysis A: General, 228, 15–27.

[4] Li, F.B. and Li, X.Z. (2002), The enhancement of photodegradation efficiency using Pt–TiO2 catalyst, Chemosphere, 48, 1103–1111.

[5] Tani, T., Kato, A. and Morisaka, H. (2005), Effect of solvent on powder characteristic of Zinc Oxide and Magnesia prepared by flame spray pyrolysis, Journal of the Ceramic Society of Japan, 113 (3), 255 –258.

VITA

Mr. Pongsapak Pawinrat was born on 4th May 1984, in Bangkok, Thailand. He received his Bachelor degree of science with a major in Chemical technology from Chulalongkorn University, Bangkok, Thailand in May 2006. He continued his Master study in the major in Chemical Engineering at Chulalongkorn University, Bangkok, Thailand in June 2006.